Excited State Pathways in 3rd Generation Organic Light-Emitting Diodes

Dissertation zur Erlangung des
naturwissenschaftlichen Doktorgrades
der Julius-Maximilians-Universität Würzburg

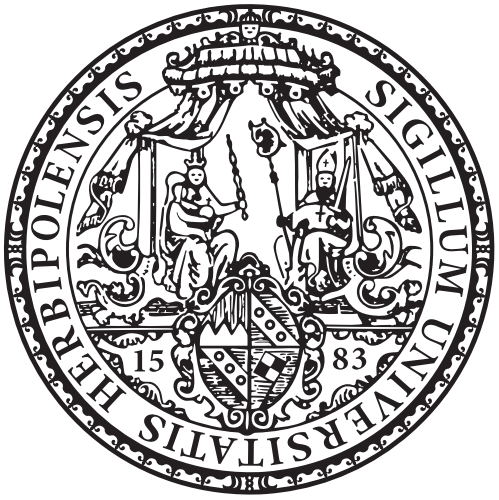

vorgelegt von

Nikolai Eberhard Bunzmann

aus Hof

Würzburg, 2020

Eingereicht am: 30.06.2020
bei der Fakultät für Physik und Astronomie

1. Gutachter: Prof. Dr. Vladimir Dyakonov
2. Gutachter: Prof. Dr. Sven Höfling
3. Gutachter:
der Dissertation.

Vorsitzende(r):

1. Prüfer: Prof. Dr. Vladimir Dyakonov
2. Prüfer: Prof. Dr. Sven Höfling
3. Prüfer: Prof. Dr. Johanna Erdmenger
im Promotionskolloquium.

Tag des Promotionskolloquiums: 18.12.2020

Doktorurkunde ausgehändigt am:

Contents

1 Introduction 1

2 Organic Light-Emitting Diodes 5
- 2.1 Organic Semiconductors . . . 5
- 2.2 Excitons in Organic Semiconductors . . . 7
- 2.3 Transitions between Excitonic States . . . 10
- 2.4 Jablonski Diagram . . . 11
- 2.5 Working Principle of OLEDs . . . 16
- 2.6 Quantifying OLED Efficiencies . . . 19
- 2.7 The Different Generations of OLEDs . . . 20
- 2.8 Transition Rates of TADF Emitters . . . 22
- 2.9 Molecular Design of TADF Emitters . . . 23
- 2.10 Time-Resolved Luminescence of TADF Emitters . . . 25
- 2.11 Photometric Quantities and Color Coordinates . . . 27

3 Electron Paramagnetic Resonance 33
- 3.1 Electron Zeeman Interaction . . . 33
- 3.2 Zero-Field Interaction . . . 34
- 3.3 EPR Transitions between Triplet States . . . 36
- 3.4 Half-Field Transition . . . 40
- 3.5 Spin Polarization . . . 41
- 3.6 Detection Schemes . . . 42

4 Experimental Section 47
- 4.1 PLDMR . . . 47
- 4.2 ELDMR . . . 50
- 4.3 EDMR . . . 54
- 4.4 External Quantum Efficiency . . . 56
- 4.5 Continuous Wave and Time-Resolved Photoluminescence . . . 59
- 4.6 Photometric Quantities and Color Coordinates . . . 59

5 Optically and Electrically Excited Intermediate States in D:A based OLEDs 61
5.1 Introduction . . . 62
5.2 Materials and Devices . . . 64
5.3 Time-Resolved Photoluminescence . . . 66
5.4 Electroluminescence Detected Magnetic Resonance . . . 68
5.5 Photoluminescence Detected Magnetic Resonance . . . 74
5.6 Discussion . . . 75
5.7 Summary . . . 79
5.8 Conclusion . . . 81
5.9 Additional Experimental Details . . . 82
5.10 Contributions to this Chapter . . . 83

6 Taking OLEDs for a Spin — is Light Generation in TADF OLEDs Spin-Dependent? 85
6.1 Introduction . . . 86
6.2 Materials and Devices . . . 87
6.3 pEDMR Experiments - Theory . . . 89
6.4 pEDMR Experiments - Results . . . 91
6.5 Discussion . . . 94
6.6 Conclusion . . . 97
6.7 Contributions to this Chapter . . . 98

7 Spin- and Voltage-Dependent Emission from Intra- and Intermolecular TADF OLEDs 99
7.1 Introduction . . . 100
7.2 Materials and Devices . . . 101
7.3 Electroluminescence Detected Magnetic Resonance . . . 104
7.4 Photoluminescence Detected Magnetic Resonance . . . 108
7.5 Summary . . . 112
7.6 Conclusion . . . 114
7.7 Additional Experimental Details . . . 115
7.8 Contributions to this Chapter . . . 116

8 Summary 117

Bibliography 122

1 Introduction

"Any fool can know. The point is to understand."

Albert Einstein [1]

The year 2020 will go down in history as the year of the COVID-19 pandemic. Life stands still because a virus is spreading over the entire world. Countries are taking all sorts of measures to contain the virus. Shops, hotels and restaurants are closed. Schools and kindergardens are shut down. Employees of firms and facilities can't go to work. The world's economy is suffering. People fear for their jobs. One of the results: conspiracy theories are booming. While governments try to stop spreading of the virus, it is practically impossible to stop spreading of false information in the day and age of social media. Everyone believes their opinion is the one and only truth. Whoever screams the loudest is heard the most. Here is where Einstein's quote comes into play. People take information as it is without analyzing or questioning it. They just *know* something but they don't *understand* it. More than ever, science has a responsibility to present facts based on independent, unbiased and thorough research. Speculation and presumptions are not enough. It is important to *understand* rather than just to *know*. Only then are we going to be able to make reasonable decisions to cope with challenges such as the corona crisis.

The importance of *understanding* doesn't apply to only the corona virus but to all fields of research. Superficial *knowledge* is not enough to develop progressive technologies. Especially in a time in which industry has a responsibility for sustainability, it is essential to develop a detailed *understanding* of the physics underlying technological applications. This thesis is about organic light-emitting diodes (OLEDs) that are based on thermally activated delayed fluorescence (TADF). The goal of this work is to develop a better *understanding* of these devices. Before we get into that, let's first have a look at what makes OLEDs worth being studied.

OLEDs have drawn the attention of research and industry as they bring a lot of advantages over competing technologies such as liquid-crystal displays (LCDs). OLED displays offer wide viewing angles, a high contrast ratio and a fast response time [2]. They do not require any backlighting enabling high efficiencies. Furthermore, OLEDs consist of thin layers and can be prepared on flexible substrates which opens up in-

novative applications such as foldable displays [3]. The chemical variability of organic molecules allows for fine tuning of emission colors and therefore specific molecular design that is tailored to the desired application.

Before we turn to the current challenges of today's OLED research, let's have a little history lesson on the emergence of this technology. A major breakthrough towards the realization of OLEDs as light sources came in 1987 when Tang and Van Slyke were able to build a device based on the compound tris(8-hydroxyquinoline)aluminum (Alq_3), which achieved an external quantum efficiency of around 1% at reasonable voltages below 10 V [4]. Light generation in the early demonstrations of electroluminescence from organic systems is based on fluorescence which is the radiative decay of singlet states. Those devices are also referred to as 1st generation OLEDs.

In electrically driven devices only 25% of injected charge carriers form radiative singlet states, while 75% form non-radiative triplet states. This fundamental limitation can be overcome by direct harvesting of triplet states, namely via phosphorescence which is the radiative transition of triplet excited states to the singlet ground state. Efficient phosphorescence can be achieved in emitter molecules that contain heavy metals such as Iridium or Platinum, which considerably enhance the radiative transition rate of triplets. The respective devices are also called 2nd generation OLEDs. The high potential of this generation was first shown by Baldo et al. in 1998 [5] where an external quantum efficiency of 4% was demonstrated. By 2001, 2nd generation OLEDs achieved internal quantum efficiencies of around 100% [6]. This significant increase in efficiency paved the way for OLEDs to be commercialized.

To this day, most OLED displays use 2nd generation emitters for the implementation of red and green pixels [7]. Blue pixels on the other hand still rely on fluorescence emitters as many phosphorescence-based blue emitters suffer from low stability and insufficient color purity [8]. Therefore, two drawbacks remain with the use of 1st and 2nd generation OLEDs: On the one hand, phosphorescence-based emitters rely on heavy atoms which is associated with high production costs and resource consumption. On the other hand, blue emitters still suffer from low efficiency as only fluorescence-based emitters meet the requirements needed for applications in displays.

Both of these issues can potentially be solved by OLEDs based on thermally activated delayed fluorescence (TADF). These types of devices are also called 3rd generation OLEDs. Here, triplet states are harvested via thermal upconversion to singlet states through reverse intersystem crossing (RISC) followed by radiative decay. This effect had already been observed in 1961 [9] but it took until 2012 that Adachi and coworkers demonstrated its high potential for efficient OLEDs [10, 11]. They showed that proper molecular design enables minimization of the energy gap between singlet and triplet

states which considerably enhances the reverse intersystem crossing rate. The efficient harvesting of triplet states allows for a theoretical internal quantum efficiency of 100% without the use of heavy metal atoms. After the basic demonstration of potentially high efficiencies, research devoted itself to various aspects that are important for the further development of TADF emitters towards practical applications. Next steps involved pushing the limit of internal quantum efficiencies towards 100% for several molecules of different emission color [12, 13, 14, 15, 16, 17].

Let's remember Einstein's quote at this point. *Knowing* that TADF OLEDs can be efficient is a first step. But *understanding* why is essential. A detailed *understanding* of generally spin-forbidden RISC is necessary for a purposeful design and synthesis of new emitters. Plenty of photophysical investigations [18, 19], but also theoretical calculations [20, 21] were conducted in order to rationalize the observation of high efficiencies in TADF OLEDs. Different mechanisms such as spin–orbit coupling [22, 23, 24] and hyperfine interaction [25] were proposed to be responsible for efficient triplet to singlet conversion. Moreover, some reports postulated the necessity of an involvement of local triplet states for efficient RISC [24, 26].

To address those issues, a spin-sensitive measurement technique is desirable. This is provided by electron paramagnetic resonance (EPR). EPR is a widely used tool in the field of spin-spectroscopy [27]. It is based on absorption of microwave photons by spin states that are split in an external magnetic field. Advanced EPR methods, such as electroluminescence or photoluminescence detected magnetic resonance (ELDMR, PLDMR), are particularly suitable to investigate TADF emitters, as they create a direct link between triplet states and light generation.

In this work, advanced EPR techniques and photophysical characterization methods are applied to a series of different TADF systems. The sum of the corresponding results in their entirety allows for a deeper understanding of light generation in TADF emitters.

"*...The point is to understand*".

Structure of this Thesis

Chapters 2-4 of this thesis provide the theoretical background regarding TADF OLEDs and EPR spectroscopy that is needed to understand the experiments conducted in this work:

Chapter 2 introduces the fundamentals of photophysical processes in organic semiconductors and explains the working principle of OLEDs. The phenomenon of TADF is explained, including the corresponding molecular properties and emission characteristics.

Chapter 3 provides the basics of EPR with a focus on triplet spectroscopy. Furthermore, the advanced EPR methods ELDMR, PLDMR and EDMR are introduced and their particular suitability for the investigation of TADF systems is explained.
Chapter 4 describes how ELDMR, PLDMR and EDMR are technically realized.

The experiments of this work can be divided into the following three parts:

Chapter 5 presents the application of (time-resolved) photophysical characterization methods and advanced EPR techniques on several donor:acceptor based TADF emitters.
Chapter 6 shows pulsed EDMR experiments on a prominent donor:acceptor TADF system.
Chapter 7 presents advanced EPR experiments on a TADF emitter that intrinsically exhibits intramolecular TADF but can also be used as a constituent of a donor:acceptor TADF system.

Chapter 8 provides a summary of this thesis.

2 Organic Light-Emitting Diodes

This chapter provides fundamental knowledge about organic light-emitting diodes (OLEDs) and thermally activated delayed fluorescence (TADF). At the beginning, the material class of organic semiconductors is introduced, with a focus on the properties that are most relevant for OLEDs. In particular, excitons in organic semiconductors and transitions between quantum mechanical states of excitons are discussed. The concepts of this part and their presentation are mostly based on the textbook "Electronic Processes in Organic Semiconductors" by Anna Köhler and Heinz Bässler [28]. Some ideas are taken from the textbook "Experimentalphysik 3" by Wolfgang Demtröder [29].

Later in this chapter, the basic working principle of OLEDs and the fundamental device physics underlying electroluminescence are explained. The main reference here is the review "Device efficiency of organic light-emitting diodes: Progress by improved light outcoupling" by Wolfgang Brütting [30].

The final part, which is based on recent publications, introduces TADF OLEDs and their basic properties. Overall, the purpose of this chapter is to provide the knowledge about TADF OLEDs, that is needed to understand electron paramagnetic resonance (EPR) experiments on such devices.

2.1 Organic Semiconductors

The class of organic molecules includes all chemical compounds that mainly consist of covalently bound carbon atoms. Organic semiconductors are a subgroup of organic materials and are the basis of the LEDs investigated in this thesis. In order to explain the semiconducting properties of these materials and their potential for technological applications, it is essential to first introduce the electronic properties of carbon atoms and their bonds.

An isolated carbon atom has 6 electrons occupying the 1s, the 2s and two of the 2p orbitals. The resulting electronic configuration is given as $(1s)^2(2s)^2(2p_x)^1(2p_y)^1$. In this configuration, two covalent bonds can hypothetically be formed. However, it is energetically more favorable if so-called *hybrid orbitals* are formed from a linear combination of the 2s and the 2p orbitals enabling the formation of four instead of two

bonds. Linear combinations of the 2s and one 2p, two 2p or three 2p orbitals lead to the formation of the so-called sp, sp^2 or sp^3 orbitals.

In order to understand semiconducting properties in organic molecules it is important to have a closer look at the sp^2 hybridization. In this case, the 2s, the $2p_x$, and the $2p_y$ orbitals form three sp^2 hybrid orbitals, all of which can form so-called σ-bonds. The remaining $2p_z$ orbital is not involved in the hybridization and can form a so-called π-bond. One of the most simple examples to explain sp^2 hybridization is given by the ethene molecule, which consists of two carbon and four hydrogen atoms. The molecular structure of ethene and the spatial arrangement of the involved orbitals are shown in **Figure 2.1a**.

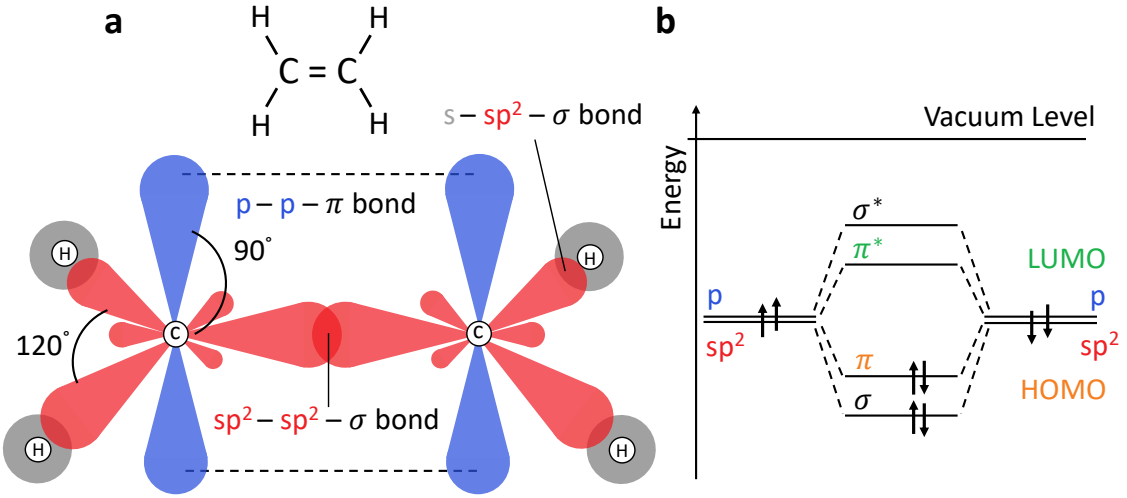

Figure 2.1: Hybridization of orbitals in ethene. **a**, **Top**: molecular structure of ethene. **Bottom**: spatial arrangement of orbitals in ethene. For each of the two carbon atoms, the three sp^2 orbitals (red) are in one plane with an angle of 120° between them. The p_z orbitals (blue) are perpendicular to that plane. s–sp^2-σ-bonds are formed between carbon and hydrogen (grey). An sp^2–sp^2-σ-bond and a p–p-π-bond are formed between the two carbon atoms. **b**, Energy levels for two carbon atoms with (middle) and without (left/right) a double bond. A double bond leads to the formation of a bonding σ/π and an anti-bonding σ^*/π^* state. The energetically most favorable configuration corresponds to a spin-up and a spin-down electron in the σ state and the π state, respectively. Hydrogen–carbon bonds are omitted. Adapted from [28].

The three sp^2 orbitals are in one plane, with an angle of 120° between them. The $2p_z$ orbitals are oriented perpendicular to this plane. Two of the sp^2 orbitals form a s–sp^2-σ-bond with the 1s orbital of a hydrogen atom, while one sp^2 orbital forms a sp^2–sp^2-σ-bond with the other carbon's sp^2 orbital. The two $2p_z$ orbitals have a small overlap leading to a p–p-π-bond. The bonding of two carbon atoms via a σ- and a π-bond is referred to as a *double bond*.

The formation of hybridized orbitals and bonds between atoms changes the energetic position of the involved states. The energy levels of orbitals involved in carbon–carbon bonds are shown in **Figure 2.1b**. In a single isolated carbon atom, the energy level of the carbon's p_z orbital is energetically slightly higher than the sp^2 hybrid orbitals. Each p and sp^2 orbital is occupied with one electron. In case of a double bond between the two carbon atoms, new shared bonding σ and π as well as anti-bonding σ^* and π^* states are created. The molecular bonding states are lower in energy than the atomic orbitals, which reduces the total energy of the system compared to single atoms. Now, both the σ- and the π-orbital is occupied by a spin-up and a spin-down electron, respectively. In this configuration, the highest occupied molecular orbital (HOMO) is given by the π-orbital and the lowest unoccupied molecular orbital (LUMO) is given by the π^*-orbital. The energy gap between the HOMO and LUMO is comparable to the band gap in conventional inorganic semiconductors. It is one of the most relevant parameters for organic semiconductors, as it determines optical properties, such as absorption and emission characteristics.

Ethene is a simple example that demonstrates the physics of double bonds in organic molecules. However, the compounds used in organic electronics typically involve several carbon atoms with alternating single and double bonds, which results in orbitals delocalized over several atoms within the molecule. Synthesis of molecules with different numbers of carbon atoms, as well as the inclusion of heteroatoms, such as sulfur, nitrogen or oxygen, allows tuning of the molecule's optoelectronic properties.

2.2 Excitons in Organic Semiconductors

When organic molecules are in their ground state, all orbitals up to the HOMO are filled with a spin-up and a spin-down electron. Under optical excitation with sufficient energy, one of the electrons can be excited to the LUMO. The unoccupied state that is left behind in the HOMO is referred to as a *hole*. Excitons are formed between the excited electron and the hole. In the context of organic molecules, those electron–hole pairs are referred to as *Frenkel excitons*. In contrast to their inorganic counterparts, they are strongly bound, which is due to the relatively small dielectric constant of organic compounds. As a consequence, they are typically localized on one molecule. The excitation of excitons and their radiative decay are the basis of light generation in OLEDs. Therefore, understanding the photo-physics of excitons is essential for proper description of the working principle of OLEDs.

Spin states

The electron spin is of particular importance for excitonic states. The spin describes an electron's intrinsic angular momentum. A spin system's total angular momentum is characterized by the spin quantum number s and the z-component by the magnetic quantum number m_s. For electrons, $s = 1/2$ and $m_s = \pm 1/2$. The corresponding eigenstates are denoted as follows: $|\Psi(m_s = 1/2)\rangle = |\alpha\rangle$ ('spin-up') and $|\Psi(m_s = -1/2)\rangle = |\beta\rangle$ ('spin-down'). Electron–hole pairs are described as a single quasi-particle with effective values for s and m_s. In this case, the two spins of the electrons with their individual spin states $|\Psi_1\rangle$ and $|\Psi_2\rangle$ forming the exciton need to be combined: $|\Psi_{\text{Exc}}\rangle = |\Psi_1\Psi_2\rangle$. Mathematically, this means that both of the two-dimensional Hilbert spaces describing the eigenstates of the two single electrons are combined to a four-dimensional Hilbert space describing the eigenstates of the exciton. The four eigenstates of the combined Hilbert space can be represented in different bases. In the context of OLEDs, it is most convenient to use the so-called singlet–triplet base:

$$\begin{aligned} &\text{Singlet} \quad |\Psi_{\text{S}}\rangle = \tfrac{1}{\sqrt{2}}\left(|\alpha_1\beta_2\rangle - |\beta_1\alpha_2\rangle\right) && s = 0, m_s = 0 \\ &\text{Triplet} \begin{cases} |\Psi_{\text{T}_+}\rangle = |\alpha_1\alpha_2\rangle & s = 1, m_s = +1 \\ |\Psi_{\text{T}_0}\rangle = \tfrac{1}{\sqrt{2}}\left(|\alpha_1\beta_2\rangle + |\beta_1\alpha_2\rangle\right) & s = 1, m_s = 0 \\ |\Psi_{\text{T}_-}\rangle = |\beta_1\beta_2\rangle & s = 1, m_s = -1 \end{cases} \end{aligned} \tag{2.1}$$

The excitonic spin states can be categorized into singlet and triplet states, depending on the total spin quantum number s. There is one excitonic spin state $|\Psi_{\text{S}}\rangle$, with $s = 0$, referred to as *singlet* state and three excitonic spin states $|\Psi_{\text{T}_+}\rangle$, $|\Psi_{\text{T}_0}\rangle$ and $|\Psi_{\text{T}_-}\rangle$, with $s = 1$, referred to as *triplet* states. Those spin states can be in different electronic excited states. The lowest excited singlet state is denoted as S_0 and represents the ground state of most organic semiconductors. Higher excited singlet states are denoted as $S_1, S_2, ..., S_i$. Likewise, triplet states are denoted as $T_1, T_2, ..., T_i$. Sometimes the term *singlet/ triplet* is used as a short form for *singlet state/ triplet state*.

An exciton's spin state has important consequences for the total energy of the exciton. One can show that the energy difference between singlet and triplet exciton ΔE_{ST} is given by [31]:

$$\Delta E_{\text{ST}} = E_{\text{Singlet}} - E_{\text{Triplet}} = 2J \tag{2.2}$$

with

$$J = \iint \phi_{\text{HOMO}}(\mathbf{r}_1)\,\phi_{\text{LUMO}}(\mathbf{r}_2)\,\frac{e^2}{|\mathbf{r}_2 - \mathbf{r}_1|}\,\phi_{\text{HOMO}}(\mathbf{r}_2)\,\phi_{\text{LUMO}}(\mathbf{r}_1)\,\mathrm{d}\mathbf{r}_1\mathrm{d}\mathbf{r}_2 \tag{2.3}$$

Here, ϕ_{HOMO} and ϕ_{LUMO} are the spatial wave functions of the HOMO and the LUMO, respectively, and $\mathbf{r}_1$ and $\mathbf{r}_2$ are position vectors of the two electrons forming the exciton. J is referred to as exchange integral and is determined by the spatial overlap of HOMO and LUMO. This connection is essential for the design of TADF emitters, which exploit the spatial separation of HOMO and LUMO in order to minimize ΔE_{ST}. A more in-depth explanation of the molecular design of TADF emitters will be given in a later chapter in this thesis. Also note that the above discussion neglects any spin–spin interactions. Therefore, **Equation 2.2** implies degenerate energies for all three triplet states, which is not generally valid. The impact of spin-spin interactions will be discussed within the context of EPR later on.

ΔE_{ST} and Wave Function Symmetries

J is always positive, meaning that the singlet state is always higher in energy than the triplet state. This can be understood intuitively from the symmetries of the electronic wave functions of singlet and triplet state. The total wave function of an exciton is given by the product of electronic wave function and spin wave function: $\Psi_{\mathrm{tot}} = \Psi_{\mathrm{el}}\Psi_{\mathrm{spin}}$ (The vibrational wave function is omitted at this point because it is negligible for the following discussion). According to Pauli's principle, the total wave function of a multi-fermion system needs to be antisymmetric with respect to the interchange of two fermions (in the case of excitons in organic molecules, two electrons) [32]. The spin wave function of a singlet is antisymmetric and the spin wave function of a triplet is symmetric (see **Equation 2.1**). In order for Pauli's principle to be fulfilled, the electronic wave function of a singlet exciton must be symmetric $\Psi_{\mathrm{el}}^{\mathrm{Sing}}(\mathbf{r}_1,\mathbf{r}_2) = \Psi_{\mathrm{el}}^{\mathrm{Sing}}(\mathbf{r}_2,\mathbf{r}_1)$ and the electronic wave function of a triplet exciton antisymmetric $\Psi_{\mathrm{el}}^{\mathrm{Trip}}(\mathbf{r}_1,\mathbf{r}_2) = -\Psi_{\mathrm{el}}^{\mathrm{Trip}}(\mathbf{r}_2,\mathbf{r}_1)$. For an antisymmetric wave function of a two-particle system, the probability for both particles to be found at the same spatial coordinate ($\mathbf{r}_1 = \mathbf{r}_2 = \mathbf{r}_0$) vanishes:

$$\Psi_{\mathrm{el}}^{\mathrm{Trip}}(\mathbf{r}_0,\mathbf{r}_0) = -\Psi_{\mathrm{el}}^{\mathrm{Trip}}(\mathbf{r}_0,\mathbf{r}_0) \Rightarrow \Psi_{\mathrm{el}}^{\mathrm{Trip}}(\mathbf{r}_0,\mathbf{r}_0) = 0 \tag{2.4}$$

For a symmetric wave function, on the other hand, this probability is non-zero. This can be interpreted such that two electrons forming a singlet are on average closer to each other than two electrons forming a triplet. Consequently, the electron–electron repulsion for a singlet is higher than for a triplet. This eventually causes the singlet state to be higher in energy than the triplet state.

2.3 Transitions between Excitonic States

Transitions between two quantum mechanical states are generally described by Fermi's golden rule. It states that the transition rate k_{if} between an initial state Ψ_{i} and a final state Ψ_{f} is given by:

$$k_{\mathrm{if}} = \frac{2\pi}{\hbar} |\langle \Psi_{\mathrm{f}} | \hat{H}' | \Psi_{\mathrm{i}} \rangle|^2 \rho \tag{2.5}$$

Here, $\hbar$ is the reduced Planck constant and ρ the density of final states. Furthermore, the system is assumed to be slightly perturbed, which is considered via the perturbing Hamiltonian $\hat{H}'$. Optical transitions between excitonic states in organic molecules are described by the dipole operator $\hat{H}' = e\hat{\mathbf{r}}$. In this case, three components of the exciton's total wave function are relevant: the electronic, the spin and the vibrational wave function: $\Psi_{\mathrm{tot}} = \Psi_{\mathrm{el}}\Psi_{\mathrm{spin}}\Psi_{\mathrm{vib}}$. The vibrational wave function considers vibrational modes of the molecule's nuclei. Similarly to electronic states, vibrational modes exist in different levels of excitation $\Psi_{\mathrm{vib}} = \nu_0, \nu_1, \nu_2, ..., \nu_i$. Fermi's golden rule applied to a molecule's initial and final total wave function yields:

$$k_{\mathrm{if}} = \frac{2\pi}{\hbar} |\langle \Psi_{\mathrm{el,f}}\Psi_{\mathrm{spin,f}}\Psi_{\mathrm{vib,f}} | e\hat{\mathbf{r}} | \Psi_{\mathrm{el,i}}\Psi_{\mathrm{spin,i}}\Psi_{\mathrm{vib,i}} \rangle|^2 \rho \tag{2.6}$$

The dipole operator acts only on the electronic wave function, such that **Equation 2.6** can be rewritten as:

$$k_{\mathrm{if}} = \frac{2\pi}{\hbar} |\langle \Psi_{\mathrm{el,f}} | e\hat{\mathbf{r}} | \Psi_{\mathrm{el,i}} \rangle|^2 |\langle \Psi_{\mathrm{spin,f}} | \Psi_{\mathrm{spin,i}} \rangle|^2 |\langle \Psi_{\mathrm{vib,f}} | \Psi_{\mathrm{vib,i}} \rangle|^2 \rho \tag{2.7}$$

Accordingly, the transition rate between two excitonic states is determined by three different factors, all of which have to be non-zero for the transition to be allowed. The role of those three respective factors in the context of optoelectronic applications of organic semiconductors will be explained in the following.

Electronic Factor

The electronic factor is often referred to as the *transition dipole moment* $\mu_{\mathrm{i\text{-}f}}$:

$$\mu_{\mathrm{i\text{-}f}}^2 = |\langle \Psi_{\mathrm{el,f}} | e\hat{\mathbf{r}} | \Psi_{\mathrm{el,i}} \rangle|^2 \tag{2.8}$$

$\mu_{\mathrm{i\text{-}f}}$ scales with the overlap of initial and final state. In case of an exciton on an organic molecule, this corresponds to the overlap between HOMO and LUMO. The transition rates of radiative decay channels are proportional to $\mu_{\mathrm{i\text{-}f}}^2$. A sufficiently high overlap between HOMO and LUMO is therefore needed for a radiative transition to be efficient.

Spin Factor

The spin factor $|\langle\Psi_{\text{spin,f}}|\Psi_{\text{spin,i}}\rangle|^2$ can be either 0 for transitions between states of different spin number s, or 1 for states with equal spin number. This strict spin-selection rule does not apply if spin-mixing perturbations exist within the system. A common effect in organic semiconductors that enables spin-mixing is spin–orbit coupling. It describes the interplay between spin and angular orbital momentum. Spin flips can be induced by spin–orbit coupling because a change in spin is compensated by a change of orbital angular momentum. Another spin-mixing effect in organic molecules is hyperfine interaction. It describes the coupling between electron spins and nuclear spins. Here, spin flips are enabled as the change of electron spin is compensated by a change of nuclear spin.

Vibrational Factor

The third factor in **Equation 2.7** takes vibrational modes into account. For each transition between two electronic states, there is a series of transitions between different vibrational levels. The intensity of those individual transitions is determined by the vibrational factor $|\langle\Psi_{\text{vib,f}}|\Psi_{\text{vib,i}}\rangle|^2$, referred to as *Franck–Condon-factor*. It governs the shape of the emission and absorption spectra of organic molecules. Single transitions between particular vibrational levels are however typically not resolved in emission spectra of TADF emitters at room temperature.

2.4 Jablonski Diagram

A summary of all possible transitions between excitonic states in an organic semiconductor are shown in **Figure 2.2**, which depicts a so-called *Jablonski diagram*. The most relevant processes and the corresponding terminology are presented in the following.

Absorption

The ground state of organic semiconductors is commonly the singlet ground state S_0. The molecule is most likely to be found in the lowest vibrational excitation ν_0 at room temperature, according to Boltzmann statistics. Therefore, absorption always takes place from the lowest vibrational level of the singlet ground state to any vibrational level ν_i of a higher excited singlet state S_k. The intensity of any of those transitions is determined by the Franck–Condon-factor and the transition dipole moment. Absorption from the singlet ground state to a triplet state is forbidden, as optical transitions are only possible between spin states of equal spin number.

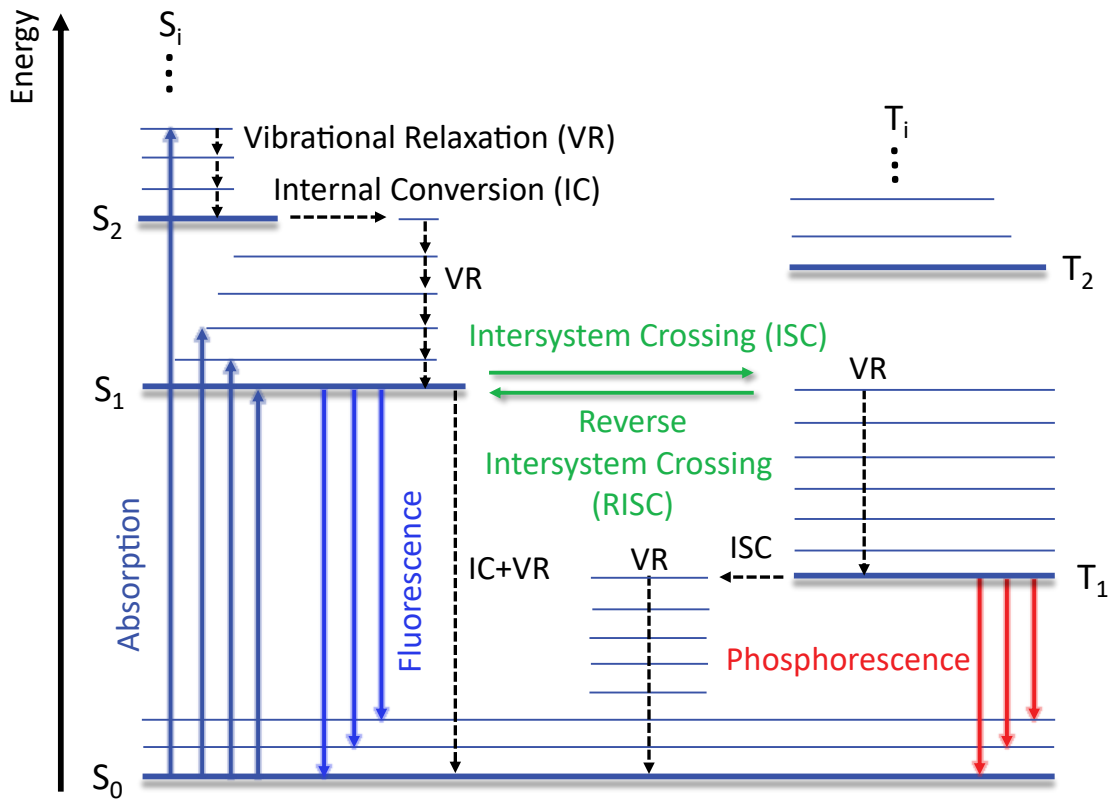

Figure 2.2: Jablonski diagram showing fundamental transitions between excitonic states in an organic semiconductor. The ground state for most organic semiconductors is the singlet ground state S_0. Higher excited singlet states are denoted as S_1, S_2,...,S_i; excited triplet states as T_1, T_2,...,T_i. Vibrational levels are indicated as thin lines.

Vibrational Relaxation and Internal Conversion

After absorption into a vibrational level v_i of an excited singlet state S_k, the molecule continuously relaxes from one vibrational level v_i to the next lower-lying one v_{i-1} till the zeroth vibrational level v_0 of the S_k state is reached. This process is called *vibrational relaxation* (VR). After VR, a transition from the zeroth vibrational level of S_k to a higher excited vibrational level of S_{k-1} takes place. This process is called *internal conversion* (IC) and is indicated as horizontal arrow in Jablonski diagrams. Subsequent VR and IC take place until the zeroth vibrational level of the S_1 state is reached.

Fluorescence

The radiative decay of a singlet state is called *fluorescence*. Because of the fast processes of VR and IC, fluorescence always occurs from the zeroth vibrational level of the S_1 state. This principle is called *Kasha's rule*. Radiative transitions from S_1 are generally possible into any vibrational level of the singlet ground state S_0. The intensity of the

individual transition into a specific vibrational level is determined by the respective Franck–Condon-factor. The overall fluorescence intensity is mostly determined by the transition dipole moment $\mu_{S_1-S_0}$ related to the overlap between the electronic wave functions of S_1 and S_0.

Intersystem Crossing

One possible depopulation mechanism of the S_1 state is *intersystem crossing* (ISC). It describes transitions from a vibrational level of the S_1 state to an isoenergetic higher excited vibrational level of the T_1 state. This transition is a horizontal line in a Jablonski diagram. According to the discussion of the spin factor in **Equation 2.7**, such a transition is forbidden. A perturbation, such as spin–orbit coupling or hyperfine interaction, is therefore necessary to enable ISC. The ISC rate scales with the strength of the respective perturbation.

Phosphorescence

After ISC, the molecule is in a higher vibrational level of the T_1 state. Subsequently, VR takes place and the molecule relaxes to the zeroth vibrational level of the T_1 state. The radiative transition from T_1 to any of the vibrational levels of T_0 is called *phosphorescence*. As for ISC, a spin-mixing perturbation is needed to enable phosphorescence. Additionally, the transition dipole moment $\mu_{T_1-S_0}$ between T_1 and S_1 needs to be sufficiently large. If no significant spin-mixing perturbation is present, the radiative transition from T_1 to S_0 is typically outcompeted by other depopulation channels resulting in no observation of phosphorescence.

Reverse Intersystem Crossing

The reverse process of ISC is referred to as *reverse intersystem crossing* (RISC). In a Jablonski diagram it is a horizontal transition from T_1 to S_1. Since RISC is the fundamental process underlying TADF-based OLEDs, it will be described in more detail in the following. In order to understand the nature of RISC, it is helpful to derive an expression for the rate of population transfer k_{RISC} due to RISC. In other words, the number of excitons that are converted per time from a triplet spin configuration to a singlet spin configuration. The derivation of this rate is based on **Figure 2.3**, which depicts a section of a full Jablonski diagram that is reduced to only the S_1 and the T_1 state.

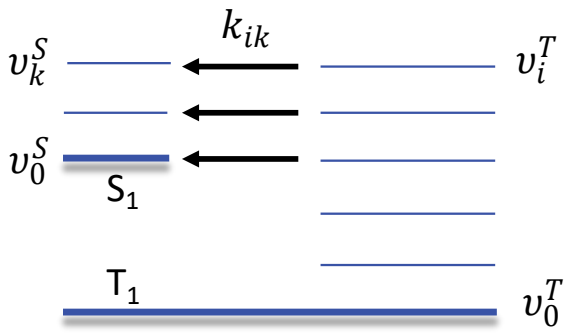

Figure 2.3: Explanation of RISC in a Jablonski diagram consisting of a T_1 and an S_1 state. Both have excited vibrational levels v_i^T and v_k^S with the lowest vibrational levels being v_0^T and v_0^S. RISC with a rate k_{ik} takes place between isoenergetic pairs of v_i^T and v_k^S.

Both the T_1 and the S_1 state have vibrational states v_i^T and v_k^S in different levels of excitation i and k. RISC can take place between any pairs of v_i^T and v_k^S that are isoenergetic. The transition rate between v_i^T and v_k^S can be expressed via Fermi's golden rule:

$$k_{ik} = \frac{2\pi}{\hbar} \left| \left\langle \Psi_{\text{el}}^S \Psi_{\text{spin}}^S \middle| \hat{H}_{\text{SM}} \middle| \Psi_{\text{el}}^T \Psi_{\text{spin}}^T \right\rangle \right|^2 \left| \langle v_k^S | v_i^T \rangle \right|^2 \delta\left(E_i - E_k\right) \tag{2.9}$$

Here, $\hat{H}_{\text{SM}}$ is the Hamiltonian describing the spin-mixing mechanism such as spin–orbit coupling or hyperfine interaction. $\delta\left(E_i - E_k\right)$ is the Dirac delta function ensuring that RISC only takes place between isoenergetic vibrational states.

In order for such a transition to take place, the state v_i^T needs to be populated. Therefore, the population probability $p(v_i^T)$ according to Boltzmann statistics needs to be considered:

$$p(v_i^T) = \frac{1}{Z} \exp\left(\frac{-E_i}{k_{\text{B}} T}\right), \text{ with } Z = \sum_i \exp\left(\frac{-E_i}{k_{\text{B}} T}\right) \tag{2.10}$$

Here, Z is the canonical partition function, k_{B} the Boltzmann constant, T the temperature and E_i the energy of the state v_i^T.

The total RISC rate k_{RISC} is defined via the total number of excitons that are converted per time from a triplet spin configuration to a singlet spin configuration. One obtains k_{RISC} by taking the sum over all pairs v_i^T and v_k^S, while taking into account Boltzmann statistics [33]:

$$k_{\text{RISC}} = \sum_i \sum_k \frac{2\pi}{\hbar} \left| \left\langle \Psi_{\text{el}}^S \Psi_{\text{spin}}^S \middle| \hat{H}_{\text{SM}} \middle| \Psi_{\text{el}}^T \Psi_{\text{spin}}^T \right\rangle \right|^2 \frac{1}{Z} \exp\left(\frac{-E_i}{k_{\text{B}} T}\right) \left| \langle v_k^S | v_i^T \rangle \right|^2 \delta\left(E_i - E_k\right) \tag{2.11}$$

Equation 2.11 is accurate, however, not always practical. A simplified expression for k_{RISC} can be derived from the following considerations. On the one hand, vibrational levels ν_i^T that energetically lie below the S_1 state have no isoenergetic partner ν_k^S. Those states are irrelevant for RISC. On the other hand, vibrational levels ν_i^T that energetically lie far above S_1 are unlikely to be populated at ambient temperatures. Those states are negligible. The only vibrational levels ν_i^T that are relevant for RISC are the ones that are close to the zeroth vibrational level ν_0^S of the S_1 state. In that case, the Boltzmann factor is determined by the singlet–triplet gap: $\exp\frac{-\Delta E_{\mathrm{ST}}}{k_{\mathrm{B}}T}$. The matrix elements in **Equation 2.11**, the canonical partition function and the natural constants can be summarized in a single prefactor k^0_{RISC}. Then the total RISC rate can be written as:

$$k_{\mathrm{RISC}} = k^0_{\mathrm{RISC}} \exp\left(\frac{-\Delta E_{\mathrm{ST}}}{k_{\mathrm{B}}T}\right) \tag{2.12}$$

This is a commonly found form of k_{RISC} in literature. It is often sufficiently accurate, while more practical than **Equation 2.11**.

In simplified Jablonski diagrams, vibrational levels are not included and RISC is typically indicated by a vertical arrow from T_1 to S_1, as shown in **Figure 2.4**.

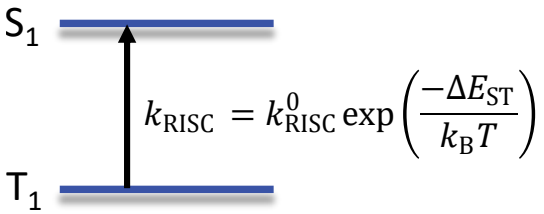

Figure 2.4: Simplified representation of RISC as a vertical arrow from T_1 to S_1 in a Jablonski diagram.

Non-radiative Decay

For OLEDs, the radiative decay of excitons is the desired transition. However, non-radiative decay channels compete with radiative transitions. The singlet state S_1 can undergo a non-radiative transition to the S_0 state. This decay is a two-step process. First a transition from the lowest vibrational level of the S_1 state to a higher excited vibrational level of the singlet ground state S_0 takes place (IC). Subsequently, the molecule relaxes to the lowest vibrational level of the singlet ground state S_0 (VR). For simplicity this two-step process is often indicated as a single vertical transition in Jablonski diagrams. Similarly, excited triplet states can decay non-radiatively via a two-step pro-

cess. Here, ISC occurs from the lowest vibrational level of the T_1 state to an isoenergetic higher vibrational level of the singlet ground state S_0 followed by vibrational relaxation to the lowest vibrational level of the singlet ground state. The rate of non-radiative transitions k_{nr} was empirically found to exponentially increase with temperature [28]:

$$k_{\mathrm{nr}} = k_{\mathrm{nr}}^{0} + k_{\mathrm{nr}}' \exp\left(\frac{E\mathrm{a}}{k_{\mathrm{B}}T}\right) \tag{2.13}$$

Here, k_{nr}^{0} and k_{nr}' are temperature-independent parameters and E_{A} is an activation energy.

In a real molecule, all of the above processes coexist. The relative magnitudes of the corresponding rates define the dominant process.

2.5 Working Principle of OLEDs

The previous section introduced excitonic states in organic molecules, as well as transitions between them. The aim of this section is to explain how excitons can be electrically generated and used for light emission in OLEDs. Electroluminescence (EL) is light emission resulting from the electrical injection and recombination of charge carriers. A typical OLED layer structure and the relevant processes leading to electroluminescence are illustrated in **Figure 2.5**.

The generation of light from an OLED can be separated into four fundamental steps that are indicated in **Figure 2.5**: (i) charge injection, (ii) charge transport, (iii) exciton formation and (iv) radiative recombination. Those four steps are explained in more detail in the following.

(i) Charge Carrier Injection

The first step towards EL is the injection of electrons and holes from an electrode into the organic layers. For injection of electrons a metal with low work function Φ_{C} such as Aluminum is often used as a cathode. For injection of holes from the anode a high work function Φ_{A} is required. Here, Indium–Tin Oxide (ITO) is frequently used because it provides both a low work function and optical transparency with respect to visible light [34]. The latter is needed for the outcoupling of light from the electrode. Generally, the electrode's Fermi-levels and the energy levels of the transporting states of the organic layer are not perfectly aligned. Charge carriers need to overcome a potential barrier to be injected. This barrier can be overcome via tunneling (Fowler–Nordheim-model [35]) or via thermionic emission (Richardson–Schottky-injection [36]). Both processes can be assumed to take place simultaneously if an external voltage is applied to an OLED.

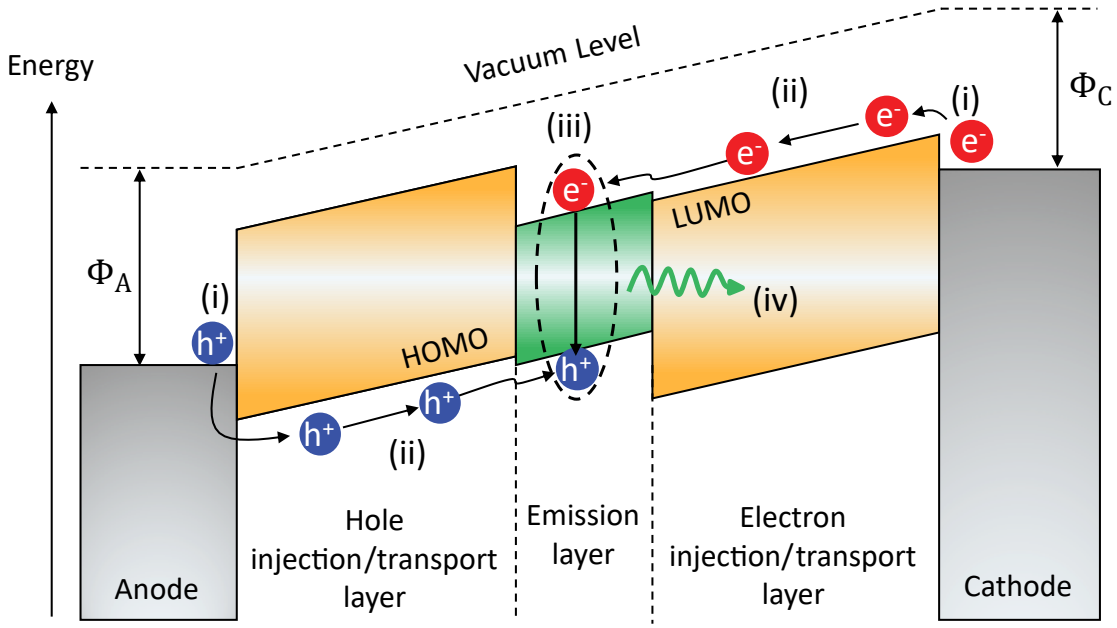

Figure 2.5: Schematic energy diagram of an OLED consisting of an anode, a cathode, injection and transport layers and an emission layer. Typically, such a layer structure is processed on top of a glass substrate, which is omitted at this point because it is not involved in the OLED's electronic circuit. Generation of electroluminescence from an OLED can be divided into four fundamental steps: (i) injection of electrons/holes from the cathode/anode into the injection layers; (ii) transport of charge carriers to the emission layer; (iii) formation of excitons; (iv) radiative recombination of excitons. Adapted from [30].

Depending on temperature and applied electric field strength one or the other mechanism dominates the overall injection [37]. An important aspect for the experiments of this thesis is the fact that the previously mentioned mechanisms of charge carrier injection include an explicit temperature-dependence. This needs to be considered in the interpretation of EPR experiments on OLEDs.

(ii) Charge Transport

After injection of charge carriers from electrodes to organic layers, electrons and holes need to be transported to an emission layer where they can eventually recombine. OLED layers are usually disordered amorphous films. Band-like transport, as found in conventional inorganic semiconductors, doesn't apply. Instead, transport in amorphous organic semiconductors is described as so-called hopping. Here, charge carriers are localized at individual sites whose energies are statistically distributed [38]. Transport is described as jumps between those sites. In the Miller–Abrahams model, the jump rate ν_{ij} between two sites i and j with energies ε_i and ε_j is as follows [39]:

$$\nu_{ij} = \nu_0 \exp\left(-2\gamma R_{ij}\right) \begin{cases} \exp\left(-\dfrac{\varepsilon_j - \varepsilon_i}{k_\mathrm{B} T}\right) & , \varepsilon_j > \varepsilon_i \\ 1 & , \varepsilon_j < \varepsilon_i \end{cases} . \tag{2.14}$$

ν_0 is the maximum hopping rate, γ a parameter related to the wave function overlap between the states of the two sites, R_{ij} the spatial distance between the two sites, k_B the Boltzmann constant and T the temperature. **Equation 2.14** implies that the rate of hopping between two sites is maximal for a downward jump $(\varepsilon_j < \varepsilon_i)$ and temperature-activated for an upward jump $(\varepsilon_j > \varepsilon_i)$. Therefore, the mobility of charge carriers in disordered organic systems is generally temperature-dependent. Overall, transport in disordered organic semiconductors is a highly complex subject that can be described by a series of different models [38, 40, 41]. The important point for this thesis is the fact that transport in amorphous semiconductors takes place as temperature-activated hopping, which needs to be considered in the interpretation of EPR experiments on OLEDs.

(iii) Exciton Formation

Typical OLED layer structures include a so-called emission layer that is sandwiched between the transport layers [42]. The molecules of electron and hole transport layers as well as the molecules for the emission layer are chosen such that charge carriers are energetically confined within the emission layer. Therefore, transport layers are also called blocking layers. The LUMO of the hole transport layer must be higher in energy than the LUMO of the emission layer. Equally, the HOMO of the electron transport layer must be lower in energy than the HOMO of the emission layer. This results in a confinement of electrons and holes in the emission layer which increases the probability for exciton formation. Otherwise, charge carriers can pass through the entire device without the formation of an exciton, which represents a loss mechanism that lowers the efficiency of an OLED.

(iv) Radiative Recombination

The spin of injected charge carriers is generally randomly oriented. As a result, the formation of excitons from injected charge carriers leads to an equally distributed population of the singlet state (S) and each single one of the three triplet states (T_+, T_0 and T_-). 25% of injected charge carriers form singlet states and 75% triplet states [43, 44]. As explained in **Section 2.3**, the radiative decay of triplet states to the singlet ground state is forbidden in an unperturbed system. The fact that only 25% of charge carriers form singlet states therefore poses a fundamental limitation for the efficiency of

OLEDs. The different generations of OLEDs and how this limitation can be overcome will be discussed later on.

Those four fundamental steps towards EL from an OLED are all related to processes involving charge carriers. Eventually, light needs to be coupled out of the device to be used for applications. The layers introduced in **Figure 2.5** are typically processed on top of a glass substrate. A final step towards the usage of EL from an OLED is light outcoupling through the substrate. The impact of this outcoupling process on device efficiency will be discussed later.

2.6 Quantifying OLED Efficiencies

One way to quantify the efficiency of an OLED is the external quantum efficiency (EQE). It is defined as the ratio between the number of photons n_{Ph} that are coupled out of the device and the number of charge carriers n_{inj} that are injected into the device [30]:

$$\mathrm{EQE} = \frac{n_{\mathrm{Ph}}}{n_{\mathrm{inj}}} \tag{2.15}$$

The EQE depends on different parameters, that are related to the different steps leading to EL, as discussed previously:

$$\mathrm{EQE} = \underbrace{\gamma \eta_{\mathrm{S}} \eta_{\mathrm{eff}}}_{\mathrm{IQE}} \eta_{\mathrm{out}} = \mathrm{IQE} \cdot \eta_{\mathrm{out}} \tag{2.16}$$

γ is the charge carrier balance factor, η_{S} the spin statistics factor and η_{eff} the effective radiative quantum efficiency. The product of those parameters is called internal quantum efficiency (IQE). η_{out} is the outcoupling factor.

The charge carrier balance factor γ describes the probability for injected electrons and holes to form an exciton. γ can be as high as unity if charge carriers are prevented from passing the entire device. This can be achieved by proper selection of injection, transport and blocking layers as discussed above.

The spin statistics factor η_{S} describes the fraction of excitons that are allowed to decay radiatively. As explained previously, electrical injection of charge carriers leads to the formation of singlets with a probability of 25% and triplets with a probability of 75%. For common fluorescent emitters, η_{S} is limited to 0.25. If triplet harvesting mechanisms are exploited, η_{S} can be increased up to unity.

The effective radiative quantum efficiency η_{eff} describes the relative magnitudes of radiative and non-radiative transitions rates. η_{eff} is given by:

$$\eta_{\text{eff}} = \frac{F \cdot \Gamma_{\text{r}}}{F \cdot \Gamma_{\text{r}} + \Gamma_{\text{nr}}} \tag{2.17}$$

Here, Γ_{r} is the radiative decay rate of the excited state, Γ_{nr} the sum of all competing non-radiative decay rates. F is the so-called Purcell factor, which takes into account that the environment of an OLED's emission layer (e.g. transport layers or electrodes) slightly changes the radiative transition rates [30]. η_{eff} is close to unity if $\Gamma_{\text{r}} \gg \Gamma_{\text{nr}}$.

The outcoupling factor η_{out} considers the fact that only a fraction of the light that is generated in the organic layers leaves the device. This is due to the differences in refractive index of the organic layers and the glass substrate as well as air. When light from the emission layer hits the glass substrate, a certain amount will be reflected back into the organic layers. Based on a simple ray optics model, η_{out} is found to be [45]:

$$\eta_{\text{out}} = \frac{1}{2n^2} \tag{2.18}$$

Here, n is the average refractive index of the organic layers. Typical values are in the range of n = 1.6–1.8 leading to η_{out} = 0.15–0.2. This implies a major limitation for the EQE of OLEDs. All parameters in **Equation 2.16** can theoretically be brought to unity by proper selection and design of materials with the exception of the outcoupling factor. It might be improved beyond 0.2 by sophisticated design of macroscopic lenses on the glass substrate, but those approaches are not always practical or too expensive for actual OLED applications [46, 47]. Furthermore, molecules with a preferred direction of emission related to morphology can exhibit enhanced outcoupling factors [48, 49, 50]. The EQE of OLEDs with conventional structures, however, is limited to approximately 20%.

2.7 The Different Generations of OLEDs

After the first OLEDs had been realized, the one EQE parameter that offered the most potential for improvement was the singlet/triplet factor $\eta_{\text{S/T}}$. In conventional fluorescent OLEDs, it is limited to 25% because triplet states do not contribute to light generation. The goal therefore was to find ways to harvest triplet states. This led to the development of first phosphorescent OLEDs and later on TADF OLEDs. This section will give an overview of the different generations of OLEDs and the involved excited states. The light generation mechanisms for each type of OLED are illustrated by the simplified Jablonski diagrams in **Figures 2.6**-**2.8**. In each figure, black circles indicate the singlet-to-triplet generation ratio of 1:3.

Fluorescence Emitters – 1st Generation OLEDs

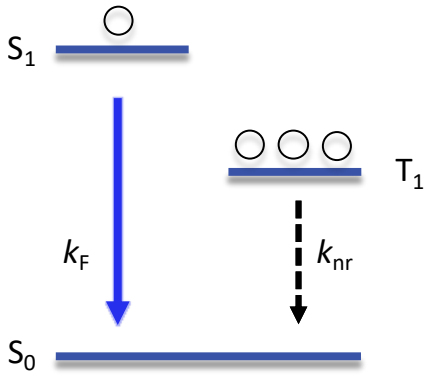

Figure 2.6: Simplified Jablonski diagram for fluorescence OLEDs. Singlets decay radiatively while triplets are lost via non-radiative decay.

OLEDs based on fluorescence were the first to be developed and are therefore referred to as 1st generation OLEDs [51, 4]. They employ the radiative decay of singlet excited states S_1 (see **Figure 2.6**). Fluorescence emitters do not intrinsically exhibit spin-mixing perturbations. The radiative decay of triplet excited states is therefore not enabled which is why triplets are lost via non-radiative decay. The singlet–triplet gap ΔE_{ST} for the respective molecules is typically in the range of several hundreds of m*e*V. The probability for thermal activation and RISC from triplet to singlet is therefore negligibly small. The spin statistics factor η_S for fluorescence emitters is 25%. Consequently, the IQE of fluorescence-based OLEDs is limited to a maximum of 25%. The EQE = IQE $\cdot \eta_{out}$ is therefore limited to approximately 5%.

Phosphorescence Emitters – 2nd Generation OLEDs

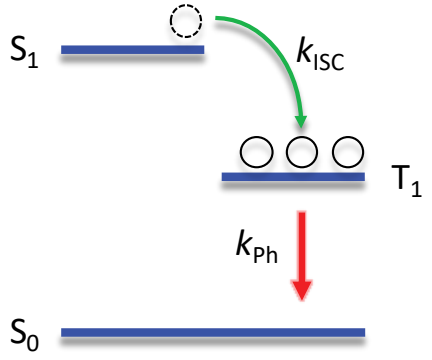

Figure 2.7: Simplified Jablonski diagram for phosphorescence OLEDs. Singlets are converted to triplets via ISC. Triplets decay radiatively via phosphorescence.

Phosphorescence emitters are based on the radiative decay of excited triplet states T_1 (see **Figure 2.7**) [5, 52]. Here, the transition from excited triplet to singlet ground state is enabled by spin–orbit coupling. This is achieved by the inclusion of heavy metal atoms, such as iridium or platinum, into organic compounds. Because of efficient spin–orbit coupling, the ISC rate considerably increases. ISC from S_1 to T_1 even exceeds the radiative decay rate from S_1 to S_0. All singlets are converted to triplets and light emission solely stems from phosphorescence. The spin statistics factor η_S for phosphorescence-based OLEDs can be as high as 1. Accordingly, IQE values reach 100% and EQE values around 20%. Phosphorescence based OLEDs were developed to overcome the efficiency limit of fluorescence-based OLEDs and are also called 2nd generation OLEDs.

TADF Emitters – 3rd Generation OLEDs

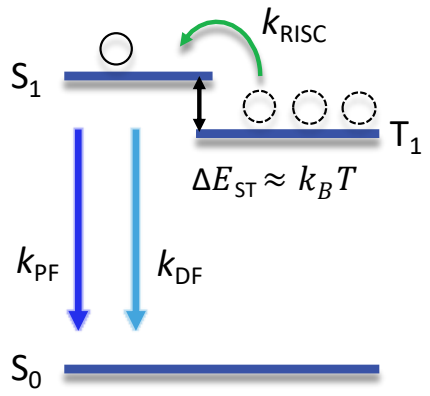

Figure 2.8: Simplified Jablonski diagram for TADF OLEDs. Singlets decay radiatively as prompt fluorescence (PF). Triplets are converted to singlets via RISC followed by a radiative decay as delayed fluorescence (DF).

Light generation of TADF emitters is based on two processes. The first is so-called prompt fluorescence, which is the radiative decay of initially created singlets S_1. The second is so-called thermally activated delayed fluorescence (TADF) resulting from the radiative decay of singlets S_1 that are populated via thermally activated RISC from the T_1 state [10, 11]. This working principle of TADF OLEDs is illustrated in **Figure 2.8**. The underlying process of RISC was explained in detail in **Section 2.4**. In order for RISC to be efficient, the singlet–triplet gap ΔE_{ST} needs to be minimized to values in the range of thermal energy $k_B T$. Furthermore, a spin-mixing perturbation within the system is needed. The spin statistics factor η_S for TADF-based OLEDs can reach unity if all triplets are harvested. Therefore, IQE values reach 100%, and EQE values around 20%. TADF OLEDs followed phosphorescence emitters and are also called 3rd generation OLEDs.

2.8 Transition Rates of TADF Emitters

A more formal and more accurate description for TADF emitters is shown in **Figure 2.9**. Here, all rates that are relevant for the efficiency of TADF emitters are included.

There are three relevant depopulation channels for excitons in the singlet state S_1. The first is the radiative decay to the singlet ground state S_0 with the rate k_F. However, a non-radiative transition to the singlet ground state with a rate k_{nr}^S is possible as well. The third process is ISC to the triplet state with a rate k_{ISC}. For excitons in the triplet state T_1, there are three relevant depopulation mechanisms. First, triplets can be converted to singlet states via RISC with a rate k_{RISC}. This process is, however, only available to higher excited vibrational triplet sublevels v_i that are at least isoenergetic with the lowest vibrational level of the first excited singlet state S_1 (see detailed description of RISC in **Section 2.4**). The number of triplet excitons, which are available for RISC, is proportional to the Boltzmann term $\exp(-\Delta E_{ST}/k_B T)$. Another important depopulation mechanism is the non-radiative transition to the singlet ground state S_0 with a rate k_{nr}^T. Finally, triplets can decay radiatively via phosphorescence with a rate

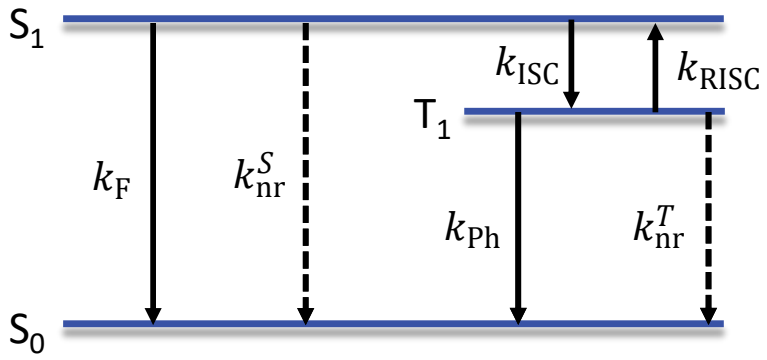

Figure 2.9: Jablonski diagram including the most relevant transitions for a TADF emitter. Singlets can decay radiatively as fluorescence with a rate k_F, decay non-radiatively with a rate k_{nr}^S or undergo ISC with a rate k_{ISC}. Triplets can decay radiatively as phosphorescence with a rate k_{Ph}, decay non-radiatively with a rate k_{nr}^T or be converted to singlets via RISC with a rate k_{RISC}.

k_{Ph}, which is typically very low for TADF emitters, might however become relevant at low temperatures [53]. If a TADF emitter is optically excited or a TADF-based OLED is electrically driven, generation rates G have to be added. For optical excitation, there is a generation rate from S_0 to S_1, while the excitation of T_1 is spin-forbidden. For electrical injection, there are generation rates for S_1 and T_1 with a ratio of 1:3. For both optical excitation and electrical generation, all of the above described transitions coexist and a stationary state is reached where the population of all of the involved states is constant in time. The relative magnitudes of the rates for all radiative and non-radiative transitions eventually determine the efficiency of a TADF system. The optimization of those rates by molecular design will be discussed in the following section.

2.9 Molecular Design of TADF Emitters

TADF relies on triplet-to-singlet conversion via RISC and the subsequent radiative decay of singlets. Three material properties make this process efficient [54]:

(i) sufficiently small singlet–triplet gap ΔE_{ST}
(ii) sufficiently large transition dipole moment $\mu_{S_1-S_0}$
(iii) sufficiently strong spin-mixing

These three requirements are needed for k_{RISC} to outcompete the non-radiative decay rate of triplets k_{nr}^T and for k_F to outcompete the non-radiative decay rate of singlets k_{nr}^S. If these criteria are fulfilled, a TADF-based OLED can achieve an IQE of 100%. All of the three requirements (i)-(iii) need to be considered in the molecular design of TADF emitters.

Singlet–Triplet Gap ΔE_{ST}

ΔE_{ST} is proportional to the overlap between HOMO and LUMO of an organic molecule (see **Section 2.2**, **Equation 2.3**). In order to minimize ΔE_{ST}, HOMO and LUMO need to be spatially separated. This has been addressed with a series of different approaches, which can be divided into two categories: intramolecular and intermolecular TADF emitters. Both approaches are illustrated in **Figure 2.10**.

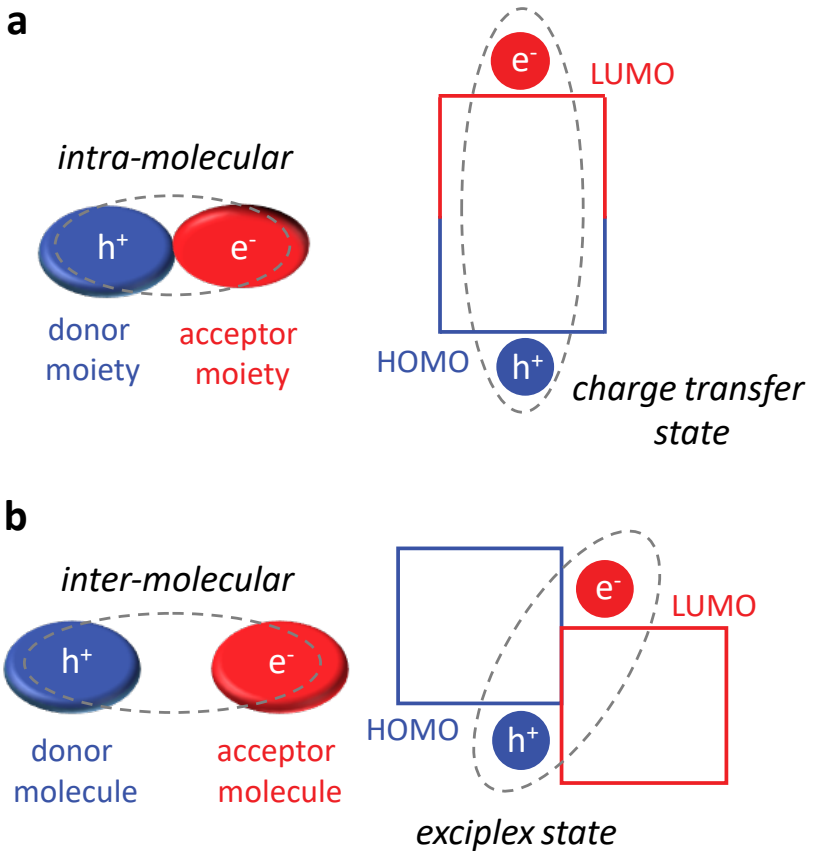

Figure 2.10: Molecular design approaches for TADF emitters. **a**, Intramolecular TADF emitters. A charge transfer state is formed on a single molecule that consists of a donor and an acceptor moiety. A twist between the two moieties minimizes the HOMO–LUMO overlap and accordingly ΔE_{ST}. **b**, Intermolecular TADF emitters. An exciplex state is formed between a donor and an acceptor molecule. The distance between donor and acceptor results in a small HOMO–LUMO overlap and a small ΔE_{ST}.

The first rely on *charge transfer* (CT) states on a single molecule (**Figure 2.10a**). Here, the idea is to design molecules that have spatially separated donor and acceptor moieties. This can be achieved for instance by sterical hindrance that induces a twist between donor and acceptor unit [11, 55, 56]. In such a case, conjugation over the molecule is broken and the HOMO is mostly located on the donor moiety whereas the LUMO is located on the acceptor moiety. As a result, the HOMO–LUMO overlap is

minimized and accordingly ΔE_{ST}. The emissive state is a charge transfer state where the electron is located on the acceptor and the hole on the donor moiety.

Figure 2.10b illustrates intermolecular TADF emitters. Here, the spatial separation of HOMO and LUMO is achieved via the formation of CT excitons where electron and hole are located on two different adjacent molecules [10, 57]. The emissive state is formed by an exciton where the electron is located on the acceptor and the hole on the donor molecule. In this context, such CT states are also referred to as *exciplex* states.

Transition Dipole Moment $\mu_{S_1-S_0}$

By following the above described design rule, a $\Delta E_{ST} = 0$ is possible if HOMO and LUMO are fully spatially separated. This case is beneficial for k_{RISC}, however, one has to keep in mind that the transition dipole moment $\mu_{S_1-S_0}$ is proportional to the HOMO–LUMO overlap as well (see **Section 2.3**, **Equation 2.8**). Fully spatially separated HOMO and LUMO imply $\mu_{S_1-S_0} = 0$, which means that the S_1 state cannot decay radiatively into the S_0 state ($k_F = 0$). It is therefore necessary to find a proper trade-off between ΔE_{ST} and $\mu_{S_1-S_0}$ [58, 59]. Nevertheless, it is typically sufficient for HOMO and LUMO to deviate only slightly from a fully separated configuration ensuring a near-zero ΔE_{ST} with reasonably high $\mu_{S_1-S_0}$ [56].

Spin-Mixing

Unlike in phosphorescence based OLEDs, TADF emitters do not require the inclusion of heavy-metal atoms to induce spin–orbit coupling. Nevertheless, some form of spin-mixing mechanism is needed to drive the spin-conversion from triplet to singlet during the RISC process. The exact role of spin-mixing for TADF has been subject to a lot of debate throughout the development of TADF OLEDs. Spin–orbit-coupling [22, 23, 24], hyperfine interaction [25] and Δ-g mechanism [60] have been proposed to be responsible for spin-conversion in TADF emitters. A straight-forward molecular design rule that ensures sufficient spin-mixing has not been established yet. This issue will be addressed in the experiments presented in this thesis.

2.10 Time-Resolved Luminescence of TADF Emitters

Light generation of TADF emitters is based on prompt fluorescence (PF) and delayed fluorescence (DF). These two processes can be distinguished in time-resolved (tr) experiments. Both tr-photoluminescence (trPL) and tr-electroluminescence (trEL) are

commonly applied to study TADF systems. Such measurements reveal time scales of processes in the investigated systems. This information is valuable for proper interpretation of EPR experiments on TADF systems.

In trPL, a thin film consisting of the emitter molecule is optically excited with a pulsed laser and the time decay of PL following excitation is recorded. In trEL, a pulsed voltage is applied to a fully processed device and the time decay of EL after switching off the voltage is recorded. The time-dependent luminescence L for a TADF system can be modeled with a bi-exponential decay [31, 61]:

$$L(t) = A_{\mathrm{PF}} \exp\left(-\frac{t}{\tau_{\mathrm{PF}}}\right) + A_{\mathrm{DF}} \exp\left(-\frac{t}{\tau_{\mathrm{DF}}}\right) \tag{2.19}$$

Here, $A_{\mathrm{PF}}/A_{\mathrm{DF}}$ and $\tau_{\mathrm{PF}}/\tau_{\mathrm{DF}}$ are the amplitude and the time constant of prompt/delayed fluorescence. τ_{PF} is typically in the range of nanoseconds and τ_{DF} in the range of microseconds. **Figure 2.11** shows normalized plots of **Equation 2.19** with representative values of $\tau_{\mathrm{PF}} = 20$ ns and $\tau_{\mathrm{DF}} = 5$ μs.

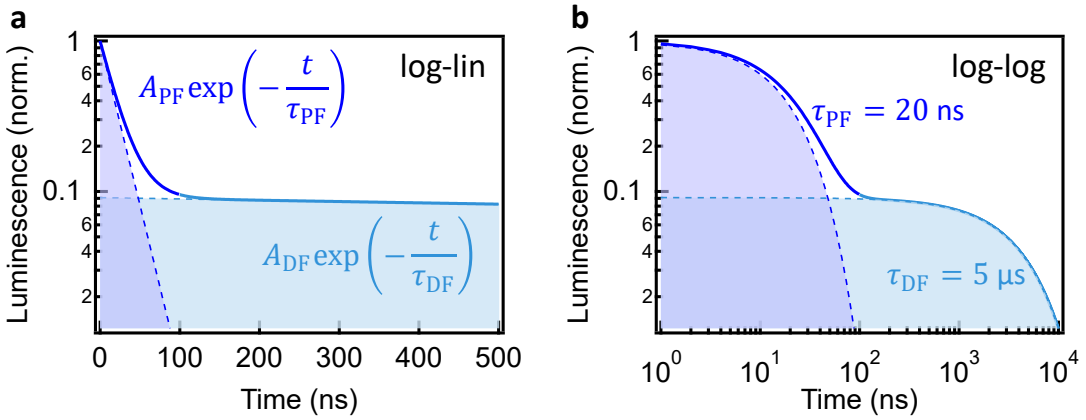

Figure 2.11: Time-resolved luminescence $L(t)$ for a TADF emitter according to **Equation 2.19**. **a**, log-lin plot of $L(t)$. At early times, $L(t)$ follows a line with a slope of $-1/\tau_{\mathrm{PF}}$, while at late times $L(t)$ follows a line with a slope of $-1/\tau_{\mathrm{DF}}$. **b**, log-log plot of $L(t)$. Graphical presentations adapted from [53].

In order to distinguish the features of PF and DF, time-resolved luminescence curves are commonly shown in a log-lin (**Figure 2.11a**) or log-log (**Figure 2.11b**) representation [53]. The early part of such transients is determined by PF, while at later times DF dominates.

Arrhenius Plots

The observation of DF by itself is an indication for TADF however no sufficient proof. Triplet–triplet-annihilation (TTA) can induce DF as well [62, 63, 64]. Temperature-dependent measurements are needed to show that DF is temperature-activated.

From those experiments the temperature-dependent RISC rate k_{RISC} or a quantity that is proportional to k_{RISC} is determined. A so-called Arrhenius plot is commonly used to quantitatively analyze temperature-dependent experiments on TADF systems.

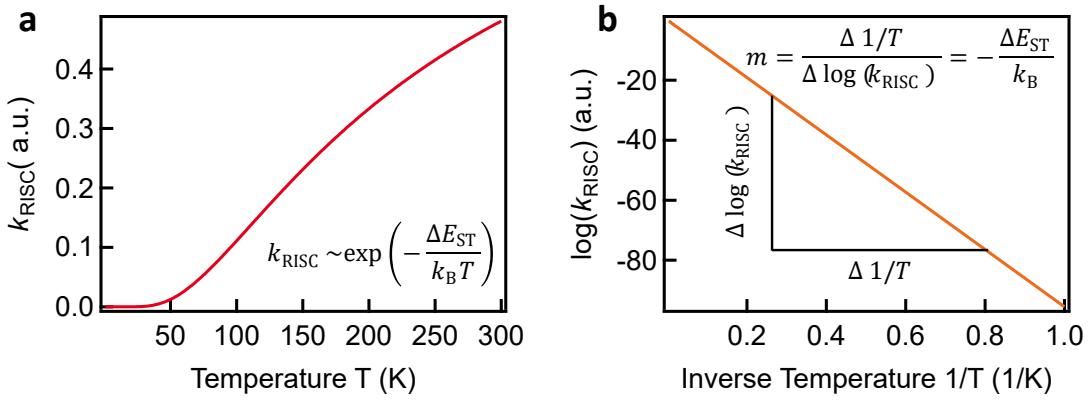

Figure 2.12: Determination of ΔE_{ST} via an Arrhenius plot. **a**, The RISC rate k_{RISC} depends exponentially on the inverse temperature. **b**, Plotting the logarithm of k_{RISC} vs. the inverse temperature yields a straight line. ΔE_{ST} can be obtained from the slope m of that line.

Arrhenius plots, in the context of TADF, are based on the following consideration:

$$k_{\mathrm{RISC}} = k^0_{\mathrm{RISC}} \exp\left(\frac{-\Delta E_{\mathrm{ST}}}{k_{\mathrm{B}}T}\right) \Rightarrow \log(k_{\mathrm{RISC}}) = \log\left(k^0_{\mathrm{RISC}}\right) - \frac{\Delta E_{\mathrm{ST}}}{k_{\mathrm{B}}T} \tag{2.20}$$

Plotting $\log(k_{\mathrm{RISC}})$ vs. the inverse temperature $1/T$ yields a linear dependence with a slope $m = -\Delta E_{\mathrm{ST}}/k_{\mathrm{B}}$ (see **Figure 2.12**). Extracting k_{RISC} or a quantity that is proportional to k_{RISC} from temperature-dependent experiments can therefore be used to determine ΔE_{ST} from the slope of an Arrhenius plot.

2.11 Photometric Quantities and Color Coordinates

The most promising applications of OLEDs are displays and room lighting. Human perception of light and color are central for these applications. It is therefore important to characterize the emission properties of OLEDs with respect to the wavelength-selective sensitivity of the human eye. This is considered in so-called photometric quantities as well as in color coordinates.

Photometric Quantities

Radiometry describes various properties of a sample's electromagnetic radiation. One of the simplest so-called *radiometric* quantities is the *radiant flux* Φ_e, which is defined as the total energy emitted by a sample per time in units of watt (W). Each radiometric quantity has a so-called *photometric* analogue that describes the same optical property, however, weighted with the wavelength-dependent sensitivity of the human eye. The photometric analogue to the radiant flux Φ_e is the so-called *luminous flux* Φ_v. Radiometric quantities are typically denoted with the subscript 'e' for *electromagnetic* and photometric ones with 'v' for *visual*. The connection between Φ_e and Φ_v is defined by the following integral [28]:

$$\Phi_v = K_m \int \Phi_e(\lambda) V(\lambda) d\lambda, \tag{2.21}$$

Here, λ is the wavelength. $K_m = 683$ lm/W is a scaling factor that converts units between lumens (lm) and watts (W). $V(\lambda)$ is called luminous efficiency function and describes the average spectral sensitivity of the human eye in daylight. $V(\lambda)$ is shown in **Figure 2.13**.

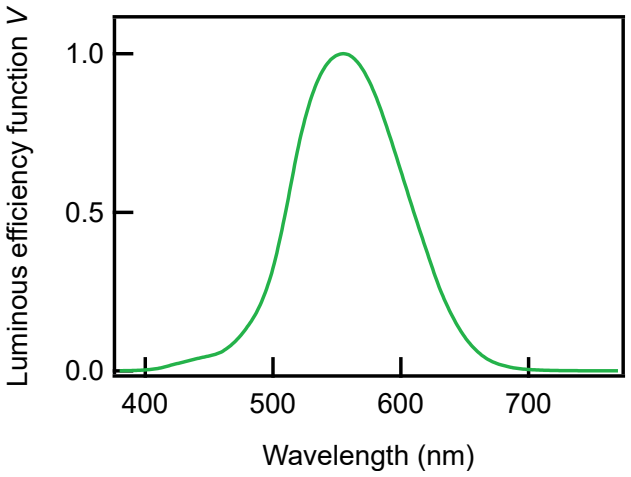

Figure 2.13: Wavelength-dependent luminous efficiency function V which is a dimensionless quantity describing the human eye's spectral sensitivity. Dataset for V is taken from [65].

A suitable photometric quantity to characterize an OLED's emission strength is the *luminance* L_v. It is formally defined as [28]:

$$L_v = \frac{1}{\cos(\theta)} \frac{d^2\Phi_v}{d\Omega dA} \tag{2.22}$$

In words, L_v describes an emitter's luminous flux Φ_v per unit solid angle $d\Omega$ normalized to the emitting surface area dA where θ is the angle between the surface nor-

mal of the emitting area dA and the direction of the solid angle $d\Omega$. L_v is given in units of lumen per steradian and per square meter (lm/sr·m^2), which equals candela per square meter (cd/m^2), with cd= lm/sr. Generally, the luminance is a direction-dependent quantity. OLEDs are, however, so-called *Lambertian* emitters, which means $L_v(\theta)$ =const [45, 66]. Intuitively, this means that an OLED appears equally bright, no matter from which direction an observer looks at it. L_v is therefore a suitable measure to quantify OLED brightness.

Color Coordinates

OLED applications demand a quantitative standardized measure of the emission color. For example, each pixel in modern displays consists of three independent monochromatic light-emitting diodes: red, green, and blue. Therefore, one has to (pre-)select optimal emitters by their color characteristics based on the emission spectrum. There are different approaches to classify an emission spectrum within a defined color space. One of the most commonly used approaches for OLEDs is the CIE1931 color space (Commission Internationale de l'Eclairage) [67, 68]. It relies on the three so-called *color matching functions* $\overline{x}(\lambda)$, $\overline{y}(\lambda)$ and $\overline{z}(\lambda)$. Those functions are related to the human eye's perception of the colors red, green and blue. Their wavelength dependence is shown in **Figure 2.14a**.

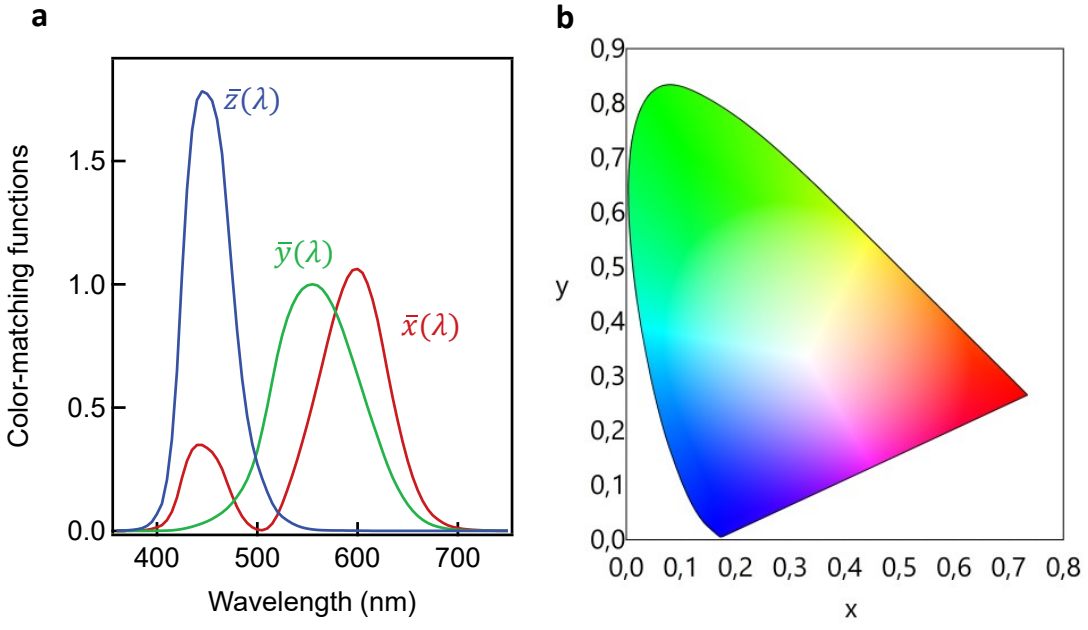

Figure 2.14: CIE1931 color coordinates. **a**, Color-matching functions $\overline{x}(\lambda)$, $\overline{y}(\lambda)$ and $\overline{z}(\lambda)$. They are dimensionless quantities related to the human eye's perception of the colors red, green and blue. Datasets for color-matching functions taken from [65]. **b**, CIE1931 color diagram, taken from [69].

Based on these color-matching functions, three so-called tristimulus values X, Y and Z can be defined by the following integrals:

$$\begin{aligned} X &= \int \overline{x}(\lambda) L_{\mathrm{e}}(\lambda)\, d\lambda \\ Y &= \int \overline{y}(\lambda) L_{\mathrm{e}}(\lambda)\, d\lambda \\ Z &= \int \overline{z}(\lambda) L_{\mathrm{e}}(\lambda)\, d\lambda \end{aligned} \tag{2.23}$$

Here, L_{e} denotes a sample's *radiance*, which is the radiometric analogue to the photometric luminance L_{v}. The radiance $L_{\mathrm{e}}(\lambda)$ can be viewed as an OLED's emission spectrum in units of W/sr·m^2. Finally, the tristimulus values allow the calculation of the color coordinates x, y and z according to the following equations:

$$\begin{aligned} x &= \frac{X}{X+Y+Z} \\ y &= \frac{Y}{X+Y+Z} \\ z &= \frac{Z}{X+Y+Z} \end{aligned} \tag{2.24}$$

These equations imply that $z = 1 - x - y$. Accordingly, the color coordinates, associated with a sample's radiance $L_{\mathrm{e}}(\lambda)$, are fully described by the two values x and y. These two values define a color in the CIE1931 color diagram, as shown in **Figure 2.14b**. Depending on the desired application, the color coordinates x and y of a TADF emitter need to be in a certain range for the emitter to be considered suitable for this application.

Another concept that is used to describe the human perception of color is the so-called *correlated color temperature* (CCT). The CCT is defined as the temperature of an ideal black body radiator whose emission spectrum most closely resembles the emission of the light source that is characterized [70]. The determination of a light source's CCT value is commonly used in the development of white light emitters. It provides a quantitative measure for how "warm" or "cold" a white light source is perceived. Low CCT values (around 2000 K) represent "warm white" light sources while high CCT values (around 4000 K) represent "cold white" light sources. For instance, the emission spectrum of a candle has a CCT value of around 1900 K and is considered as "warm white". The CCT can be approximated by using the color coordinates x and y [71]:

$$\mathrm{CCT} = a n^3 + b n^2 + c n + d, \quad \text{with} \quad n = \frac{x - x_e}{y - y_e} \tag{2.25}$$

With the parameters $a = 449$, $b = 3525$, $c = 6823.3$, $d = 5520.33$, $x_e = 0.3320$ and $y_e = 0.1858$, this equation yields a reasonably accurate approximation for CCT.

3 Electron Paramagnetic Resonance

Most of the experiments presented in this work are based on the method of electron paramagnetic resonance (EPR). The idea of EPR is to energetically split spin states in an external magnetic field and induce transitions between those spin states via microwaves. Every intrinsic or optically and electrically excited spin species yields a specific EPR spectrum. EPR spectroscopy therefore allows to identify spin species and reveal their impact on spin-dependent processes in the investigated material.

The purpose of this chapter is to introduce the theory that is needed to understand the origin and structure of EPR spectra for a specific spin type. Since TADF emitters rely on RISC, the spin species of interest in this thesis are triplet states. The first part of this chapter explains the most relevant interactions that determine the energetic structure of triplet states. Afterwards, the concept of microwave absorption between triplet substates in an external magnetic field is explained. Here, a special focus is on the line shape of the detected absorption spectra. Finally, EPR detection methods that are most suitable for the investigation of TADF OLEDs are introduced.

The explanation of EPR fundamentals is mostly based on the textbook "Electron Paramagnetic Resonance - Elementary Theory and Practical Applications" by John R. Weil, James R. Bolton and John E.Wertz [27], as well as the online documentation for the EPR software package "easyspin" from Stefan Stoll [72].

3.1 Electron Zeeman Interaction

The most fundamental principle of EPR is the so-called *electron Zeeman interaction* (EZI). It describes the dependence of a spin state's energy on an external magnetic field. Generally, EZI stems from a particle's magnetic moment, which is composed of both orbital angular momentum and spin angular momentum. In the context of this work, however, only spin angular momentum is relevant. In that case, EZI for a spin system is mathematically described by the EZI Hamiltonian $\mathscr{H}_{\mathrm{EZI}}$:

$$\mathscr{H}_{\mathrm{EZI}} = \mu_B \cdot \mathbf{B} \cdot \mathbf{g} \cdot \hat{\mathbf{S}} \tag{3.1}$$

Here, μ_B is the Bohr magneton, $\mathbf{B}$ the vector of the external magnetic field, $\mathbf{g}$ the g-tensor and $\hat{\mathbf{S}}$ the spin operator for the considered spin system. For a free electron, the g-tensor can be reduced to a single value of $g_e = 2.002319...$ [27]. The g-tensor accounts for the influence of a spin's environment. In molecules or solid state systems, the externally applied magnetic field $\mathbf{B}$ is superimposed with local magnetic fields $\mathbf{B}_{\mathrm{local}}$ that originate from the spin system's surrounding. The strength of such local fields is typically small compared to the external field. Therefore, one can describe them by a g-tensor, rather than explicitly taking $\mathbf{B}_{\mathrm{local}}$ into account. Because local magnetic fields are anisotropic, a g-tensor, rather than a g-factor is generally needed to describe a spin system accurately. For the experiments in this work, it is, however, mostly sufficient to consider a single g-factor g that slightly deviates from g_e. In that case, the eigenenergies E_{Z} for the EZI Hamiltonian in **Equation 3.1** are given by:

$$E_{\mathrm{Z}} = \mu_B g m_s B_0, \tag{3.2}$$

where m_s is the spin system's magnetic quantum number and B_0 the absolute value of the magnetic field.

3.2 Zero-Field Interaction

In multi-particle systems, spin–spin interaction needs to be considered in order to describe the energy of the corresponding spin states accurately. This interaction is called *zero-field interaction* (ZFI), because it exists independently from external magnetic fields. It is sometimes also called dipole–dipole coupling, because it results from the interaction between magnetic dipole moments of two spins. Mathematically, ZFI can be described via the following Hamiltonian $\mathscr{H}_{\mathrm{ZFI}}$ and the zero-field tensor $\mathbf{D}$:

$$\mathscr{H}_{\mathrm{ZFI}} = \hat{\mathbf{S}}^T \mathbf{D} \hat{\mathbf{S}} = \begin{pmatrix} S_x & S_y & S_z \end{pmatrix} \begin{pmatrix} D_{xx} & D_{xy} & D_{xz} \\ D_{yx} & D_{yy} & D_{yz} \\ D_{zx} & D_{zy} & D_{zz} \end{pmatrix} \begin{pmatrix} S_x \\ S_y \\ S_z \end{pmatrix}, \tag{3.3}$$

Here, $\hat{\mathbf{S}}$ is the spin operator of the spin system. **Equation 3.3** describes ZFI in it's most general form. However, $\mathbf{D}$ can be conveniently transformed to a traceless symmetric matrix, which is fully described by the two zero-field splitting parameters D and E:

$$\boldsymbol{D} = \begin{pmatrix} D_x & 0 & 0 \\ 0 & D_y & 0 \\ 0 & 0 & D_z \end{pmatrix} = \begin{pmatrix} -\frac{1}{3}D + E & 0 & 0 \\ 0 & -\frac{1}{3}D - E & 0 \\ 0 & 0 & \frac{2}{3}D \end{pmatrix} \tag{3.4}$$

The most relevant spin systems for this thesis are excitons consisting of an electron and a hole spin. As explained in **Chapter 2**, **Section 2.2**, the spin states of a two-spin system can be divided into one singlet (S) and three triplet (T_-, T_0, T_+) states. ZFI impacts only triplet states, while it vanishes for singlet states. The energies $\varepsilon_{\pm,0}$ of the three triplet states resulting from **Equations 3.3** and **3.4** are:

$$\begin{aligned} \varepsilon_+ &= \frac{1}{3}D + E \\ \varepsilon_0 &= -\frac{2}{3}D \\ \varepsilon_- &= \frac{1}{3}D - E \end{aligned} \tag{3.5}$$

The individual contributions of D and E to the triplet energies are illustrated in **Figure 3.1**.

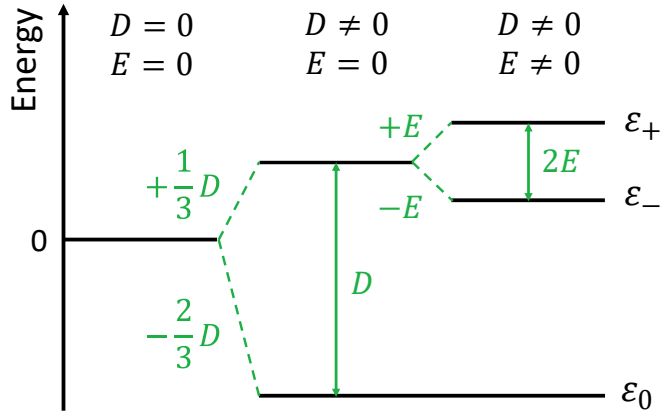

Figure 3.1: Effects of zero-field interaction on the triplet energies ε_+, ε_0 and ε_-. The zero-field splitting parameters lift the degeneracy of the triplet energies at zero magnetic field.

For the systems investigated in this work E is negligibly small, whereas D has a significant influence on the shape of EPR spectra, as will be explained later on. It is therefore important to know which parameters determine D. One can show that D is given by the following equation [73]:

$$D = \frac{3\mu_0}{16\pi h} \frac{g_a g_b \mu_B^2}{r_{ab}^3} \left(1 - 3\cos^2\theta\right) \tag{3.6}$$

Here, μ_0 is the permeability constant, h Plank's constant, g_a and g_b the g-factors of the two spins forming a triplet, μ_B the Bohr magneton, r_{ab} the distance between the two spins and θ the angle between the vector connecting the two spins and the vector of an external magnetic field. In ordered organic systems the angle dependence of D can be used to study certain properties of the investigated organic material. The organic systems studied in this thesis are, however, amorphous films consisting of small molecules. In that case, the angle θ is randomly distributed and different for each exciton. Therefore, no dependence of the EPR spectrum on the angle between the magnetic field and the sample orientation is expected. For this work, the most relevant parameter in **Equation 3.6** is the distance r_{ab}. The determination of D from EPR spectra allows to calculate r_{ab}, which can be used to distinguish between different types of excitons, as will be discussed in more detail later.

3.3 EPR Transitions between Triplet States

EPR is based on the resonant excitation of transitions between spin states that are split in an external magnetic field. Combining the previously described Zeeman and zero-field interactions, the energies E_+, E_0 and E_- for the triplet states T_+, T_0 and T_- are [74]:

$$\begin{aligned} E_+ &= \frac{1}{3}D + \mu_B g B \\ E_0 &= -\frac{2}{3}D \\ E_- &= \frac{1}{3}D - \mu_B g B \end{aligned} \tag{3.7}$$

Here, the zero-field splitting parameter E is assumed to be zero. According to spin-selection rules (the change of magnetic quantum number Δm_s needs to be ± 1), only transitions between the T_0 triplet and the T_+ or T_- triplet are allowed [75]. Those transitions can be driven by photons of frequency ν. For EPR experiments these frequencies are in the microwave range (in this work mostly X-band regime: approximately 8-12 GHz). Transitions are resonantly excited if one of the following resonance conditions is fulfilled:

$$\begin{aligned} T_+ \leftrightarrow T_0: &\quad h\nu = E_+ - E_0 = D + \mu_B g B \\ T_0 \leftrightarrow T_-: &\quad h\nu = E_0 - E_- = -D + \mu_B g B \end{aligned} \tag{3.8}$$

In order to detect resonance, one can either use a fixed magnetic field and sweep the microwave frequency or use a fixed microwave frequency and sweep the magnetic field. For the experiments in this thesis, the latter was implemented. In the simplest

case, the magnitude of microwave absorption is monitored during an EPR experiment. The energy splitting of the three triplet sublevels, transitions between them and the resulting absorption line are illustrated in **Figure 3.2**.

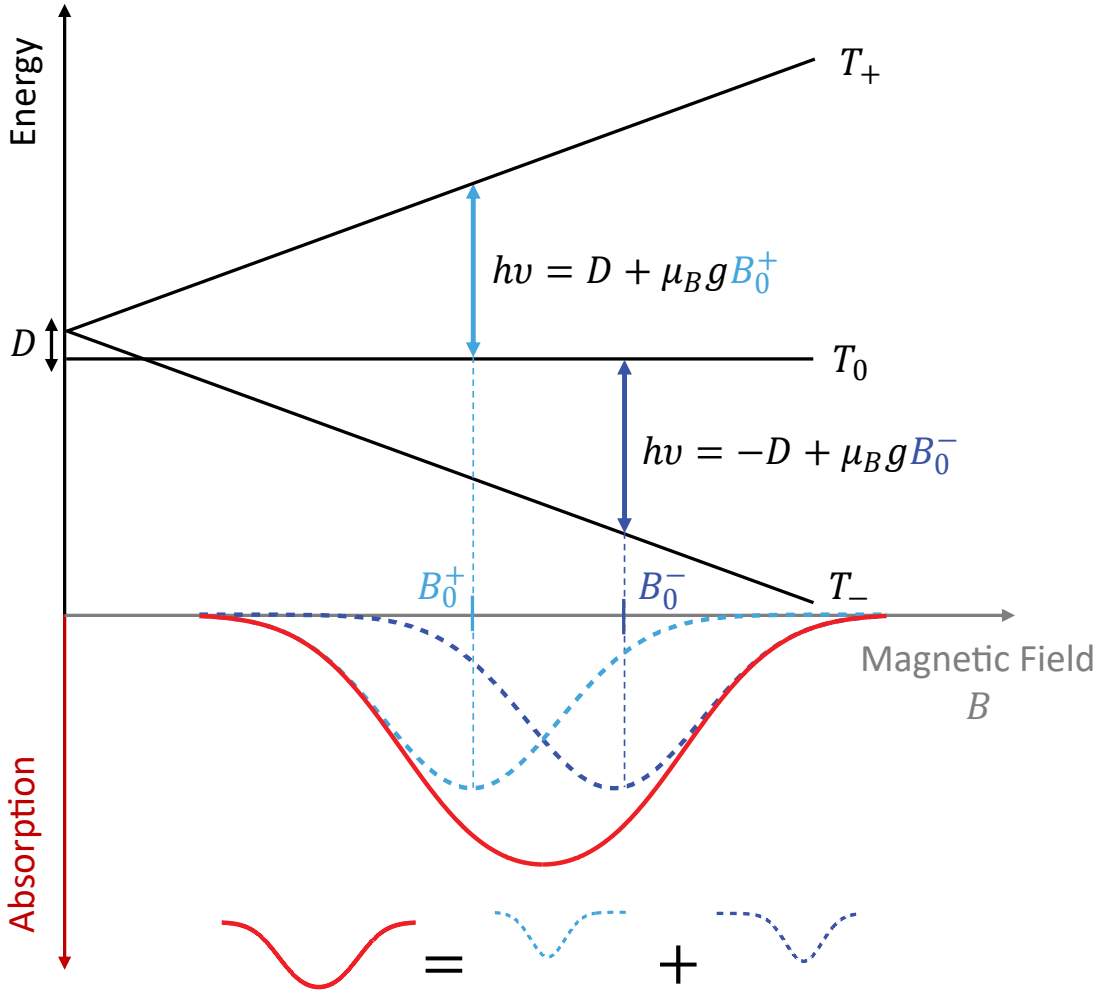

Figure 3.2: Connection between triplet energies in an external magnetic field and the shape of the EPR absorption line. Triplet sublevels T_+, T_0 and T_- are energetically split in an external magnetic field according to the Zeeman interaction. The zero-field splitting parameter D lifts the degeneracy of the sublevels at zero magnetic field. If microwaves of constant photon energy $h\nu$ are applied, there are two resonant transitions at the magnetic field positions B_0^+ and B_0^-. Both transitions have an individual absorption line (dotted lines in blue). The overall absorption spectrum (solid line in red) is a superposition of the two individual ones.

Because of the zero-field splitting D, there are two resonant positions B_0^+ and B_0^- for a constant microwave frequency (ν = const). Using **Equation 3.8**, one finds the two resonance positions at the following magnetic field values:

$$B_0^+ = \frac{h\nu - D}{\mu_B g}$$
$$B_0^- = \frac{h\nu + D}{\mu_B g} \tag{3.9}$$

A mean magnetic field $\overline{B}_0$ can be defined according to:

$$\overline{B}_0 = \frac{B_0^+ + B_0^-}{2} = \frac{h\nu}{\mu_B g} \tag{3.10}$$

Both of the two transitions have an individual absorption line. However, if they are sufficiently close, they overlap. An EPR experiment eventually yields the superposition of the two individual lines. Note, that this scenario is specific for sufficiently small values of D. If D exceeds a certain value, the individual lines are separately resolved instead of adding up to a single Gaussian line. For sufficiently large D values, so-called powder patterns are observed as EPR spectra [74, 76, 77]. However, powder patterns have not been found in the materials investigated in this work.

Absorption peaks in physics are never δ-functions but rather have a finite linewidth. The width of the overall absorption curve depends on a series of broadening mechanisms, the most important of which will be explained in the following.

Natural Linewidth

Every quantum mechanical transition has a natural linewidth that is due to the time–energy uncertainty. The natural lineshape is typically a Lorentzian curve whose width is proportional to the inverse lifetime of the involved states. This applies to the individual $T_+ \leftrightarrow T_0$ and $T_+ \leftrightarrow T_0$ absorption lines.

Zero-Field Interaction

As shown in **Figure 3.2**, the total absorption curve of a triplet system is the sum of the $T_+ \leftrightarrow T_0$ and the $T_0 \leftrightarrow T_-$ absorption line. This causes a broadening of the overall lineshape, which is of Gaussian type. Using **Equation 3.9**, one finds the distance ΔB between the two resonance positions B_0^+ and B_0^- on the magnetic field axis:

$$\Delta B = B_0^- - B_0^+ = \frac{2D}{\mu_B g} \tag{3.11}$$

Accordingly, ΔB and therefore the width of the total absorption line scale with D.

The proportionality $D \propto r^{-3}$, stated by **Equation 3.6**, is important in this context. The width of an EPR absorption line depends strongly on the spatial distance between two spins forming a triplet. An additional broadening mechanism can arise, if the

inter-spin distance of triplets in the investigated material is statistically distributed. The broader this distribution, the broader the detected EPR linewidth.

Hyperfine Interaction

Hyperfine interaction (HFI) describes the coupling between an electron spin and a nuclear spin. The effect of broadening due to HFI is similar to the broadening due to zero-field interaction [78, 74, 79]. HFI causes a splitting of the triplet energies into more sublevels. Accordingly, more individual transitions exist that eventually overlap to a total broadened line. In organic molecules that contain several heteroatoms (e.g. nitrogen), electron spins couple to a number of nuclear spins. Typically, discrete transition lines can not be resolved. In this case, the broadening due to HFI is also called unresolved hyperfine interaction.

g-factor

If the g-factors of two particles that form a triplet differ between each other, the EPR absorption line is broadened [80]. This can be illustrated in a simplified picture where the two spins with g-factors g_a and g_b are considered independent. In this case, only the Zeeman interaction needs to be considered in the EPR resonance conditions for the two spins:

$$\begin{aligned} h\nu &= g_\mathrm{a}\mu_B B_\mathrm{a} \\ h\nu &= g_\mathrm{b}\mu_B B_\mathrm{b} \end{aligned} \tag{3.12}$$

Here, B_a and B_b are the resonance positions for spin a and b. Both spins have their own individual absorption line. The difference ΔB between the two resonant magnetic fields is given by:

$$\Delta B = B_\mathrm{a} - B_\mathrm{b} = \left(\frac{1}{g_a} - \frac{1}{g_b}\right)\frac{h\nu}{\mu_B} \tag{3.13}$$

Consequently, if $\Delta g = g_\mathrm{a} - g_\mathrm{b} \neq 0$ then $\Delta B \neq 0$. The two individual absorption lines for spin a and b superimpose to a single broadened line with a width proportional to ΔB. Moreover, **Equation 3.13** implies that line broadening due to Δg depends linearly on the applied microwave frequency ν. A broadening of the absorption line with increasing frequency is therefore expected.

3.4 Half-Field Transition

In previous sections, only transitions that follow the spin-selection rule $\Delta m_s = 1$ have been described. However, it is observed that transitions with $\Delta m_s = 2$ can occur as well, although with lower intensity [81, 82]. For triplets, this corresponds to transitions between T_+ and T_-. Using the energies for T_+ and T_- from **Equation 3.7**, one finds the following EPR resonance condition:

$$T_+ \leftrightarrow T_- : \quad h\nu = E_+ - E_- = 2\mu_B g B_{\mathrm{hf}}, \tag{3.14}$$

with the resonant magnetic field being:

$$B_{\mathrm{hf}} = \frac{h\nu}{2\mu_B g} \tag{3.15}$$

Comparison of B_{hf} and the mean field $\overline{B}_0$ from **Equation 3.10** in the previous section shows that $B_{\mathrm{hf}} = \frac{1}{2}\overline{B}_0$. Transitions with $\Delta m_s = 1$ are therefore called *full-field* transitions and those with $\Delta m_s = 2$ *half-field* transitions. A graphical summary of full-field and half-field transitions is given in **Figure 3.3a**.

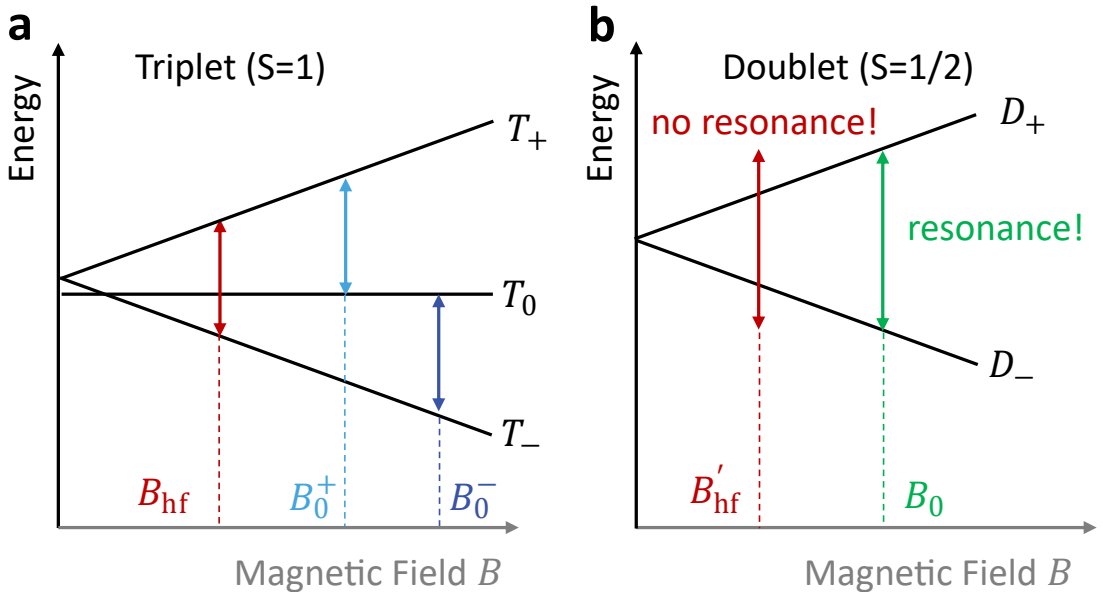

Figure 3.3: Illustration of half-field transitions. **a**, Energy diagram of triplet sublevels in an external magnetic field with a finite zero-field splitting. There are three resonant magnetic field values for a constant microwave frequency. There are the two full-field transitions (between T_+ and T_0 at B_0^+ and between T_0 and T_- at B_0^-), but also a half-field transition (between T_+ and T_-) at B_{hf}. **b**, EPR transition in doublets are between D_+ and D_- at B_0. There is no resonance at $B'_{\mathrm{hf}} = \frac{1}{2}B_0$.

The relative intensity I_{rel}, defined as the ratio between the half-field transition's intensity and the full-field transition's intensity, is given by [82]:

$$I_{\mathrm{rel}} = \frac{A}{r_{\mathrm{ab}}^6}\left(\frac{9.1}{\nu}\right)^2 \tag{3.16}$$

Here, A is a prefactor, r_{ab} the distance between the two spins forming a triplet and ν the applied microwave frequency. This equation implies that the intensity of half-field transitions for triplet species with large inter-spin distances practically vanishes. The observation of a half-field signal is therefore an indication that the investigated spin system consists of two nearby spins.

Furthermore, the occurrence of a half-field signal unambiguously excludes doublets (spin 1/2 systems) as the origin of an observed EPR signal. This is illustrated in **Figure 3.3b**. EPR transitions of doublets occur between the $m_s = +1/2$ state (D_+) and the $m_s = -1/2$ state (D_-). The corresponding resonance position B_0 for a fixed microwave frequency ν is given by:

$$B_0 = \frac{h\nu}{\mu_B g} \tag{3.17}$$

At half-field $B_{\mathrm{hf}}^{'} = \frac{1}{2}B_0$ the energy of microwave photons does not match any energy level difference within the spin system and no microwave absorption is observed.

In summary, if an unknown spin species is probed in an EPR experiment, the observation of a half-field signal yields the following information:

(i) The signal stems from a species with small inter-spin distance

(ii) The signal does not stem from a doublet

3.5 Spin Polarization

Net absorption between triplet states in an EPR experiment is only possible if the populations P_i of the triplet states T_i are non-equally distributed, in other words, if the system is spin-polarized. Naturally, this is always given in systems at non-zero temperature ($T \neq 0$) according to Boltzmann statistics that yields the following population probability p_i of a state with energy E_i:

$$p_i = \frac{1}{Z}\exp\left(\frac{-E_i}{k_{\mathrm{B}}T}\right), \quad \text{with} \quad Z = \sum_i \exp\left(\frac{-E_i}{k_{\mathrm{B}}T}\right) \tag{3.18}$$

Here, Z is the canonical partition function. For a three-level system consisting of the three triplet states T_+, T_0 and T_-, Z is given by:

$$Z = \exp\left(\frac{-E_+}{k_B T}\right) + \exp\left(\frac{-E_0}{k_B T}\right) + \exp\left(\frac{-E_-}{k_B T}\right) \tag{3.19}$$

Using the triplet energies according to **Equation 3.7** with an EPR typical magnetic field of $B = 335$ mT, one finds the following population probabilities p_i at room temperature ($T = 300$ K):

$$p_+ = 0.332833$$
$$p_0 = 0.333333$$
$$p_- = 0.333834$$

According to those numbers, the relative population difference between the T_+ and the T_0 state, as well as between the T_0 and the T_- state is approximately 0.15%. If the triplet populations are solely determined by Boltzmann statistics, EPR signals larger than 0.15% are not expected. This upper limit can be altered if additional selective population or depopulation mechanisms exist in the probed system.

3.6 Detection Schemes

The simplest detection method in EPR is to probe microwave absorption, which is employed in classical EPR. There are, however, limitations to this method that need to be considered when using EPR for the investigation of TADF emitters. First, the minimum number of spins that is required for spins to be detectable via EPR is around $\sim 10^9$ [83]. The number of spins in TADF emitter films might, however, be below this lower limit. Second, in order for triplets to be probed they need to first be optically or electrically excited. Those excitations might generate additional spin species, such as radicals, that are not related to light generation in TADF systems. These additional spin species increase the complexity of EPR spectra and complicate their interpretation. Advanced EPR methods are therefore desired which exhibit high spin sensitivity as well as spin selectivity. Detection methods that meet these requirements will be introduced in the following.

Optically Detected Magnetic Resonance

Optically detected magnetic resonance (ODMR) is based on the detection of a sample's luminescence change under magnetic resonance conditions [84, 85, 86]. There are two implementations of ODMR that are used in this work. The first is photoluminescence detected magnetic resonance (PLDMR) where a thin film of the investigated material is optically excited and the change of PL under magnetic resonance conditions is probed. The second is electroluminescence detected magnetic resonance (EL-

DMR) where a fully processed device is electrically driven and the change of EL from the device under magnetic resonance conditions is probed.

The genesis of ODMR signals from TADF emitters is based on the following consideration. If a TADF-based OLED is driven by a constant current or a thin TADF emitter film is optically excited with constant power, the system is in an equilibrium state. Here, the population densities of the singlet excited state $[S_1]$, the triplet excited state $[T_1]$ and the singlet ground state $[S_0]$ are constant. They are mostly determined by the radiative decay rate of the singlet excited state k_F, the RISC rate k_{RISC}, the ISC rate k_{ISC}, the non-radiative decay rate of the triplet excited state k_{NR} and the respective generation rates for electrical injection or optical excitation (see **Figure 3.4a**). The fluorescence intensity I is given by the product of k_F and the population density $[S_1]$: $I = k_F[S_1]$.

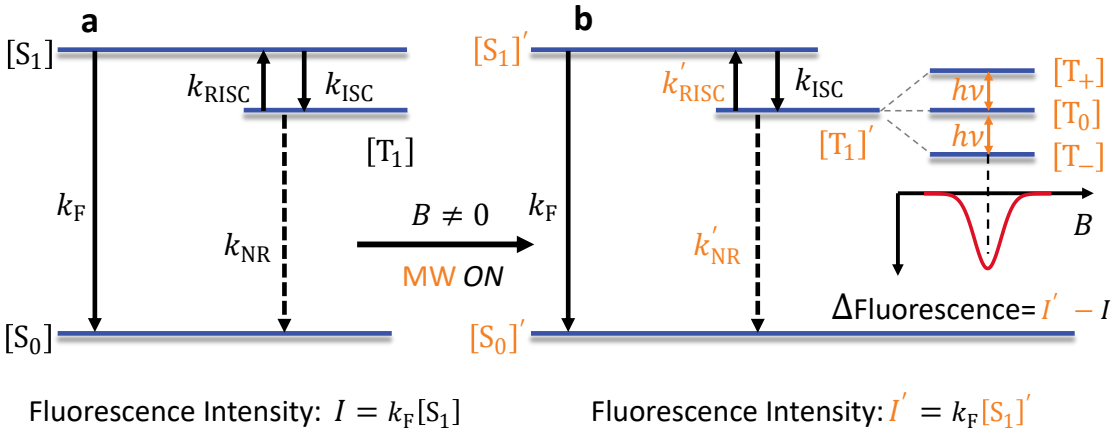

Figure 3.4: Illustration of the ODMR signal genesis. **a**, Jablonski diagram of a TADF emitter including the population densities $[S_1]$, $[S_0]$ and $[T_1]$ for singlet excited and ground state and the triplet excited state. An equilibrium state is determined by the radiative decay rate of the singlet excited state k_F, the RISC rate k_{RISC}, the ISC rate k_{ISC}, the non-radiative decay rate of the triplet excited state k_{NR} and the respective generation rates for electrical injection or optical excitation. The fluorescence intensity I is given by $I = k_F[S_1]$. **b**, The application of an external magnetic field and resonant microwaves changes the RISC rate and the non-radiative transition rate of the triplet state. An altered fluorescence intensity is now given by: $I' = k_F[S_1]'$. An ODMR experiment probes the microwave induced change of fluorescence which is given as $I' - I$.

When an external magnetic field and resonant microwaves are applied to the system, the equilibrium state is perturbed (see **Figure 3.4b**). Resonant microwaves drive transitions between the triplet sublevels which essentially changes the RISC rate from k_{RISC} to k'_{RISC} and the non-radiative decay rate of the triplet excited state from k_{NR} to k'_{NR}. Consequently, the population densities are altered to $[T_1]'$ and $[S_1]'$. Now, the altered fluorescence intensity I' is given by: $I' = k_F[S_1]'$.

There are two important scenarios that explain why k_{RISC} and k_{NR} can be altered under magnetic resonance conditions. First, there can be individual rates k^{+}_{RISC}, k^{0}_{RISC} and k^{-}_{RISC} or k^{+}_{NR}, k^{0}_{NR} and k^{-}_{NR} for the three triplet sublevels T_+, T_0 and T_-. Then transitions between those sublevels can change the overall rates k_{RISC} and k_{NR}. A second scenario for a change of k_{RISC} and k_{NR} is based on sample heating. The absorption of microwave photons under magnetic resonance conditions equals an addition of energy to the investigated system. This leads to sample heating. k_{RISC} and k_{NR} are temperature-dependent, thus an increase of the sample temperature changes those rates.

In PLDMR, a thin film, consisting of the investigated TADF emitter, is optically excited and the PL change ΔPL under magnetic resonance conditions compared to the PL off-resonance is monitored:

$$\frac{\Delta \mathrm{PL}}{\mathrm{PL}} = \frac{\mathrm{PL}_{\text{MW-on}} - \mathrm{PL}_{\text{MW-off}}}{\mathrm{PL}_{\text{MW-off}}} \tag{3.20}$$

In ELDMR, a fully processed OLED is driven electrically and the EL change ΔEL under magnetic resonance conditions compared to EL off-resonance is monitored:

$$\frac{\Delta \mathrm{EL}}{\mathrm{EL}} = \frac{\mathrm{EL}_{\text{MW-on}} - \mathrm{EL}_{\text{MW-off}}}{\mathrm{EL}_{\text{MW-off}}} \tag{3.21}$$

The quantities ΔPL/PL and ΔEL/EL are referred to as *PLDMR* and *ELDMR contrast*. Within the terminology of **Figure 3.4**, **Equations 3.20** and **3.21** can be written as:

$$\frac{\Delta \mathrm{PL}}{\mathrm{PL}} = \frac{I' - I}{I} \tag{3.22}$$

$$\frac{\Delta \mathrm{EL}}{\mathrm{EL}} = \frac{I' - I}{I} \tag{3.23}$$

Overall, the advantage of ELDMR and PLDMR is that both methods probe only spin states that are involved in the light generation mechanisms as EL and PL are detected. Other spin species, such as radicals, might absorb microwave photons in resonance, however, those absorption processes don't impact light generation. ODMR methods are therefore ideal techniques to investigate spin states of TADF emitters.

Electrically Detected Magnetic Resonance

The purpose of OLEDs is the generation of light from electrical injection of charge carriers. As discussed previously, the influence of spin states on the light generation itself can ideally be investigated by ODMR. The injection and transport of charge carriers, however, play an important role as well. Furthermore, transport layers of OLEDs might not be luminescent and therefore not suitable to be investigated by ODMR.

An EPR-based method that addresses injection and transport in OLEDs is electrically detected magnetic resonance (EDMR) [87]. It probes the current change ΔI through the device under magnetic resonance conditions compared to the current I off-resonance:

$$\frac{\Delta I}{I} = \frac{I_{\text{MW-on}} - I_{\text{MW-off}}}{I_{\text{MW-off}}} \tag{3.24}$$

There are several scenarios for the genesis of EDMR signals. The first is related to hopping transport in organic semiconductors and illustrated in **Figure 3.5a**.

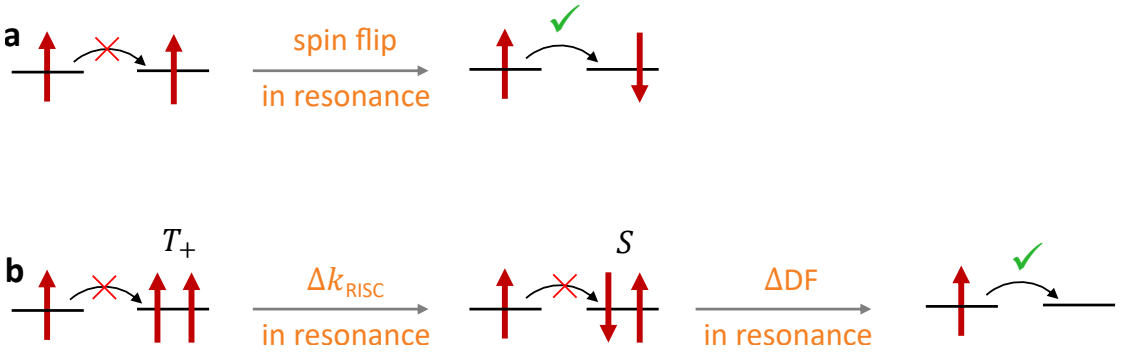

Figure 3.5: Illustration of EDMR signal genesis: **a**, Hopping between neighboring sites is blocked because of Pauli's exclusion principle. A microwave-induced spin flip lifts the blocking. **b**, Hopping of a charge carrier onto a site that is occupied by a triplet exciton is blocked. Microwave-induced enhancement of RISC to a singlet and subsequent delayed fluorescence clear the site for hopping.

Hopping transport is modeled as a jumping of charge carriers between sites. If two charge carriers of equal spin orientation occupy neighboring sites, a hopping event from one site to the other is forbidden according to Pauli's exclusion principle. Under magnetic resonance conditions, however, spin flips are induced that can change the configuration to two sites with opposite spin orientation. The hopping event becomes spin-allowed, which increases the current flow. This increase is detected as an EDMR signal.

A second origin for EDMR signals is spin-dependent recombination, as illustrated for TADF emitters in **Figure 3.5b**. Assume two neighboring molecules, one of which is occupied by a charge carrier and the other one by a triplet exciton. Hopping between these two molecules is not possible. As explained in the context of ODMR, the RISC rate can increase under magnetic resonance conditions. In this case, the probability of the triplet to be converted to a singlet increases. A singlet, on the other hand, can decay radiatively as delayed fluorescence. After the decay, the molecule that was previously occupied by the singlet is now available for hopping. The increased hopping and current flow result in an EDMR signal.

4 Experimental Section

The previous chapter introduced the theoretical basics of the EPR-based methods PLDMR, ELDMR and EDMR. This chapter provides an overview of the technical realization for these methods. That includes the sample types for each method.

In order to perform an EPR experiment, a setup roughly needs to provide the following four basic elements:

(i) creation of an external **magnetic field**

(ii) application of **microwaves** to the sample

(iii) **excitation** of spins in the sample

(iv) **detection** of magnetic resonance

If temperature-dependent measurements are desired, additional features allowing control of the sample temperature are needed. The details of each method's setup and the implementation of the four fundamental elements will be explained in the following.

4.1 PLDMR

PLDMR probes the PL intensity change ΔPL from an optically excited sample under magnetic resonance conditions. The setup used for this technique is based on the modified Bruker Spectrometer *Bruker ESP300*. The four basic elements of the setup are realized in the following way:

(i) **magnetic field**: electromagnet

(ii) **microwaves**: microwave cavity

(iii) **excitation**: UV LED

(iv) **detection**: ΔPL via a photodetector

A full overview of the setup used for PLDMR is illustrated in Figure **4.1**.

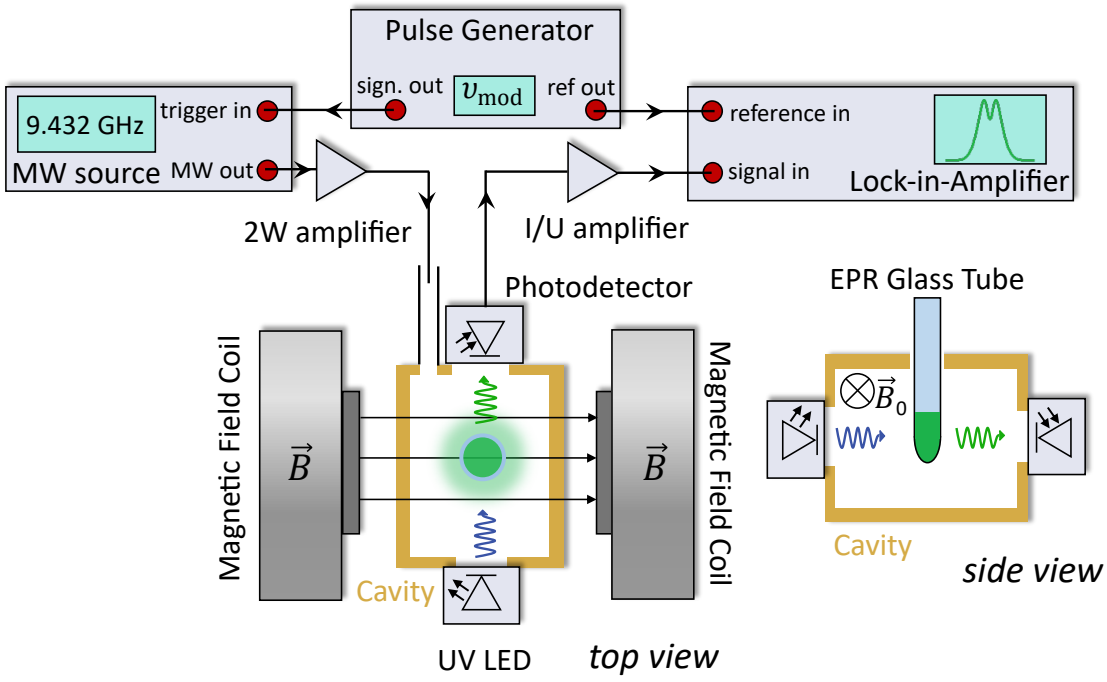

Figure 4.1: Illustration of the PLDMR setup. ***Top view***: Two parallel magnetic field coils create an external magnetic field, with the field lines pointing from one coil to the other. Microwaves are created in a microwave source and are led to a cavity. The sample is placed in the middle of the cavity. A UV LED optically excites the sample, while its PL is detected via a silicon photodetector. A pulse generator is used to modulate the microwaves between on and off, enabling lock-in detection. ***Side view***: The cavity has a hole at its top for the insertion of an EPR tube.

Magnetic Field

The external magnetic field is created via an electromagnet. It consists of a pair of copper coils, through which an electric current is flowing. The current creates a magnetic field, with the field lines pointing from one coil to the other. During a magnetic field sweep the current through the coils and therefore the absolute value of the magnetic field are increased.

Microwaves

A cavity is placed in between the two magnetic field coils. The cavity is a rectangular resonator with dimensions in the range of the microwaves' wavelength. The used cavity (*ER4104OR*) has a resonance frequency of $\nu_0 = 9.432$ GHz, which corresponds to a wavelength of around $\lambda = 3$ cm. If microwaves of frequency ν_0 are led to the cavity from a microwave source (*Anritsu MG3694C*), a standing wave is formed in the cavity. Microwaves from the source pass through an amplifier (*Microsemi APA0612-30-33*) before being led to the cavity, which allows microwave powers of up to 2W.

Samples for PLDMR are prepared in quartz glass tubes with an inner diameter of around 2.8 mm. The cavity has a hole on top, which is just large enough for such glass tubes to be inserted into the cavity, as illustrated in **Figure 4.1** ***side view***. The investigated material is given by a film at the edge of the inner glass at the bottom of the tube. During sample preparation the material of interest is first dissolved in chlorobenzene, and then poured into the glass tube. Subsequent evacuation of the tube leads to annealing of the solvent and the formation of a film on the edge of the tube.

Excitation

The cavity is equipped with two optical accesses, allowing optical excitation of a sample as well as detection of luminescence from the sample. For PLDMR measurements, a UV LED driven by a constant current is used as an excitation source. It emits in continuous wave mode at around 365 nm, which overlaps with the absorption spectra of most of the organic compounds used in this work.

Detection

A silicon photodiode is placed at the opposite optical access of the cavity to detect the PL of the sample. Microwave induced PL changes are, however, typically too small to be distinguishable from noise with the photodiode itself. Therefore, a lockin-in amplifier (*Signal Recovery Model 7265*) as well as a current to voltage (I/U) amplifier (*Femto DLPCA*) are used. Lock-in detection is based on the extraction of signal contributions with a particular reference frequency. During PLDMR measurements, the microwave source output is modulated with a frequency ν_{mod}. A pulse generator (*Keithley3390*) creates a TTL pulse with frequency ν_{mod}, which is led to the microwave source, causing the microwave signal to switch between on and off with the frequency ν_{mod}. Consequently, PL from the sample oscillates between $\mathrm{PL}_{\mathrm{MW\text{-}off}}$ and $\mathrm{PL}_{\mathrm{MW\text{-}off}} + \Delta\mathrm{PL}$ with the frequency ν_{mod}. This oscillating PL signal is measured with the photodiode producing a current signal that is transformed into a voltage by the I/U amplifier. This voltage signal is finally measured by the lock-in amplifier. The lock-in amplifier uses a reference signal from the pulse generator, which is modulated with ν_{mod} as well. Finally, only contributions in the PL signal that oscillate with ν_{mod} are recovered yielding ΔPL.

For temperature control, PLDMR samples are put into a helium-flow cryostat (*Oxford Instruments ESR900*) inside the cavity. The interplay between helium flow and a heater that is regulated by a temperature controller (*Lakeshore 330*) allows to realize temperatures between room temperature and around 4 K.

4.2 ELDMR

For ELDMR the four basic elements of the setup are realized in the following way:

(i) **magnetic field**: electromagnet

(ii) **microwaves**: microwave transmission line

(iii) **excitation**: electrical injection of charge carriers via an external voltage

(iv) **detection**: ΔEL via a photodetector

Magnetic Field

The external magnetic field is created with a current through copper coils, analogue to the PLDMR setup.

Microwaves

The ELDMR setup relies on the application of microwaves via a so-called *microwave transmission line* or in short *stripline*. An illustration of such a device is shown in **Figure 4.2**.

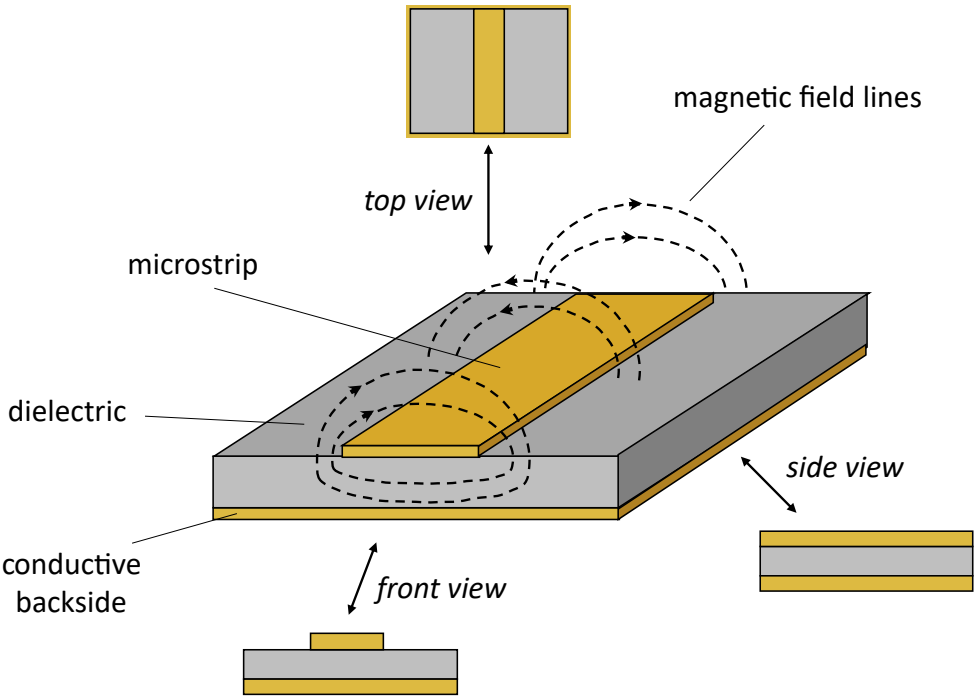

Figure 4.2: Illustration of a microwave transmission line (stripline). It consists of a microstrip on top of a dielectric with a conductive backside. Analogue to a coaxial cable, an electromagnetic wave can propagate through the dielectric with the magnetic field lines around the microstrip. *Top*, *front* and *side view* of the stripline are illustrated. These illustrations are used in further figures in this section.

It includes illustrations of the *top*, *front* and *side view* of the stripline, which will be used in other figures in this section. A stripline consists of a metallic microstrip, which is placed on a dielectric with a conductive backside [88]. Similar to a coaxial cable, an electromagnetic wave can propagate through the dielectric medium between microstrip and backside. In contrast to a coaxial cable, the field lines of the magnetic field are not restricted to inside the dielectric but exist above the microstrip as well. Therefore, if an OLED is placed on top of the microstrip, microwaves can be applied. The usage of a stripline instead of a microwave cavity offers two advantages. First, the stripline is not limited to a unique resonance frequency. Multifrequency experiments within a single setup are therefore possible allowing the investigation of frequency dependent effects (for instance the broadening of EPR spectra related to the g-factor, as explained in **Chapter 3**, **Section 3.3**). Second, if a cavity is used, the architecture of OLED samples needs to be adapted for the devices to fit into an EPR tube. This puts a limit on the seize of the investigated OLEDs, which is challenging for sample preparation. As a result, potential issues regarding the reproducibility of experiments might occur. A sample design that offers more flexibility in terms of the sample's dimensions is therefore beneficial. The OLED sample layout used for ELDMR experiments is shown in **Figure 4.3**.

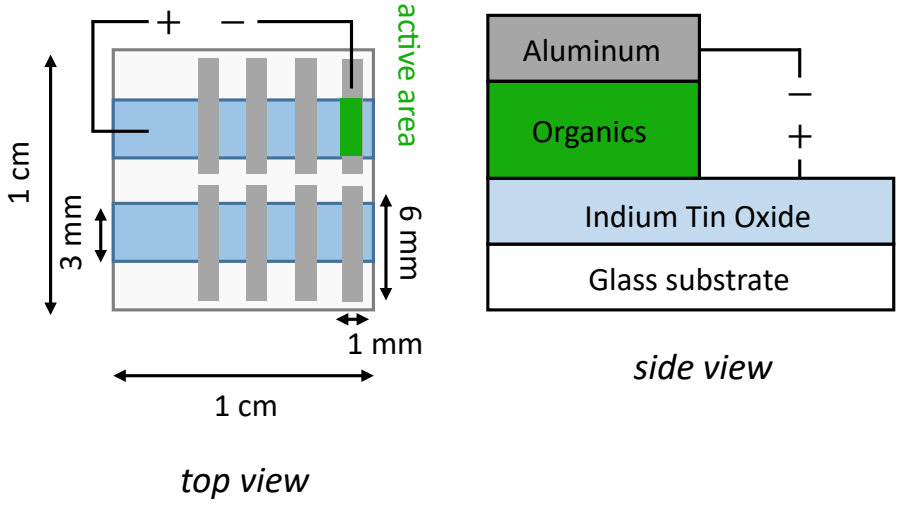

Figure 4.3: ***Top view***: Illustration of the OLED sample layout including the dimensions. Each sample consists of a glass substrate with two ITO stripes on top. There are four layers of organics and aluminum on each ITO stripe yielding a total of 8 OLED stacks per substrate. ***Side view***: Layer stack for each OLED. A glass substrate is covered with ITO followed by the organic layer and an aluminum layer.

OLED samples consist of 1 cm^2 glass substrates with two 3 mm wide stripes of Indium Tin Oxide (ITO) on top. ITO is both transparent and electrically conductive, which enables contacting of the OLED while it also allows light outcoupling. On top of the ITO stripes are organic layers as well as an aluminum layer as a cathode. There are 4 layers of organics and aluminum on each ITO stripe yielding a total of 8 OLED stacks per substrate. The active area (3 mm^2) for each stack is given by the overlap between ITO and the organic layers. The specific composition of the organic layers in this thesis will be presented in the respective results chapters for each experiment. The electrical contacting scheme for the used OLED design and the application of microwaves with a stripline are illustrated in **Figure 4.4**.

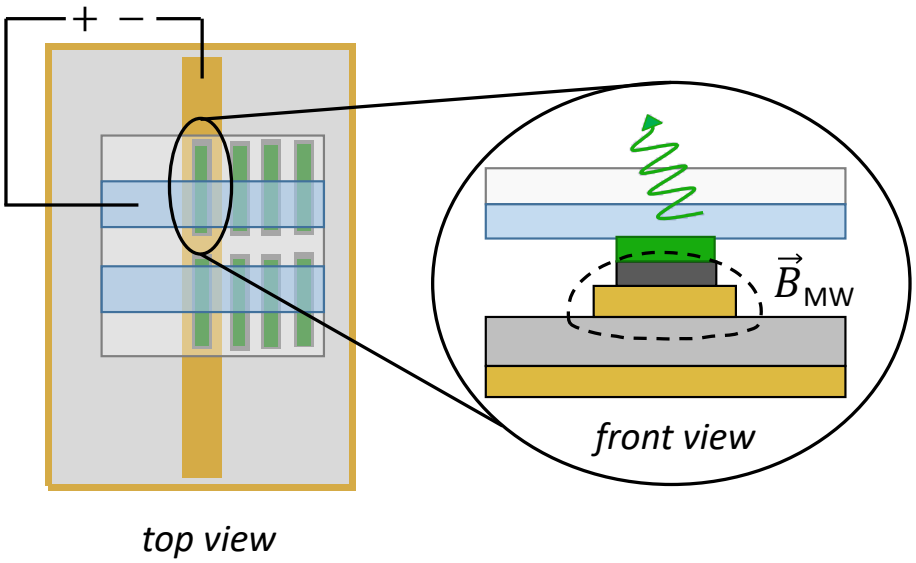

Figure 4.4: Contacting scheme of OLEDs on a stripline. ***Top view***: An OLED is placed on the stripline upside down, such that the aluminum cathode is in contact with the stripline's microstrip. ***Front view***: When the aluminum cathode is in contact with the stripline, the distance between the microstrip and the organic layers is reduced to a minimum. The magnetic field lines couple efficiently to spins in the organic layers.

The glass substrate is turned upside down and placed on top of the stripline, such that the aluminum cathode is in contact with the microstrip. If a voltage is applied between the ITO stripe and the microstrip, a current can flow and the OLED is emitting light. The advantage of this contacting scheme is the proximity of the OLED and the microstrip. The magnitude of the microwaves' magnetic field decreases with increasing distance from the microstrip. If microwaves are transmitted via the stripline, the magnetic field lines penetrate the OLED and couple to spins in the organic layers efficiently, as illustrated in **Figure 4.4** ***front view***.

The implementation of the stripline within the entire setup is shown in Figure **4.5**.

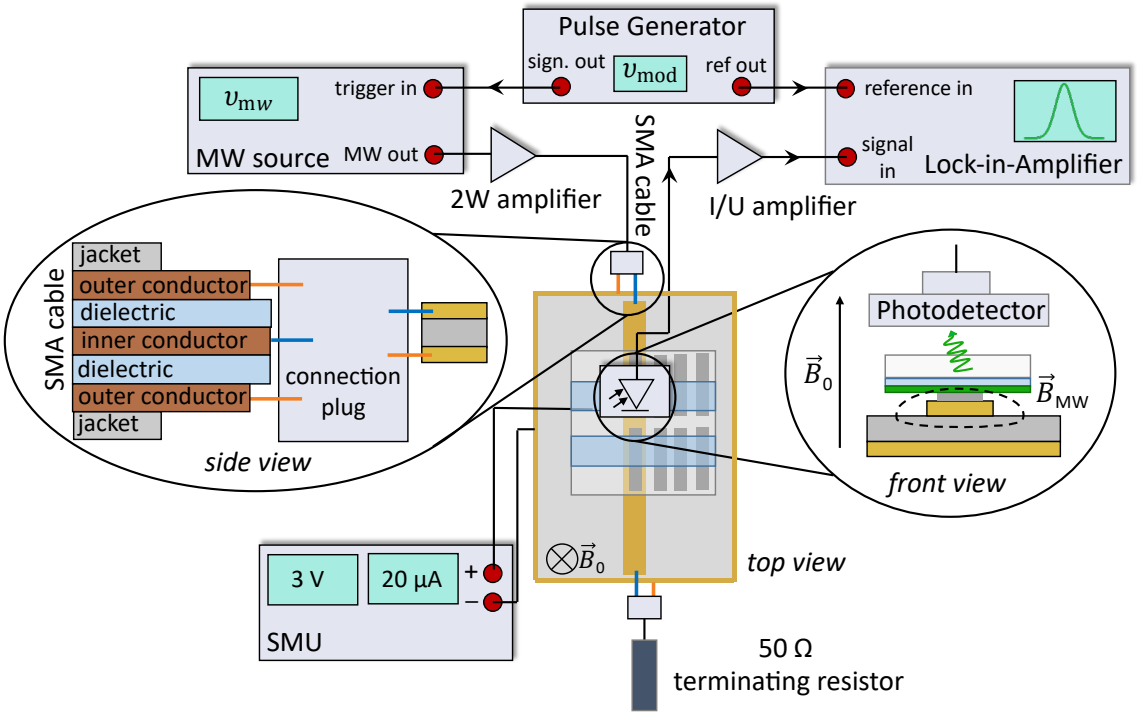

Figure 4.5: Illustration of the ELDMR setup. ***Top view***: A sample is placed on the stripline upside down (in contact with the microstrip) and driven electrically via an SMU. The plus pole is connected to the ITO stripe and the minus pole to the backside of the stripline. The backside of the stripline is electrically connected to the microstrip via a 50 Ω terminating resistor. Microwaves are created via a microwave source and led to the stripline via an SMA cable which can be plugged to the stripline via a connection plug. ***Side view***: The connection plug electrically connects the outer conductor of the SMA cable with the stripline's backside and the inner conductor with the microstrip. ***Front view***: A photodetector is placed on top of the stripline collecting the OLED's EL. As for PLDMR, microwaves are modulated via a pulse generator to enable lock-in detection.

Microwaves from a source (*Anritsu MG3694C*) pass a 2 W amplifier and are led to the stripline. Microwaves from the source are conducted via an SMA (SubMiniature version A) cable, which is a special type of coaxial cable optimized for the GHz frequency range. The SMA cable couples to the stripline via a connection plug. It connects the inner conductor of the SMA cable with the microstrip and the outer conductor with the backside (see **Figure 4.5** ***side view***). The other side of the stripline is equipped with another connection plug. It enables the connection of the stripline to a 50 Ω terminating resistor which closes the electrical circuit with matching impedance.

Excitation

A source–measure unit (SMU) *Keithley 237* is used to provide an external voltage. The plus pole is connected to the OLED's ITO stripe and the minus pole is connected to the stripline's backside. Because the 50 Ω terminating resistor electrically connects microstrip and backside, the minus pole is essentially connected to the microstrip. Finally, the microstrip is in contact with the OLED's aluminum cathode, as shown in **Figure 4.4**.

Detection

EL from the OLED is detected via a photodetector that is placed on top of the OLED's glass substrate, as shown in **Figure 4.5** ***front view***. The same lock-in detection scheme as for PLDMR is used. A pulse generator triggers the microwave source with a TTL pulse of frequency ν_{mod}, while sending a reference signal of the same frequency to a lock-in amplifier (*Signal Recovery Model 7265*). The OLED's EL generates a photocurrent in the photodetector, which is amplified by the I/U amplifier (*Femto DLPCA*) and transformed to a voltage. This voltage is detected by the lock-in amplifier, which recovers the microwave induced change ΔEL.

For temperature control, the stripline is placed inside a nitrogen flow cryostat. The interplay between nitrogen flow and a heater that is regulated with a temperature controller (*Lakeshore 335*) allows the realization of temperatures between room temperature and around 77 K.

Side note: The magnetic field coils are not visible in **Figure 4.5** because of the *top view* perspective. The magnetic field lines are perpendicular to the shown plane. The two coils can be imagined to be placed on top and below of what is shown in **Figure 4.5**.

4.3 EDMR

For EDMR, the four basic elements of the setup are realized in the following way:

(i) **magnetic field**: electromagnet

(ii) **microwaves**: microwave transmission line

(iii) **excitation**: electrical injection of charge carriers via an external voltage

(iv) **detection**: ΔI via a current to voltage amplifier

The setup used for EDMR is shown in **Figure 4.6**.

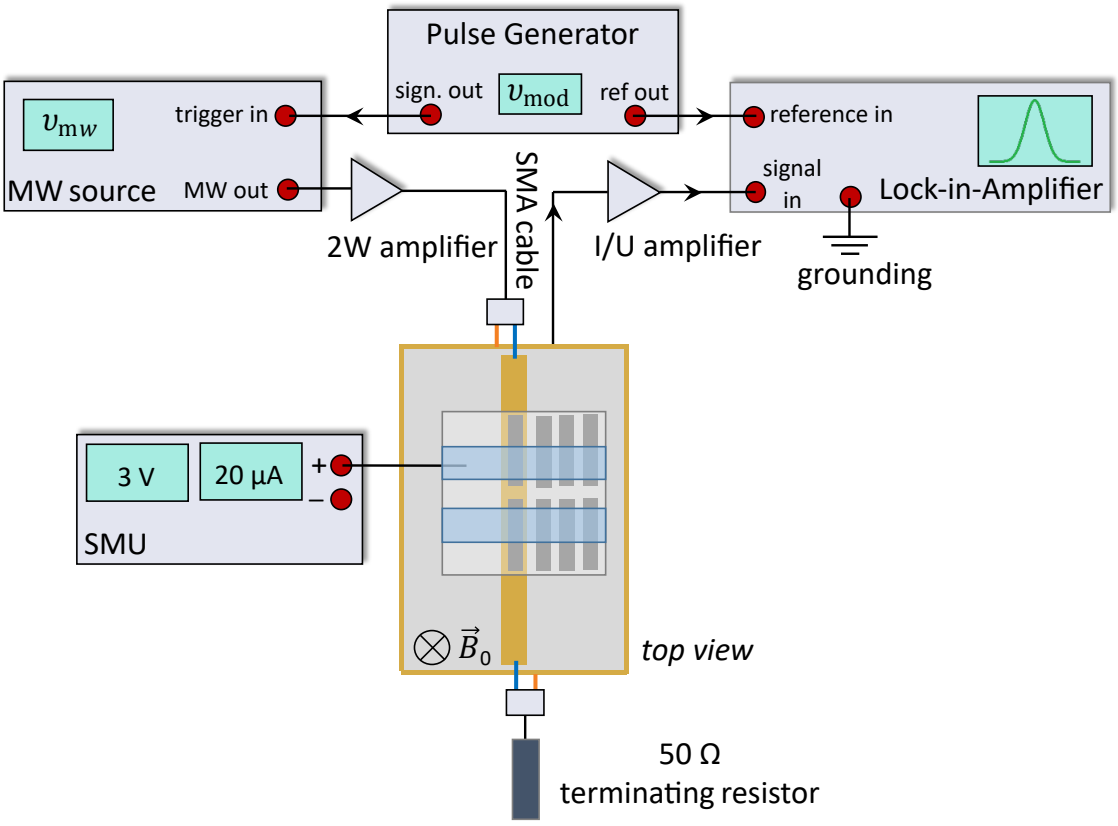

Figure 4.6: Illustration of the EDMR setup. ***Top view***: Analogue to the ELDMR setup, an OLED is placed on the stripline upside down. The current path, that is responsible for OLED operation, is between the plus pole of an SMU and the grounding of the lock-in amplifier. This contacting scheme allows direct detection of the microwave induced current change in the OLED.

Magnetic Field

The external magnetic field is created with a current through copper coils, analogue to the PLDMR and ELDMR setups.

Microwaves

The EDMR setup relies on microwave application via the stripline, as explained for ELDMR. Sample design, the microwave source, the microwave amplifier and the electric circuit for microwave conduction are identical to the ELDMR setup.

Excitation and Detection

In EDMR experiments, an OLED is electrically driven, while the current change ΔI under magnetic resonance conditions is probed. For this excitation and detection scheme, a special electric circuit is used. For the application of an external voltage to

the OLED, the same source–measure unit (SMU) as for ELDMR is used. The plus pole is connected to the OLED's ITO stripe. The minus pole, however, is not connected at all and remains unused. Instead the backside of the stripline is directly connected to the I/U amplifier, which in turn is connected to the lock-in amplifier. With this structure, current flows between the SMU's plus pole and the grounding of the lock-in amplifier. In this case, the lock-in amplifier measures both the total current through the OLED as well as the microwave induced current change ΔI. Again, a modulation scheme using a pulse generator to enable lock-in detection is used.

Temperature control is analogue to ELDMR.

4.4 External Quantum Efficiency

The main focus of this thesis are EPR experiments on TADF OLEDs. It is, however, essential to perform basic OLED characterization measurements as well, in order to ensure proper interpretation of EPR data. One of the most import characteristics of an OLED is its external quantum efficiency (EQE) as introduced in **Chapter 2**, **Section 2.6**. The EQE is defined as:

$$\mathrm{EQE} = \frac{n_{\mathrm{Ph}}}{n_{\mathrm{inj}}}, \tag{4.1}$$

with n_{Ph} being the number of emitted photons and n_{inj} the number of injected charge carriers. This equation can as well be expressed in terms of the number of photons emitted per time ϕ_{Ph} and the current through the OLED I_{OLED}:

$$\mathrm{EQE} = \frac{e\phi_{\mathrm{Ph}}}{I_{\mathrm{OLED}}}, \tag{4.2}$$

with e being the elementary charge. In order to experimentally determine an OLED's EQE, one needs to measure ϕ_{Ph} and I_{OLED}. Measuring the current through the OLED is rather trivial, as it is typically detected by the device, that provides the external voltage for OLED operation. A more challenging task is to measure all photons emitted from the OLED. The most accurate method to determine ϕ_{Ph} is to use an integrating sphere, which is covered with a reflective coating at its interior (also called *Ulbricht* sphere). An OLED can be placed at the entrance of the sphere and all emitted light is reflected on to a photodetector. In this thesis, however, a workaround solution was used that doesn't require an integrating sphere. This approach is easier to realize, while maintaining reasonable accuracy. The setup is illustrated in **Figure 4.7**.

An OLED is operated via a Semiconductor Parameter Analyzer (*Agilent 4155C*), which measures the current through the OLED I_{OLED} during operation.

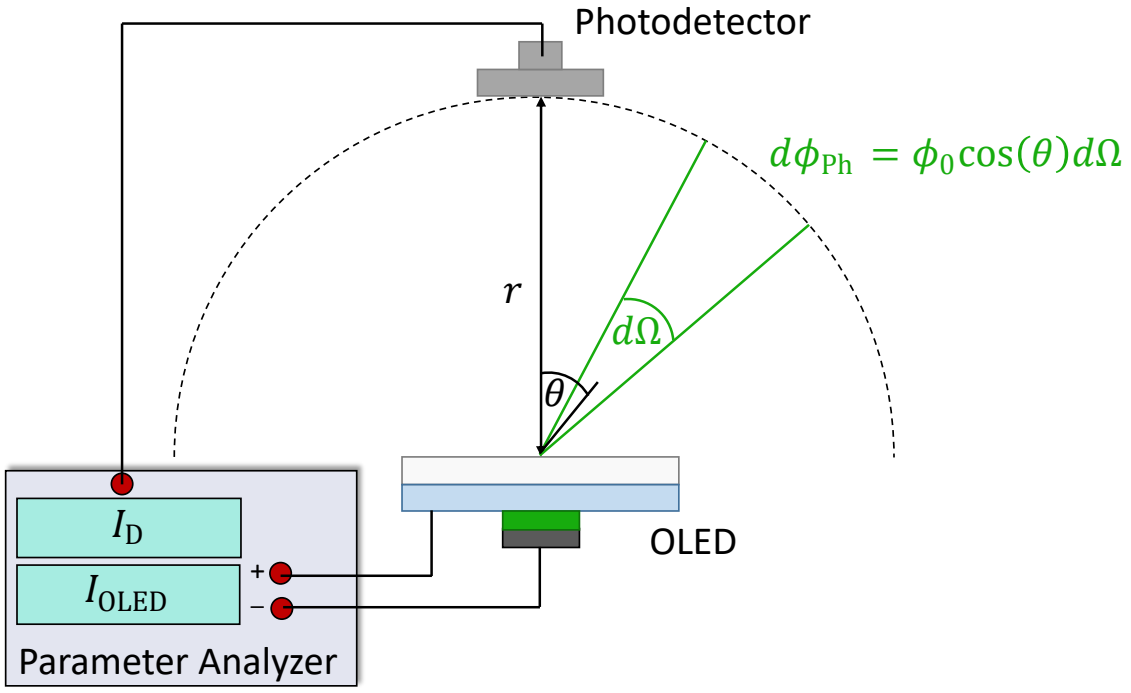

Figure 4.7: Illustration of the EQE setup: An OLED is driven with a current I_{OLED} via an external voltage, that is applied via a Parameter Analyzer. A photodetector is placed at a set known distance r from the OLED. The photoinduced current I_D is measured by the Parameter Analyzer as well. OLEDs are Lambertian emitters: the fraction of photons per second $d\phi_{Ph}$ emitted into the solid angle $d\Omega$ follows Lambert's cosine law: $d\phi_{Ph} = \phi_0 \cos(\theta) d\Omega$.

A photodetector is placed parallel to the OLED at a known distance r from the OLED. The detector's photocurrent I_D is measured by the Semiconductor Parameter Analyzer as well.

It is possible to calculate ϕ_{Ph} from I_D based on a series of considerations, that are presented in the following: The OLED emits photons into a semi-sphere with a Lambertian angle-dependence [45, 66]. Lambert's cosine law states that the fraction of photons per second $d\phi_{Ph}$ emitted into the solid angle $d\Omega$ is given by:

$$d\phi_{Ph} = \phi_0 \cos(\theta) d\Omega, \tag{4.3}$$

where ϕ_0 is the maximum number of photons per time and solid angle at $\theta = 0$. The solid angle $d\Omega$ can be expressed via spherical coordinates ($\theta \mathrel{\widehat{=}}$ polar angle, $\varphi \mathrel{\widehat{=}}$ azimuthal angle) as follows:

$$d\Omega = \sin(\theta) d\theta d\varphi \tag{4.4}$$

With this connection, **Equation 4.3** can be rewritten as:

$$d\phi_{\mathrm{Ph}} = \phi_0 \cos(\theta)\sin(\theta)\, d\theta\, d\varphi \tag{4.5}$$

Now, the total number of photons per time that are emitted into a semi-sphere around the OLED can be calculated by integrating over the entire semi-sphere:

$$\phi_{\mathrm{Ph}} = \int d\phi_{\mathrm{Ph}} = \int_0^{\pi/2} \int_0^{2\pi} \phi_0 \cos(\theta)\sin(\theta)\, d\varphi\, d\theta = \pi\phi_0 \tag{4.6}$$

ϕ_0 is the maximum number of photons per time and solid angle at $\theta = 0$. It can be experimentally obtained from the photocurrent I_{D} that is measured by the photodetector at a distance r and angle $\theta = 0$. The number of photons per time ϕ_{D} that hit the detector can be calculated via the photocurrent I_{D}:

$$\phi_{\mathrm{D}} = \frac{I_{\mathrm{D}}}{e\eta}, \tag{4.7}$$

where e is the elementary charge and η the detector's quantum efficiency (number of photoinduced charge carriers per number of incident photons). Now, ϕ_{D} needs to be divided by the solid angle Ω_{D} which is defined by the detector's area A_{D} in order to obtain ϕ_0.

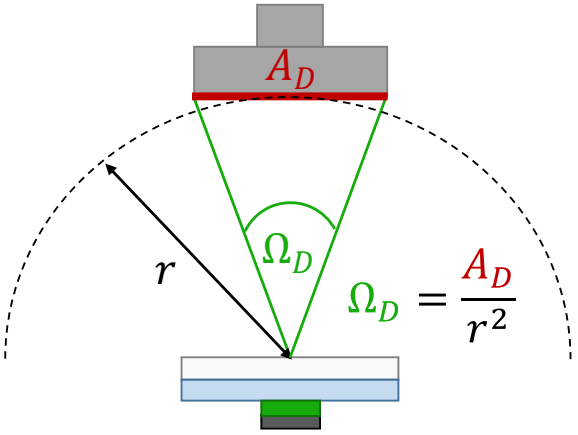

Figure 4.8: Connection between the detector area A_{D}, the distance between OLED and detector r and the solid angle Ω_{D}.

As illustrated in Figure 4.8, the connection between Ω_{D} and A_{D} is:

$$\Omega_{\mathrm{D}} = \frac{A_{\mathrm{D}}}{r^2} \tag{4.8}$$

With this, ϕ_0 can be expressed via I_{D} by combining **Equations 4.7** and **4.8**:

$$\phi_0 = \frac{\phi_{\mathrm{D}}}{\Omega_{\mathrm{D}}} = \frac{r^2 I_{\mathrm{D}}}{e\eta A_{\mathrm{D}}} \tag{4.9}$$

Finally, the EQE can be expressed according to **Equations 4.2**, **4.6**, and **4.9**:

$$\mathrm{EQE} = \frac{e\phi_{\mathrm{Ph}}}{I_{\mathrm{OLED}}} = \frac{e\pi\phi_0}{I_{\mathrm{OLED}}} = \frac{\pi r^2 I_{\mathrm{D}}}{\eta A_{\mathrm{D}} I_{\mathrm{OLED}}} \tag{4.10}$$

Now the EQE is fully expressed via measurables and known parameters. In order for that method to be reasonably accurate, the distance between OLED and photodetector needs to be sufficiently large. The assumption that ϕ_0 can be determined via the detector's photocurrent is only valid for reasonably large distances r. **Equations 4.8** and **4.9** assume that the angle θ between photodetector and OLED is zero over the entire area of the photodetector. This is an approximation, which becomes less valid the smaller r is.

4.5 Continuous Wave and Time-Resolved Photoluminescence

Further essential characterization methods for TADF emitters are continuous wave (cw) and time-resolved (tr) photoluminescence (cwPL, trPL) measurements on thin films of TADF emitters. cwPL and trPL measurements were performed with a calibrated fluorescence spectrometer *FLS980-s* (Edinburgh Instruments) equipped with a continuous broad-spectrum xenon lamp *Xe1*. Streak camera images were recorded with a *Streak Camera C5680* (Hamamatsu Photonics) using the second harmonic (400 nm) of a *MaiTai* laser (Spectra-Physics) as an excitation source. Those measurements were performed in collaboration with Liudmila Kudriashova. Details and explanations about the setups for PL measurements can be found in her PhD thesis "Photoluminescence Reveals Charge Carrier Recombination in Organic and Hybrid Semiconductors" [89].

4.6 Photometric Quantities and Color Coordinates

Measuring an OLED's emission spectrum in arbitrary units as well as an OLED's EQE allows the calculation of the radiometric quantity of the radiance $L_{\mathrm{e}}(\lambda)$ (see **Chapter 2**, **Section 2.11**). The radiance can be used to calculate the photometric quantity of the luminance $L_{\mathrm{v}}(\lambda)$, the color coordinates x and y and the correlated color temperature (CCT). Those calculations were performed via the free software *ColorCalculator* developed by *OSRAM SYLVANIA, Inc* [69].

5 Optically and Electrically Excited Intermediate States in Donor:Acceptor based OLEDs[1]

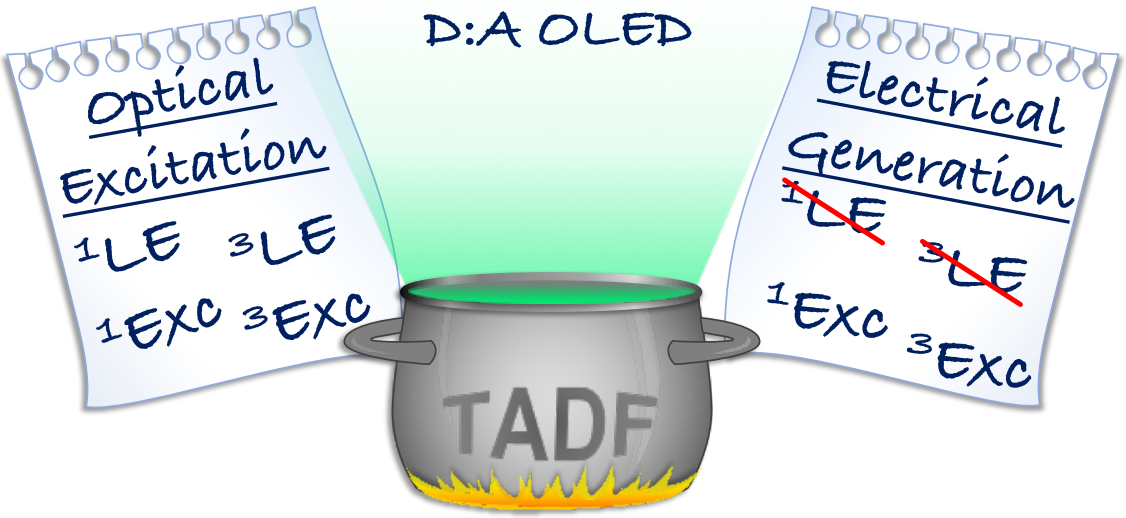

Using spin-sensitive techniques, we show that optical excitation and electrical generation in donor:acceptor TADF OLEDs involve different excited state pathways towards light emission.

[1] **The results of this chapter are published in**:
N. Bunzmann, S. Weissenseel, L. Kudriashova, J. Gruene, B. Krugmann, J. V. Grazulevicius, A. Sperlich and V. Dyakonov. Optically and electrically excited intermediate electronic states in donor: acceptor based OLEDs. *Materials Horizons*, **7**, 1126 (2020).

Abstract

Thermally activated delayed fluorescence (TADF) emitters consisting of donor and acceptor molecules are highly interesting for electroluminescence (EL) applications. Their strong fluorescence emission is considered to be due to reverse intersystem crossing (RISC), in which energetically close triplet and singlet charge transfer (CT) states, also called exciplex states, are involved. In order to distinguish between different mechanisms and excited states involved, temperature-dependent spin-sensitive measurements on organic light-emitting diodes (OLEDs) and thin films are essential. In our work we apply continuous wave (cw) and time-resolved (tr) photoluminescence (PL) spectroscopy as well as spin-sensitive EL and PL detected magnetic resonance to films and OLED devices made of three different donor:acceptor combinations. Our results clearly show that triplet exciplex states are formed and contribute to delayed fluorescence (DF) via RISC in both electrically driven OLEDs and optically excited films. In the same sample set we also found molecular triplet excitons, which occurred only in PL experiments under optical excitation and for some material systems only at low temperatures. We conclude that in all investigated molecular systems exciplex states formed at the donor:acceptor interface are responsible for thermally activated DF in OLEDs with distinct activation energies. Molecular (local) triplet exciton states are also detectable, but only under optical excitation, while they are not found in OLEDs when excited states are generated electrically. We believe that the weakly bound emissive exciplex states and the strongly bound non-emissive molecular triplet excited states coexist in the TADF emitters, and it is imperative to distinguish between optical and electrical generation paths as they may involve different intermediate excited states.

5.1 Introduction

The major drawback of conventional fluorescent organic light emitting diodes (OLEDs) is that due to spin statistics only 25% of injected electrons and holes form emissive singlet excitons, whereas 75% form long-lived triplets, which mostly decay non-radiatively [43, 44, 30, 54]. However, reverse intersystem crossing (RISC) from triplets to singlets is strongly enhanced, if the used materials are designed to exhibit an energy splitting ΔE_{ST} between the singlet and triplet state in the order of thermal energy $k_B T$ [90, 11, 10]. In this case, triplets can efficiently be harvested via thermally activated delayed fluorescence (TADF). One approach to achieve a small ΔE_{ST} is to find appropriate pairs of donor and acceptor molecules, where electrons and holes are located on different molecules to form so-called exciplex states [10, 91, 92]. Our work focuses on one of the

most prominent donor:acceptor TADF systems which is based on 4,4′,4″−Tris[phenyl (*m*-tolyl)amino]triphenylamine (m-MTDATA) as a donor and Tris(2,4,6-trimethyl-3-(pyridin-3-yl)phenyl)borane (3TPYMB) as an acceptor. After the initial report of efficient TADF from exciplex states between m-MTDATA and 3TPYMB in 2012 by Goushi et al. [10], several groups dedicated their attention to this system. A variety of experimental techniques were applied in order to rationalize the physics behind the observation of TADF. The used methods include transient electroluminescence (trEL) [93], magnetic field effects [94, 60], diffusion imaging [95] and even photovoltaic studies [96]. However, there is a lack of results from intrinsically spin-sensitive methods. Thus, a detailed understanding of the spin-forbidden upconversion mechanism from triplets to singlets is still missing. In this work we use techniques based on electron paramagnetic resonance (EPR), which are suitable tools to investigate spin states in OLEDs due to their sensitivity to triplets [27]. On the one hand, the broad spectrum of previous results from other experimental approaches allows us to compare our results and assess them within the context of existing models. On the other hand, we are able to fill the gap of missing results from spin-sensitive techniques. While few reports showed the application of transient EPR on films of intramolecular TADF emitters [25, 97], we previously demonstrated the application of EPR based methods on fully processed devices under realistic operation conditions [98]. Here, the methods of electroluminescence and photoluminescence detected magnetic resonance (ELDMR, PLDMR) were introduced and applied to donor:acceptor TADF systems for the first time. In this work, we now provide a more detailed analysis of donor:acceptor systems by application of photophysical characterization methods and a variety of advanced EPR based methods. The sum of the results of those different methods in their entirety allows for a comprehensible interpretation of the magnetic resonance data in terms of a better understanding of TADF emitters. In particular, we address issues regarding the activation energy of delayed fluorescence (DF) and if it is related to the energy gap ΔE_{ST} between exciplex singlet (^{1}Exc) and exciplex triplet (^{3}Exc) levels, or to molecular triplet states, e.g. to a triplet located on the donor (^3LE_D) or to a triplet located on the acceptor (^3LE_A) [24, 99, 26]. The goal of this work is to reveal, which spin-bearing species are involved in the light generation mechanisms of TADF based OLEDs. To make sure, that the conclusions we draw from EPR measurements on m-MTDATA:3TPYMB are not restricted to this particular system, we performed additional measurements on further donor:acceptor combinations. We used m-MTDATA as a donor and 4,7 Diphenyl-1,10-phenanthroline (BPhen) as an acceptor as well as Tri(9-hexylcarbazol-3-yl)amine (THCA) [100, 101] as a donor with BPhen as an acceptor. Not all measurements on those systems will be presented as detailed as

for m-MTDATA:3TPYMB, however, sufficiently extensive to draw accurate conclusions and to ensure comparability to m-MTDATA:3TPYMB. This allows to extend the validity of our findings to a broader spectrum of donor:acceptor systems.

5.2 Materials and Devices

The molecular components for exciplex based OLEDs investigated in this work are the donor-materials m-MTDATA and THCA combined with the acceptor-materials 3TPYMB and BPhen. **Figure 5.1** shows the corresponding molecular structures and the used OLED layer stack.

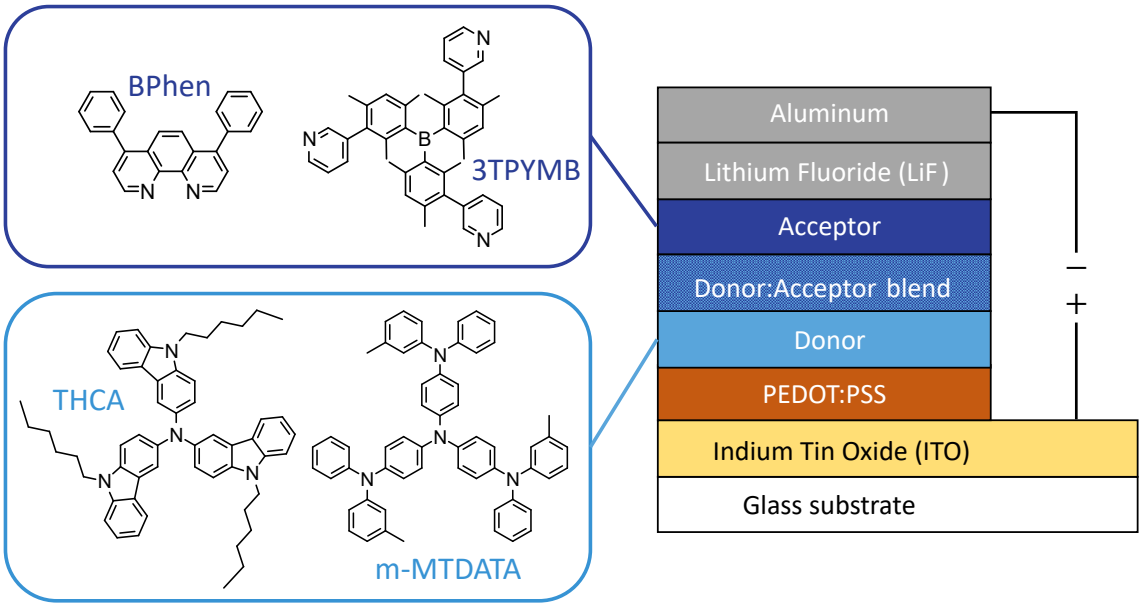

Figure 5.1: Molecular structures of donor and acceptor materials (left) and OLED layer stack (right).

An ITO anode covered with a PEDOT:PSS layer is used for hole injection and an aluminum cathode for electron injection. The emission layer consists of a 1:1 mixture of donor and acceptor materials, sandwiched in between layers of the respective pristine molecules, acting either as electron, or hole transport layer. An electroluminescence (EL) spectrum of such a device based on the combination m-MTDATA:3TPYMB as well as a photoluminescence (PL) spectrum of the respective pristine materials are depicted in **Figure 5.2a**.

One can recognize a clear red shift between the PL of the pure materials and the EL of a device, proving that the emission originates from energetically lower lying exciplex states formed at the interface between the two molecules. The energies of singlet and triplet levels of the involved states are shown in **Figure 5.2b**.

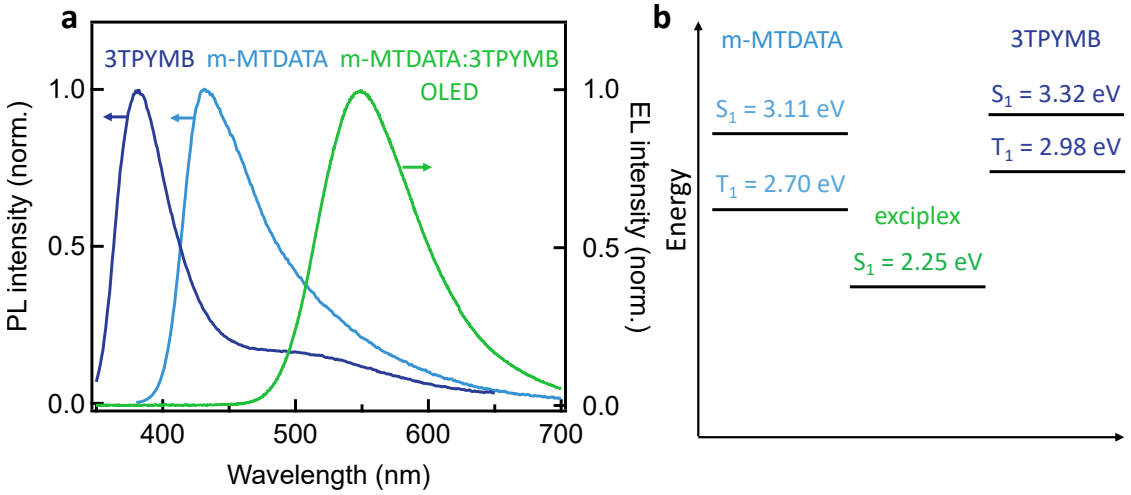

Figure 5.2: Optical characterization of m-MTDATA, 3TPYMB and their blend. **a**, PL spectra of pristine m-MTDATA and 3TPYMB together with an EL spectrum of an OLED based on those materials. The redshift between the EL spectrum and the PL spectra proofs exciplex formation. **b**, Energies of singlet and triplet levels for m-MTDATA, 3TPYMB and the exciplex state formed between them. Singlet energies are calculated from the peaks of PL spectra. Triplet energies are taken from [93]).

The material systems m-MTDATA:BPhen and THCA:BPhen show the same behavior (PL and EL spectra as well as energy levels can be found in [102].)

Exemplary current density and luminance versus voltage characteristics for an OLED based on m-MTDATA:3TPYMB at two different temperatures are shown in **Figure 5.3a** and the resulting EQE versus current density curves in **Figure 5.3b**.

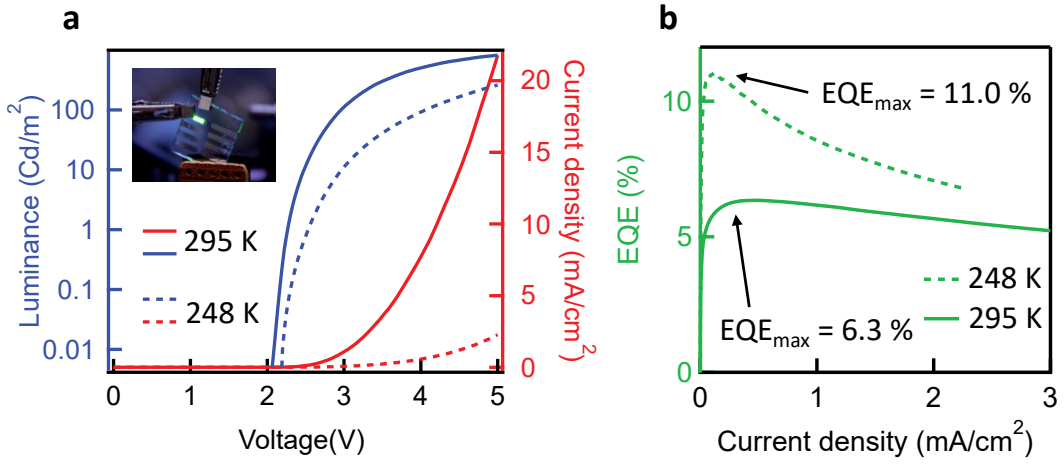

Figure 5.3: Electro-optical characterization of m-MTDATA:3TPYMB based OLEDs. **a**, OLED current density and luminance versus voltage characteristics at temperatures of 248 and 295 K. Inset: OLED device under test. **b**, External quantum efficiency versus voltage characteristics at T = 248 and 295 K.

With an optimized structure consisting of ITO / PEDOT:PSS / m-MTDATA(30nm) / m-MTDATA:3TPYMB(70nm,1:1) / 3TPYMB(30nm) / LiF(5nm) / Al(120nm), we reached a maximum EQE_{max} of 6.3% at room temperature (RT). We measured a photoluminescence quantum yield (PLQY) of 45% in oxygen free m-MTDATA:3TPYMB solid films, which allows for the estimation of a theoretical maximum EQE of 8.3% in OLEDs based on this donor:acceptor system (Calculation of a theoretical EQE from the PLQY can be found in [53]). The maximum EQE we measured for a device comes close to this theoretical value, while the discrepancy between the theoretical and experimental numbers might be attributed to leakage currents. Surprisingly, temperature dependent EQE measurements show that the efficiency increases at temperatures below room temperature. At T = 248 K an EQE_{max} of 11.0% was measured. While this observation is counterintuitive for TADF, we believe that the suppression of the non-radiative decay at lower temperatures actually outcompetes the decrease of RISC which is why efficiencies can increase below RT [103] (see the temperature-dependence of non-radiative decay rates in **Chapter 2**, **Section 2.4**). We therefore attribute the limitation of the EQE at RT to non-radiative losses. Still an EQE of 6.3% at RT exceeds the value of 5% which is the upper limit for purely fluorescent OLEDs (See **Chapter 2**, **Section 2.7**). In any case, our spin-sensitive experiments presented later on address the behavior of reasonably efficient, state-of-the art devices.

5.3 Time-Resolved Photoluminescence

In order to further investigate the optical properties of the materials used in this work, we performed time-resolved PL (trPL) measurements on an m-MTDATA:3TPYMB blended solid film. **Figure 5.4a** shows a streak camera image of such a film which displays emission between 0 and 1.5 ns after excitation.

Only emission from the exciplex singlet state (^{1}Exc) at around 550 nm can be observed within the measured time window. **Figure 5.4b** shows the PL transient of the observed exciplex emission on a longer time scale proving that the lifetime of the decay is in the microsecond range because of thermally activated fluorescence. Fitting the curve with a double exponential decay yields lifetimes of τ_1 = 3 μs and τ_2 = 12 μs. Since separated features of prompt and delayed fluorescence cannot be identified in the transient, these lifetimes do not necessarily represent the decay times of prompt and delayed fluorescence, but they demonstrate a distinct prolongation of the overall fluorescence lifetime due to thermally activated RISC (see also **Chapter 2**, **Section 2.10**).

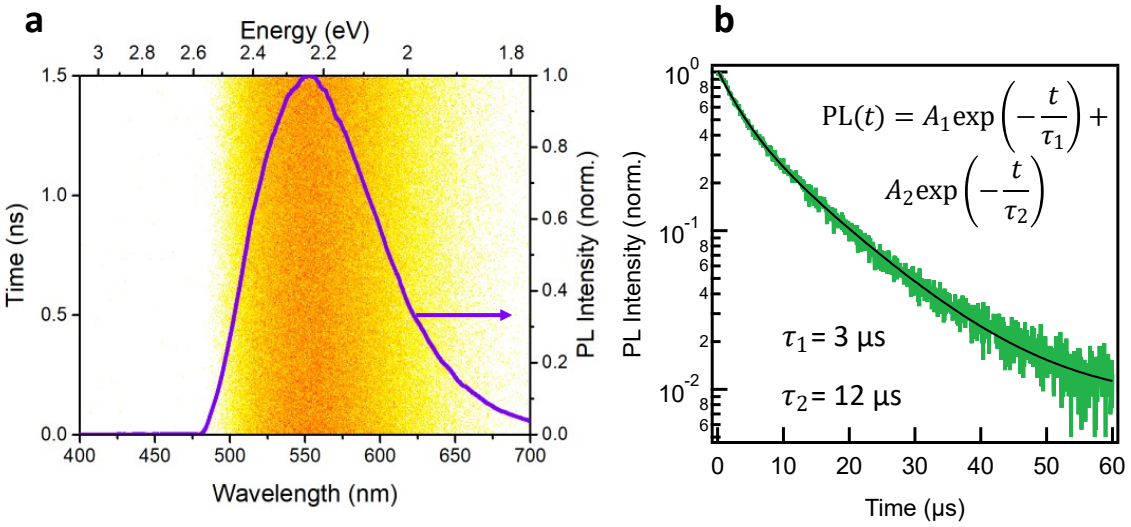

Figure 5.4: Time-resolved optical spectroscopy on m-MTDATA:3TPYMB blended films. **a**, Streak camera image of PL for excitation at λ_{exc}=400 nm together with an integrated spectrum over the 1.5 ns detection window. **b**, Transient PL decay over a range of several tens of microseconds. A sum of two exponential decays was used to fit the curve and the corresponding lifetimes were extracted.

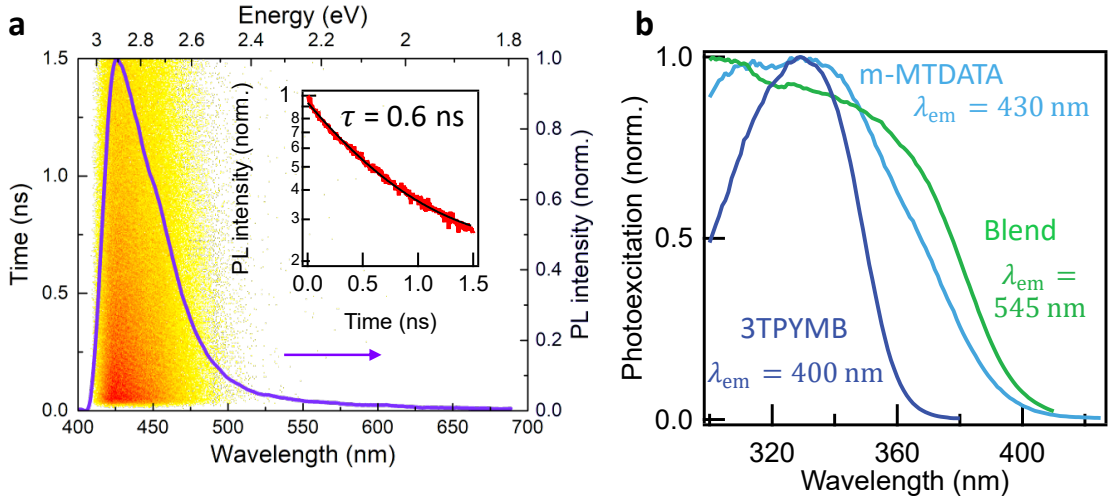

Figure 5.5: a, Streak camera image of PL from a pristine m-MTDATA film with an integrated spectrum over the 1.5 ns detection window. Inset: PL decay curve of this emission. A lifetime of 0.6 ns is obtained from fitting the transient with a single exponential decay. **b**, Photoexcitation spectra of pristine m-MTDATA, pristine 3TPYMB and an m-MTDATA:3TPYMB blended film. For each spectrum the wavelength λ_{em} at which the spectrum was recorded is given.

For comparison, a streak camera image of a pristine m-MTDATA solid film was recorded, as shown in **Figure 5.5a**. Here, emission between 400 nm and 450 nm occurs, reaching its peak at about 425 nm, which corresponds to the cw PL spectrum of m-MTDATA (see **Figure 5.2**). The decay of this emission is presented in the inset of **Figure 5.5**.

A lifetime of 0.6 ns is obtained from fitting the transient with a single exponential decay. Considering the negligibly small absorption of the exciplex state itself [26, 104, 105] it is remarkable that only exciplex emission is observed in the blended film while emission from m-MTDATA is completely quenched. According to photoexcitation spectra shown in **Figure 5.5b**, with the 400 nm laser in the streak camera measurement only m-MTDATA can be excited in the blended film. We conclude that the initial singlet excitation (^1LE_D) of the donor molecule m-MTDATA is followed by an electron transfer to the acceptor molecule 3TPYMB and the formation of an exciplex state within the instrument response time of 10 ps. This ultra-fast electron transfer outcompetes PL from m-MTDATA, which is similar to what is usually observed in donor:acceptor blends for organic photovoltaics [106, 107]. Intersystem crossing (ISC) from singlet (^1LE_D) to triplet state (^3LE_D) can also contribute to the efficient quenching of the m-MTDATA emission and will be discussed on the basis of magnetic resonance data in more details below.

An overview of the involved processes is schematically shown in **Figure 5.6**, illustrating how the exciplex state is formed after the charge transfer process, giving rise to μs long-living emission at 550 nm.

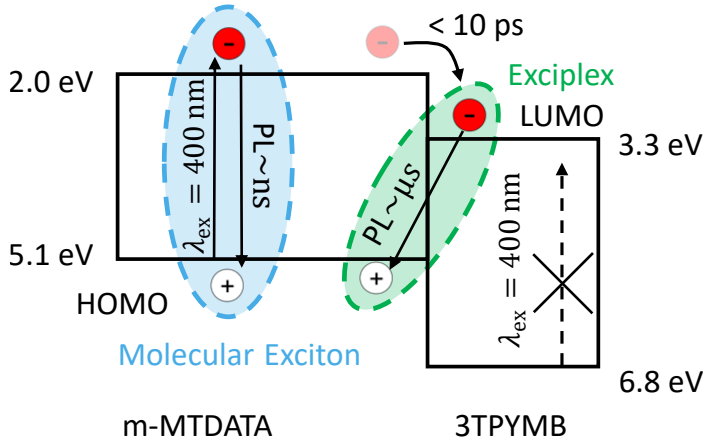

Figure 5.6: Illustration of the charge transfer process within the instrument response time of 10 ps after optical excitation of m-MTDATA with UV light. Energies for HOMO and LUMO are taken from [10].

5.4 Electroluminescence Detected Magnetic Resonance

In the next step, we applied EPR measurements. To clarify the spin sensitive mechanisms in OLEDs, ELDMR is the most suitable method as it directly probes EL.

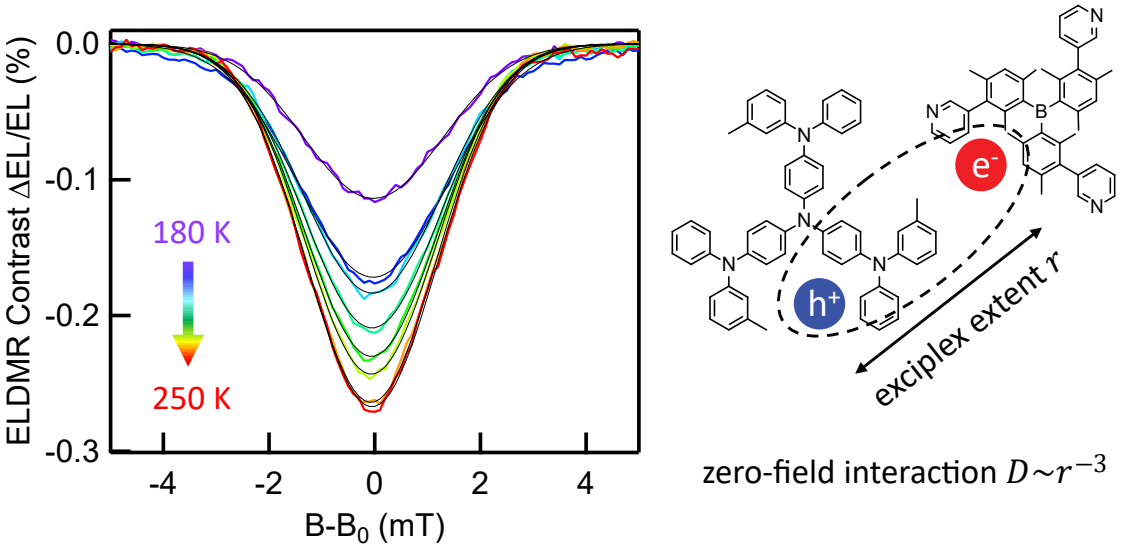

Figure 5.7: ELDMR measurements on m-MTDATA:3TPYMB-based OLEDs. **Left**: Temperature dependent ELDMR spectra exhibiting a Gaussian shaped curve. **Right**: Illustration of the extent r of the exciplex state which is delocalized over two adjacent m-MTDATA and 3TPYMB molecules. The zero-field splitting D is relatively small in such a case because it scales with r^{-3}.

Temperature-dependent ELDMR spectra measured on an m-MTDATA:3TPYMB OLED are shown in **Figure 5.7**. ELDMR measurements were performed according to **Chapter 4**, **Section 4.2**. Because ELDMR relies on the application of microwaves via a stripline, the used frequency slightly deviated for each measurement, as there is no unique resonance frequency for the stripline. To ensure comparability between different spectra, the ELDMR contrast is always plotted versus a magnetic field axis that is shifted to $B - B_0$, where B_0 is the resonant magnetic field for the respective measurement.

The ELDMR contrast for each temperature consists of a single, Gaussian shaped line without additional features. The emergence of such a signal was explained in detail in **Chapter 3**, **Section 3.3**. To remind, spin–spin interaction causes a zero-field splitting D that lifts the degeneracy of the $T_{\pm}$ and the T_0 triplet sublevels at zero magnetic field. For small D values, EPR absorption lines for the $T_+ \leftrightarrow T_0$ and the $T_0 \leftrightarrow T_-$ transitions overlap. An ELDMR experiment eventually measures the superposition of those two individual overlapping lines. As a result, a single broadened Gaussian shaped signal is observed. Furthermore, the zero-field splitting depends on the distance r between the two spins forming a triplet: $D \sim r^{-3}$. OLEDs based on m-MTDATA:3TPYMB rely on RISC from the exciplex triplet (^{3}Exc) to the exciplex singlet (^{1}Exc). For an exciplex state the interspin (electron–hole) distance is relatively large, as indicated in

Figure 5.7. A small zero-field splitting D is therefore expected and ELDMR on an m-MTDATA:3TPYMB based OLED yields a single Gaussian line.

The sign of the ELDMR contrast is negative. It was determined by measuring the microwave induced EL change with time resolution. The sign of signals that are detected via lock-in amplifiers is ambiguous [108]. Therefore, we used a high-sensitivity digital oscilloscope to determine the signal sign accurately. The sign of the ELDMR contrast, however, plays a marginal role for the conclusions of this work. Details are therefore not shown here, but can be found in [102].

Remarkable is the relative change ΔEL/EL in resonance of almost 1% at RT, which is large compared to the population difference between Zeeman sublevels expected from Boltzmann statistics (0.15% at RT, see **Chapter 3**, **Section 3.5**). From that observation we can conclude that electrically generated triplet exciplex states must be spin-polarized beyond Boltzmann statistics.

Figure 5.8a shows a comparison of normalized ELDMR spectra for each material system investigated in this work (m-MTDATA:3TPYMB, m-MTDATA:BPhen, THCA:BPhen).

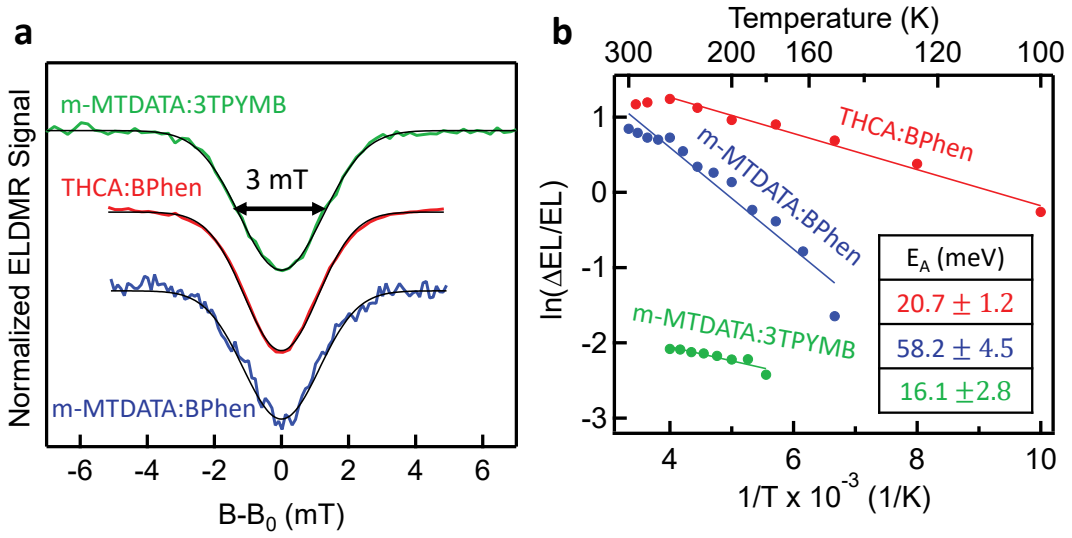

Figure 5.8: a, Comparison of ELDMR lineshapes for different donor:acceptor combinations at a temperature of T = 200 K. Each system exhibits a Gaussian line with similar width. **b**, Arrhenius plots of the integrated ELDMR spectrum for each donor:acceptor combination. The activation energy E_A is derived from the slope of linear fits and tabulated in the inset.

ELDMR spectra for all OLEDs show a similar signal shape with a full width at half maximum (FWHM) of around 3 mT. This similarity can be explained by the fact that the donor molecule in each case is either THCA or m-MTDATA, which have very similar molecular structures (see **Figure 5.1**). Although the electronic molecular environment determines the g-factor and hence the structure of the ELDMR signal,

g-factor differences are too small to be resolved in the used frequency range. On the other hand, an exciplex is a delocalized electron-hole pair over donor and acceptor molecules. As we will discuss in more detail later, the spatial separation between them is the parameter that might determine the ELDMR linewidth and since we expect a broad distance distribution of such pairs in the emissive blends, the influence of the structure of the involved individual molecules appears to be small and ELDMR signals appear rather similar for several donor:acceptor combinations.

Furthermore, all systems show the same temperature dependence (The full set of temperature-dependent ELDMR spectra for m-MTDATA:BPhen and THCA:BPhen can be found in the Supporting Information of [102]). Remarkably, the magnitude of the ELDMR contrast decreases with decreasing temperature (see **Figure 5.7**). This is completely opposite to what is commonly observed in EPR experiments, where lower temperatures lead to an increase in spin polarization according to Boltzmann statistics and therefore enhanced signals [27]. To ensure the same exciton generation rate for each temperature, all ELDMR spectra where measured at the same current density of 1 mA/cm^2. Consequently, the observed temperature dependence can be attributed to the thermal activation of RISC in TADF-based OLEDs, unambiguously proving the TADF nature of the observed EL. From the temperature dependence of the ELDMR signal intensities we can calculate the activation energy E_A from an Arrhenius plot (as introduced in **Chapter 2**, **Section 2.10**). ELDMR is not yet a widely used method to determine E_A, although it probes the OLED response to a very fast spin-flip in the electron-hole pair, i.e. without possible artifacts due to charge injection, transport and exciplex formation. **Figure 5.8b** shows Arrhenius plots of the integrated ELDMR spectral intensity for OLEDs made with three different material systems. From the slope of linear fits, values for E_A were calculated for each material system. These values are in the range between 16 and 58 meV, which is in good agreement with the values for ΔE_{ST} of other donor:acceptor-based TADF systems [10, 109, 110]. Based on the assumption that the singlet exciplex is the emissive state and its population occurs via RISC from the triplet exciplex state, we consider the deduced activation energies as good approximations for the singlet-triplet gap ΔE_{ST}, since ELDMR probes thermally activated spin-conversion.

To ensure that the observed ELDMR signals are directly related to the emitting layer, but not to spin-dependent transport or injection in the adjacent transport layers or at the interfaces, comparative EDMR measurements on fully processed OLEDs without TADF emissive layers were performed. To remind, EDMR probes the microwave-induced change of current through the OLED while a constant voltage is applied to the device. ELDMR and EDMR on an OLED (m-MTDATA:3TPYMB) yield identical signals, as shown in **Figure 5.9**.

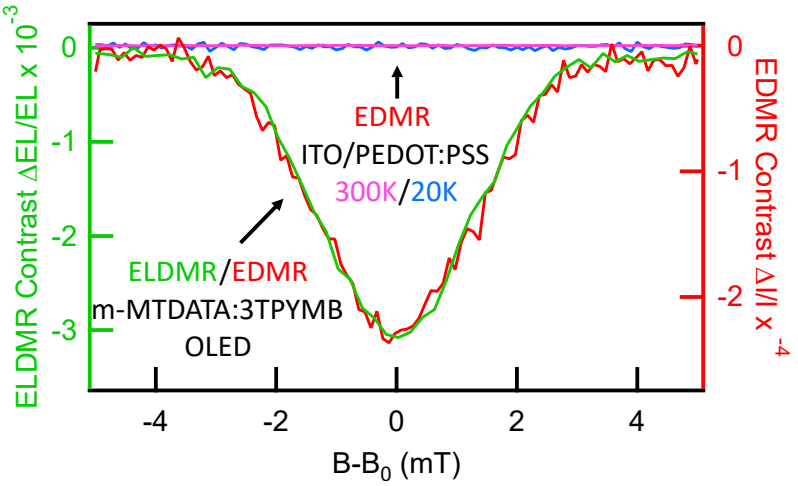

Figure 5.9: Comparison of ELDMR and EDMR spectra for m-MTDATA:3TPYMB based OLEDs. The scaling for each curve is chosen such that the lineshapes are comparable. Both methods yield identical lineshapes implying the same spin-states are involved in recombination. As a reference, a PEDOT:PSS-only device (without emitter layer) shows no spin-resonance effect on the current between 20 and 300 K, which excludes spin-dependent effects in the transport layers.

However, the relative change of the current in resonance is about one order of magnitude smaller than the ELDMR contrast. The reference sample, consisting of ITO/PEDOT:PSS without donor and acceptor layers, yields no EDMR signal at temperatures between 20 K and 300 K at all. These observations clearly show that the ELDMR and EDMR signals originate from the same spin-dependent mechanisms in the emissive layer and we can exclude spin-dependent transport, or injection in the anode and cathode layers as source of the observed effects. Moreover, we speculate that the EDMR signal is induced by the ELDMR effect. A change of the recombination rate of exciplex states in magnetic resonance under constant voltage conditions can give rise to a change in the current. Consequently, the occurrence of an ELDMR signal can induce a smaller EDMR signal of identical shape. Similar correlations between a change in EL and current are observed in magnetic field effect studies on donor:acceptor based TADF OLEDs [60].

The details of the RISC mechanism are also non-trivial. As explained in **Chapter 2**, **Section 2.4** a spin-mixing mechanism is needed for RISC to have a finite transition rate. Recent reports attribute the driving force of RISC in donor:acceptor-based TADF emitters to the so-called Δg mechanism [60, 111]. This mechanism facilitates intersystem crossing between the singlet state S and the triplet state T_0 due to a difference in spin precession frequencies $\Delta\omega_P$ which arises from a difference in electron spin g-factors Δg in the presence of an external magnetic field B ($\Delta\omega_P = \mu_B \Delta g B/\hbar$) [112]. For donor:acceptor systems, a contribution of the Δg-mechanism

can be expected because electron and hole, which form the exciplex state, reside on adjacent non-identical molecules. In order to obtain an estimate value for Δg in our OLEDs, we performed ELDMR measurements over an extensive range of magnetic fields (25 mT – 1.4 T) and microwave frequencies (0.7 GHz – 38 GHz) which is possible with the stripline approach used for this work (see **Chapter 4**, **Section 4.2**). Exemplary spectra for three different frequencies are shown in **Figure 5.10a**.

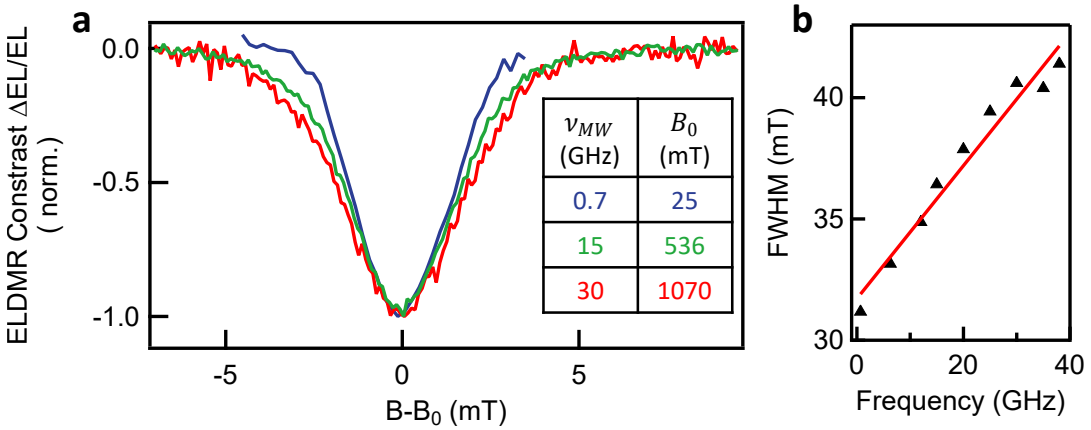

Figure 5.10: Frequency dependence of ELDMR spectra. **a**, Exemplary normalized ELDMR spectra for three different microwave frequencies. The frequencies and the corresponding resonant magnetic fields are tabulated in the inset. **b**, Frequency dependent full width at half maximum (FWHM) over the full used frequency range. The data points follow a linear dependence.

Figure 5.10b shows the frequency dependent linewidth of ELDMR spectra over the entire used frequency spectrum. An increase of the linewidth with increasing frequency is observed which indicates a non-negligible Δg (see **Chapter 3**, **Section 3.3**). We used the software package EasySpin [113] to perform a global fit of all spectra in the accessible frequency range and extracted an upper limit for Δg of $9.2 \cdot 10^{-4}$. We emphasize that this value is derived directly from spectroscopic data and is not deduced by modeling magnetic field effects, such as magneto electroluminescence (MEL). In [60], the assumption of $\Delta g = 10^{-4}$ was sufficiently large to explain magnetic field effects in m-MTDATA:3TPYMB based OLEDs with a dominant Δg-mechanism. Investigations on other organic materials report values for Δg in the range of 10^{-3} to 10^{-4} [114]. Our measurement is consistent with these numbers and thus supports the scenario that Δg-mechanism is responsible for RISC.

5.5 Photoluminescence Detected Magnetic Resonance

Next, we measured PLDMR on m-MTDATA:3TPYMB blended solid films at temperatures between 50 and 290 K, as shown in **Figure 5.11a**.

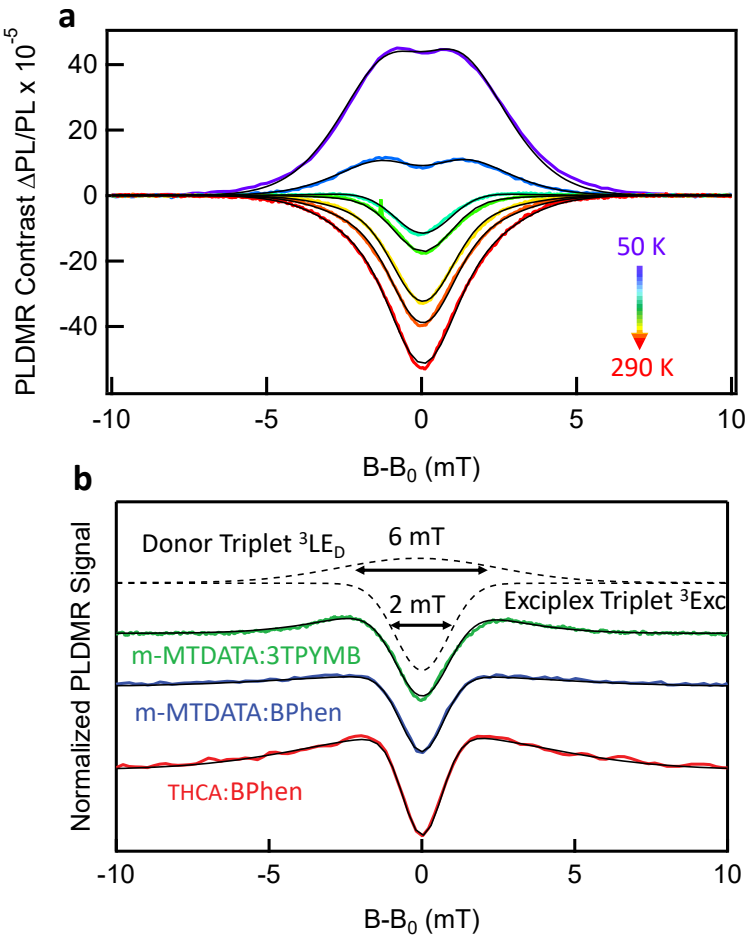

Figure 5.11: PLDMR measurements on donor:acceptor blends. **a**, Temperature dependent PLDMR measurements on m-MTDATA:3TPYMB blended films. **b**, Comparison of PLDMR spectra for different donor:acceptor combinations at a temperature of T = 200 K.

The first thing one notices is another shape of the spectrum. All spectra consist of a superposition of a narrow and a broad component with Gaussian shape and the broad component becomes more and more visible as temperature decreases. Also here we used an oscilloscope instead of a lock-in amplifier for an accurate determination of the signal's sign (details see [102]). The broad component exhibits a positive sign and the narrow component a negative one.

A full set of temperature-dependent PLDMR spectra from blended solid films of the donor:acceptor combinations m-MTDATA:BPhen and THCA:BPhen can be found in the Supporting Information of [102]. Those spectra exhibit a comparable behavior. **Figure 5.11b** presents normalized PLDMR spectra of all studied donor:acceptor blends showing that each system yields comparable signals. In order to separate the positive broad and the negative narrow contribution, we exemplary fitted the PLDMR spectrum of m-MTDATA:3TPYMB with two Gaussians, shown as dashed lines in the upper part of **Figure 5.11b**. The narrow PLDMR component is very similar to the ELDMR signals in sign and form, but has a slightly smaller linewidth of 2 mT compared to 3 mT in ELDMR. The reason for this can be slightly different spatial distributions of electron-hole pairs, as will be explained in more detail later. But the broad PLDMR component with a linewidth of 6 mT is clearly a new feature not present in ELDMR.

5.6 Discussion

In order to assign the detected signals in ELDMR and PLDMR to particular excited states, we assume that electrical injection predominantly populates the energetically lowest triplet state according to spin statistics. In the donor:acceptor blends that we studied this is the triplet exciplex state (^{3}Exc) (see energies of the molecular singlet and triplet states as well as exciplex singlet state in **Figure 5.2b**). The unusual temperature behavior strongly supports the scenario that the signals occurring in ELDMR and EDMR are due to thermally-activated RISC between triplet (^{3}Exc) and singlet exciplex (^{1}Exc) states.

The narrow components in PLDMR and in ELDMR have slightly different widths, however they are very similar in shape and, most importantly, in temperature-dependence. We therefore assign the narrow PLDMR peak to exciplex triplets (^{3}Exc), too. Although both PLDMR and ELDMR probe the exciplex triplet, their relative magnitudes (ΔPL/PL and ΔEL/EL) differ by at least a factor of 10. This can be due to different spin statistics. For optical excitation, triplet exciplex states are formed via ISC from optically generated singlets whereas for electrical injection triplet exciplex states are directly formed with a probability of 75% thus giving rise to a higher ELDMR contrast.

The second component in the PLDMR signal is a factor of two broader and therefore should have a different origin. We attribute it to molecular triplet excitons (^{3}LE), either on the donor or the acceptor molecule. The more localized character leads to a stronger dipolar-coupling D than in exciplex triplets, which are delocalized over at least two molecules. As explained previously, D determines the linewidth of the magnetic

resonance spectra. Therefore, PLDMR from a localized triplet exciton on the donor or acceptor molecule is expected to be broader.

The assignment of the broad PLDMR component to a localized triplet is further supported by the observation of a half-field signal. PLDMR measurements on blended solid films of m-MTDATA:3TPYMB and m-MTDATA:BPhen exhibit this feature, as shown in **Figure 5.12**.

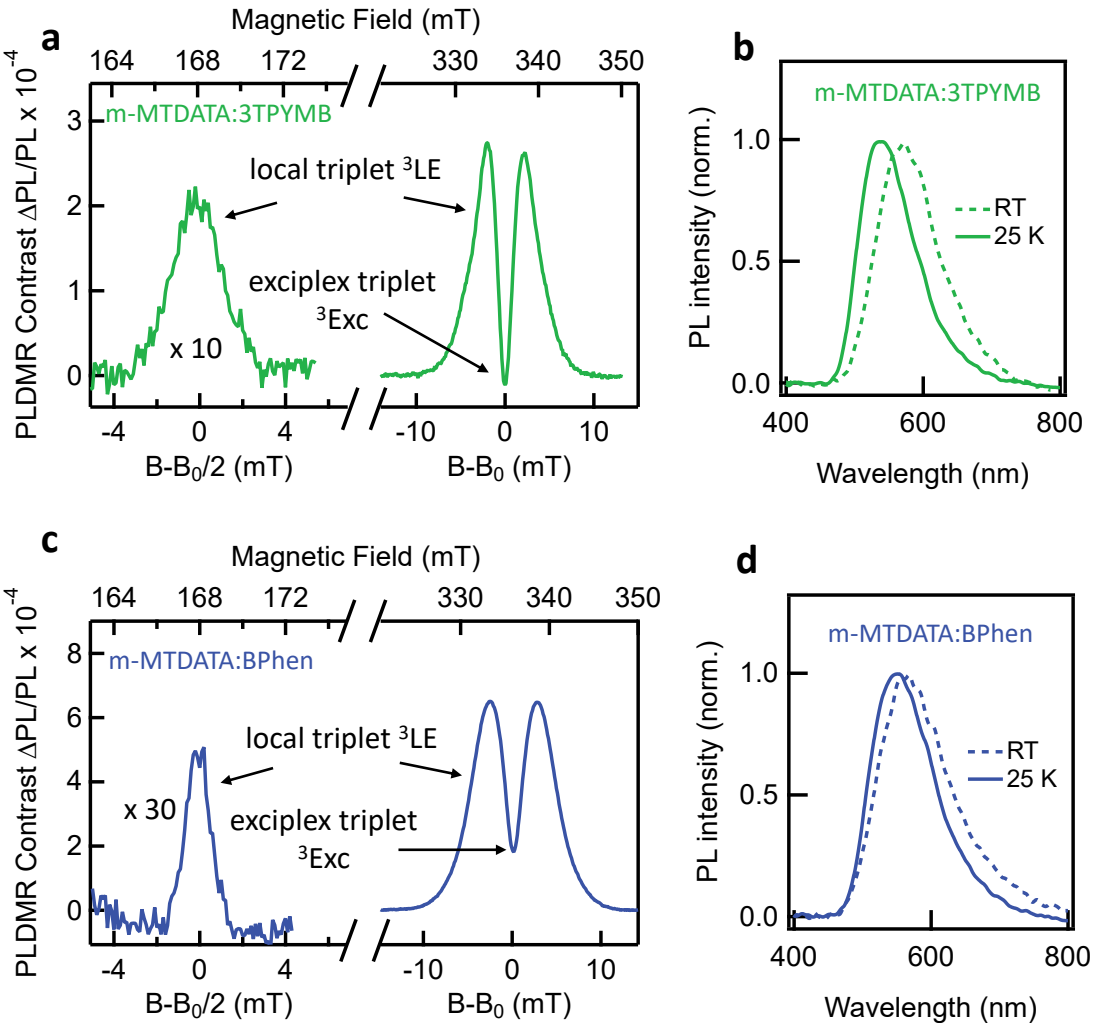

Figure 5.12: Half-field signals in donor:acceptor blends. **a**/**c**, Half-field and full-field PLDMR measurements on m-MTDATA:3TPYMB/m-MTDATA:BPhen blended films at T = 25 K. Full-field signals consist of a superposition of a narrow and a broad component. The narrow component is assigned to the exciplex triplet. The broad component and the half field signal are assigned to a local triplet. For better visibility, the signal intensities of half-field signals are magnified by a factor of 10 (m-MTDATA:3TPYMB) and 30 (m-MTDATA:BPhen), respectively. **b**/**d**, PL spectra at RT and 25 K for m-MTDATA:3TPYMB/m-MTDATA:BPhen showing exciplex emission at both ambient and low temperatures.

As explained in detail in **Chapter 3**, **Section 3.4**, half-field signals arise from a spin-flip transition with a change of spin quantum number $\Delta m_s = 2$, i.e. between the T_+ and the T_- triplet sublevel. Half-field signals are detected at half the magnetic field $B_0/2$ of the full-field transition centered at $B = B_0$. Their occurrence is unambiguous proof that the signal stems from a high spin state, since spin 1/2 particles cannot show a $\Delta m_s = 2$ transition. Polarons are therefore excluded as a potential origin of the broad PLDMR component. On the other hand the intensity of a half-field transition is proportional to r^{-6}, where r is the distance between the spin carrying particles. Since r is expected to be relatively large for exciplex triplets, the occurrence of a half field signal is not expected for exciplex states. We therefore conclude that the half-field signal must be assigned to a local triplet where r is expected to be smaller.

The half-field signals are measured at 25 K which is necessary to achieve sufficient signal to noise ratio. **Figures 5.12b** and **d** show temperature dependent PL spectra of the samples that were used to measure the half-field signal in PLDMR. Both material systems show exciplex emission at RT and 25 K. This observation ensures that there is no fundamental difference in the photophysics of the investigated molecular system between ambient and low temperatures. There is only a slight blue shift between RT and 25 K which is often observed in organic molecules.

An important consequence of the above assignment is that our experiments do not provide any evidence for the involvement of local triplets (^3LE_D or ^3LE_A) in the emergence of delayed fluorescence in electrically driven devices although our detection scheme is sensitive enough to probe them. Therefore, we cannot justify a scenario, in which the exciplex state couples to energetically higher lying local triplets via spin-orbit coupling [24, 99, 26], as in this case we would expect triplet signatures in ELDMR, too.

We now discuss the relationship between the width of the ELDMR/PLDMR lines and the spatial separation of electron and hole, which form a bound state. From EPR spectra, the distance between electron and hole $r_{e\text{–}h}$ can be estimated by the following equation [73]:

$$r_{e\text{–}h}[\text{nm}] = \sqrt[3]{\frac{2.785}{D[\text{mT}]}}\text{nm} \tag{5.1}$$

Here $r_{e\text{–}h}$ is obtained in units of nm, if D is used in units of mT. We use the FWHM as an upper limit for $2D$, as we cannot fully exclude other mechanisms of the EPR line broadening, e.g. unresolved hyperfine interactions with surrounding nuclei (see **Chapter 3**, **Section 3.3**). Consequently, a lower boundary for $r_{e\text{–}h}$ can be calculated by using **Equation 5.1**. From the FWHM of our ELDMR spectra, one finds $2D \leq 3$ mT result-

ing in $r_{e\text{–}h} \geq 1.2$ nm (electrical generation), while for the narrow PLDMR component we estimate $2D \leq 2$ mT resulting in $r_{e\text{–}h} \geq 1.4$ nm (optical excitation). The broad ^{3}LE PLDMR component yields $2D \leq 6$ mT resulting in $r_{e\text{–}h} \geq 1.0$ nm. These numbers can be explained by the different triplet formation mechanisms for electrical injection and optical excitation.

Figure **5.13a** shows an illustration of the triplet exciton formation in the case of electrical generation.

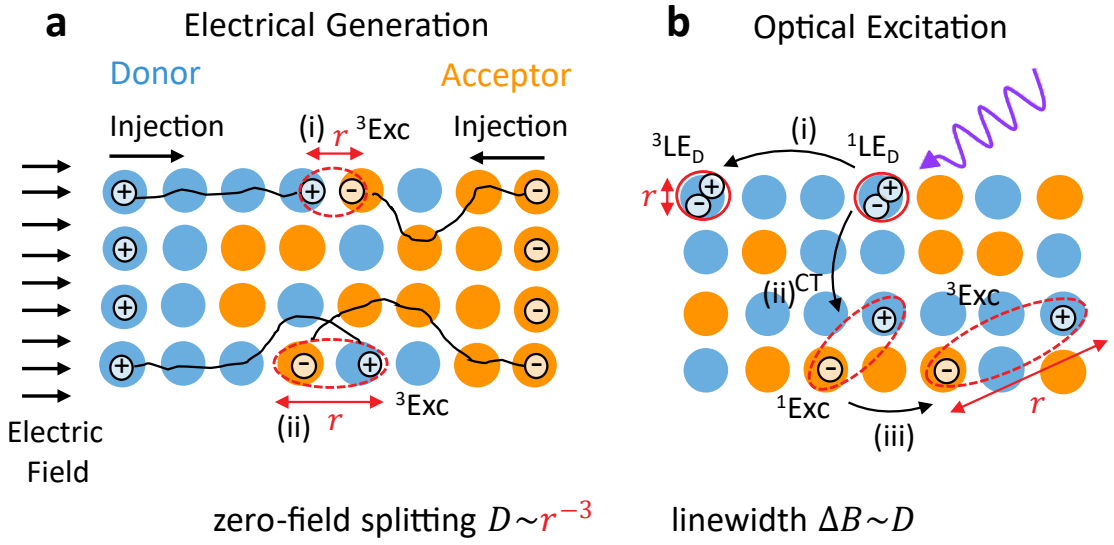

Figure 5.13: Illustration of triplet formation mechanisms in donor:acceptor blends. Each circle represents a donor or acceptor molecule. **a**, Triplet formation via electrical generation. Electrons and holes are injected into the mixed layer of the OLED and form excited states, 75% of which are triplet exciplex states (^{3}Exc). The spatial separation of the e–h pairs r can vary by the electric field. **b**, Triplet formation via optical excitation. Initially, only singlet excitons are formed in the donor phase (^{1}LE$_D$). They can diffuse and undergo ISC to form molecular triplet excitons (^{3}LE$_D$) (i). Alternatively, the donor singlet (^{1}LE$_D$) can undergo a charge transfer to form an exciplex singlet (^{1}Exc) (ii). Subsequently, an exciplex triplet (^{3}Exc) can be formed (iii). Note that the zero-field splitting D and hence the ELDMR/PLDMR line width ΔB can vary due to the broad distribution of the electron-hole separations r.

Here electrons and holes form exciplex triplets (^{3}Exc) in the emission layer, which consists of a mixture of donor and acceptor molecules (see also **Figure 5.1**). Attar et al. [104] reported that a voltage, which is applied to a mixed m-MTDATA:3TPYMB layer, broadens the distribution of distances between electrons and holes forming exciplex states. Depending on the orientation of the exciplex dipoles with respect to the E-field, the electrostatic force causes either their compression (**Figure 5.13a i**) or expansion (**Figure 5.13a ii**), which leads to a broadening of the distribution of the electron hole

radii. According to **Equation 5.1**, this leads to a distribution of zero-field splitting parameters D and thus to a broadening of the ELDMR line.

In contrast, PLDMR probes triplet states formed via ISC after optical excitation, i.e. without applied voltage. The respective processes are illustrated in **Figure 5.13b**. Initially excited donor singlets (^1LE_D) can diffuse and undergo ISC to form a molecular triplet (^3LE_D) on the donor (**Figure 5.13b i**). In this case, electron and hole are located on the same molecule resulting in a broad PLDMR spectrum. We measured a PLQY of 6% in oxygen-free m-MTDATA solid films. A significant amount of optically excited singlet states must therefore undergo a non-radiative transition instead of emitting light. Potential non-radiative decay channels are given by non-radiative decay to the singlet ground state or by ISC to the triplet excited state. A PLQY as low as 6% indicates a non-negligible contribution of ISC which explains the population of donor triplets.

Alternatively, donor singlets can undergo CT to form a singlet exciplex state (^{1}Exc) (**Figure 5.13b ii**). The depopulation of donor singlets via ISC and CT appears to be very efficient since we do not observe any emission from the donor phase in blended m-MTDATA:3TPYMB films (see **Figure 5.4**). At low temperatures, the contribution of ISC appears to increase as the broad PLDMR component is more pronounced. This behavior might be explained by a decreased rate of CT, which is mediated by temperature activated molecular vibrations [115]. Magnetic field effect studies on m-MTDATA:3TPYMB report that optically excited exciplex states can diffuse over distances of up to 10 nm within the film, while the electron-hole distance increases during this diffusion process [95, 94] (**Figure 5.13b iii**). Consequently, a decreased zero-field splitting D and therefore linewidth is expected in PLDMR, yielding the narrow component.

5.7 Summary

Figures 5.14 and **5.15** summarize the excitation pathways of singlet and triplet states for electrical generation and optical excitation.

For the exact energies of singlet and triplet states of m-MTDATA:3TPYMB see **Figure 5.2**. Energies for m-MTDATA:BPhen and THCA:BPhen can be found in the Supporting Information of [102], however the relative positions of the energy levels for m-MTDATA:3TPYMB are representative for all investigated systems.

In an electrically driven OLED, free charges are injected to form excitons in the emissive layer. As presented in **Figure 5.14**, the exciplex singlet (^{1}Exc) and triplet (^{3}Exc) are the energetically lowest states within the system, which is why they are preferably populated. Singlets decay immediately as prompt fluorescence (PF), whereas triplets can undergo thermally activated RISC giving rise to delayed fluorescence (DF).

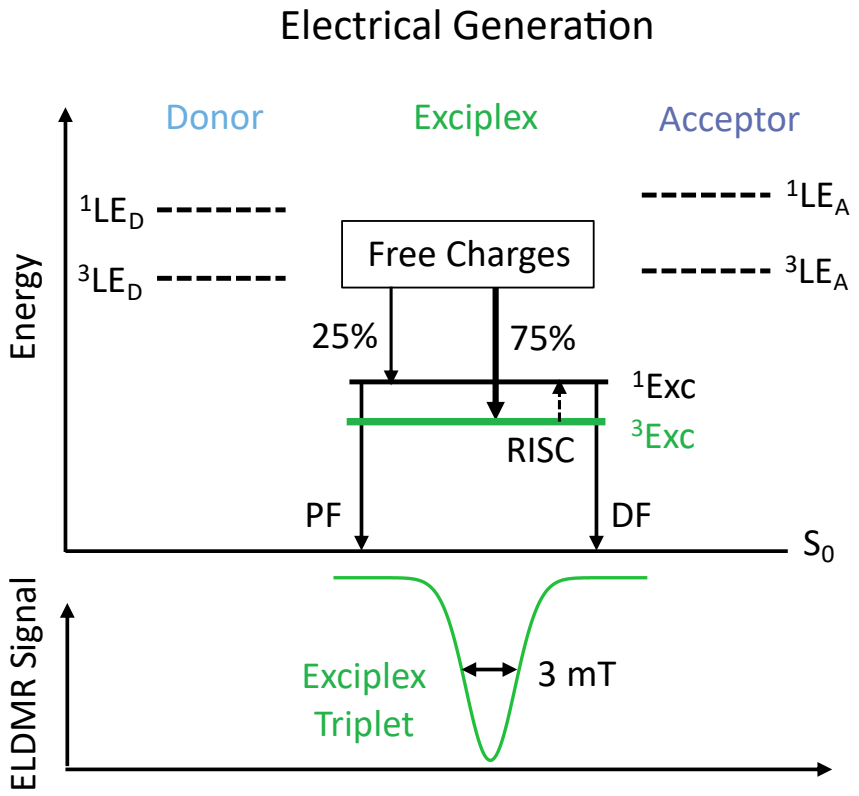

Figure 5.14: Excitation pathways for electroluminescence. Exciplex singlet ^{1}Exc and triplet ^{3}Exc states are formed from free charges. ^{1}Exc can decay directly emitting prompt fluorescence (PF), while RISC between ^{3}Exc and ^{1}Exc enables delayed fluorescence (DF). ELDMR shows a single Gaussian line which is attributed to the exciplex triplet.

In ELDMR, spin-flip transitions in the exciplex triplet significantly change the EL intensity. Neither can the emission of molecular singlet excitons in the EL spectrum of an OLED be observed, nor can characteristic signatures of molecular triplets be found in ELDMR. Therefore, triplets of pristine materials (^3LE_D or ^3LE_A) are hardly involved in the light generation mechanism of electrically driven devices.

Another scheme can be drawn for the optical excitation of the donor:acceptor blends studied in our work, as illustrated in **Figure 5.15**. Here, UV excitation at 365 nm first generates singlet excitons on donor molecules (^1LE_D), while the acceptor molecule with an even larger band gap cannot be excited at this wavelength. The singlet exciton of the donor undergoes either ISC to the donor triplet state (^3LE_D) or CT, which forms the exciplex singlet (^{1}Exc) on a picosecond time scale. Donor triplets subsequently undergo CT to exciplex triplets (^{3}Exc). Exciplex singlets (^{1}Exc) decay radiatively as PF or form exciplex triplets (^{3}Exc) via ISC. Finally, the exciplex triplets are upconverted back to singlet exciplexes via thermally-activated RISC, giving rise to DF. In PLDMR, the exciplex triplets appear as a narrow signal, which is almost identical to the ELDMR signal.

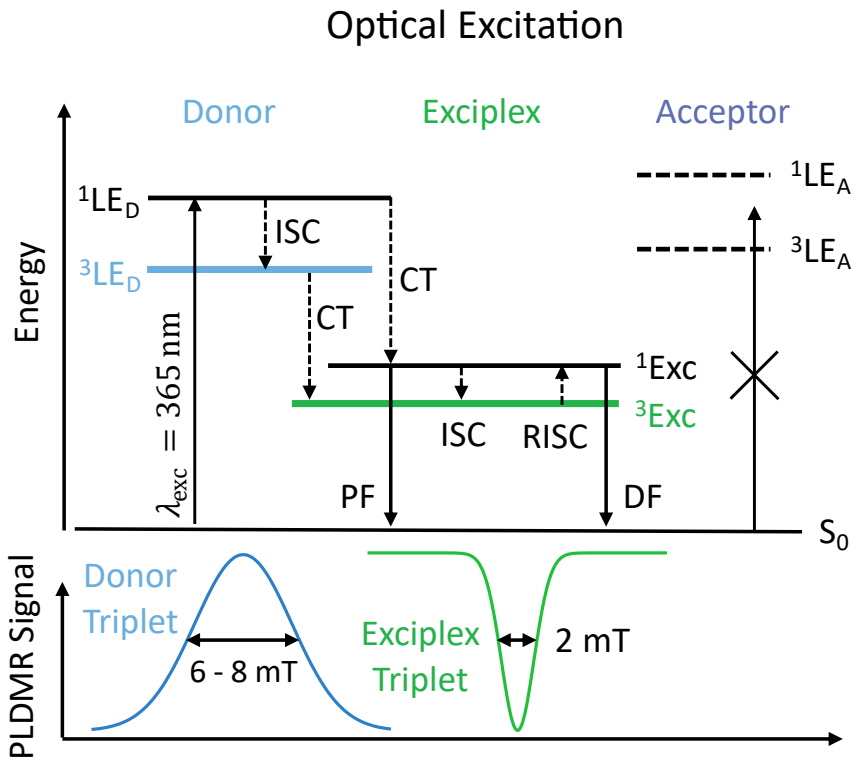

Figure 5.15: Summary of excitation pathways for photoluminescence. Donor singlets ^1LE_D are initially created via optical excitation. ^1LE_D is depopulated via CT to the exciplex singlet ^{1}Exc and ISC to the donor triplet ^3LE_D. Subsequent ISC of ^{1}Exc populates the exciplex triplet ^{3}Exc. These triplets can be upconverted back to singlets, enabling DF. Donor triplets ^3LE_D formed via ISC can populate ^{3}Exc via CT. In PLDMR, a broad signal of the donor triplet and a narrow signal of the exciplex triplet are observed.

A broad component in PLDMR is due to the molecular triplet exciton on the donor molecule, however its population is strongly temperature dependent. Note that the molecular triplets on the acceptor molecules were not considered in the scheme because they could not be generated with the available excitation energy.

5.8 Conclusion

We applied three different spin-sensitive techniques in order to reveal the role of spin-bearing excited states in the light generation mechanism of TADF-based films and OLEDs. In the case of electrical injection of charge carriers in the donor:acceptor emissive layer, which leads to EL, we found a characteristic signature of the triplet exciplex states (^{3}Exc) in ELDMR. By driving spin-flip transitions within triplet exciplex states the EL intensity changes by up to 1%. This is much higher than what is expected from Boltzmann statistics at room temperature. From the temperature dependence,

we deduced the activation energy of this process, which depends strongly on the donor:acceptor combination and is between 16 and 58 meV. We have assigned this characteristic energy to a singlet-triplet gap and the underlying mechanism of up-conversion via RISC. The underlying TADF mechanism includes a kinetic singlet-triplet exchange based on the g-factor difference, which ensures the conservation of angular momentum, while energy conservation is ensured by a thermal energy supply. As no molecular triplets are observed in the OLED experiments, we suppose they cannot be excited electrically. In the case of optical excitation of donor:acceptor films, the signature of triplet exciplex states (^{3}Exc) is observed in PL and it is similar to the one observed in EL from OLEDs. Additional spectral features from the triplet excitons localized on the donor molecules (^3LE_D) are also found, but their appearance strongly depends on the material system and on the temperature. Our experiments clearly show that the excited state which is majorly responsible for the occurrence of TADF in donor:acceptor systems is the triplet exciplex state (^{3}Exc). Molecular triplet excitons do not show up at all in efficient OLEDs, but only appear under optical excitation and in some systems mainly at low temperatures. We also emphasize the importance of comparative spin-sensitive, temperature-dependent PL and EL measurements, since the intermediate generation and recombination pathways may differ substantially.

5.9 Additional Experimental Details

The most important experimental details are explained extensively in **Chapter 4**. More information that is specific for this chapter is given in the following.

The materials m-MTDATA and BPhen were purchased from Sigma-Aldrich. 3TPYMB was purchased from Lumtec (Luminescence Technology Corp.). THCA was supplied by A. Dabuliene and Prof. J. V. Grazulevicius from the Department of Polymer Chemistry and Technology at Kaunas University of Technology, Radvilenu pl. 19, LT-50254 Kaunas, Lithuania. All materials were used as received.

All OLED devices were fabricated on Indium Tin Oxide (ITO) covered glass substrates (1 cm^2). First, poly(3,4-ethylendioxythiophene):polystyrolsulfonate (PEDOT:PSS, 4083Ai) from Heraeus was spin coated, resulting in a 40 nm thick film. All further device fabrication steps were done inside a nitrogen glovebox to avoid degradation, starting with annealing of the PEDOT:PSS layer for 10 minutes at 130°C. For m-MTDATA:3TPYMB devices, 30 nm donor and 30 nm acceptor were thermally evaporated in an evaporation chamber with an additional 70 nm mixed layer (1:1) in between the pristine material layers. For THCA:BPhen devices, THCA was spin-coated from chlorobenzene solution yielding a layer thickness of 50 nm followed by evapo-

ration of a 40 nm BPhen layer (bilayer device). For m-MTDATA:BPhen both methods were used yielding identical results for the spin-dependent EDMR and ELDMR measurements. The top electrode for all devices was evaporated (5 nm Ca / 120 nm Al), completing OLEDs with 3 mm^2 each. Evaporation rates for Ca were 0.3 Å/s and for Al 3 Å/s.

5.10 Contributions to this Chapter

Nikolai Bunzmann[1] (N.B.), Sebastian Weißenseel[1] (S.W.), Andreas Sperlich[1] (A.S.) and Vladimir Dyakonov[1] (V.D.) designed the experiments. N.B., S.W., Benjamin Krugmann[1] and Jeannine Gruene (J.G.) prepared the devices. N.B., S.W., Juozas Vidas Grazulevicius[2] (J.V.G.) provided the molecule THCA, B.K. and J.G. carried out electro-optical device characterization. N.B., S.W., B.K, J.G and A.S. performed the magnetic resonance measurements. Liudmila Kudriashova[1] (L.K.) measured photoexcitation and (time-resolved) photoluminescence spectra. A.S. and V.D. supervised the research project. N.B., S.W. and A.S. evaluated the data.

[1]Experimental Physics VI, Julius Maximilian University of Würzburg, 97074 Würzburg, Germany

[2]Department of Polymer Chemistry and Technology at Kaunas University of Technology, Radvilenu pl. 19, LT-50254 Kaunas, Lithuania

6 Taking OLEDs for a Spin — is Light Generation in TADF OLEDs Spin-Dependent?[1]

Abstract

Organic light emitting diodes (OLEDs) based on thermally activated delayed fluorescence (TADF) are highly efficient because of the conversion of non-radiative triplet to radiative singlet states by reverse intersystem crossing (RISC). Even efficient TADF OLEDs are, however, limited by long excited state lifetimes, limiting maximum achievable current densities and causing device degradation. On the one hand, thermal activation over singlet-triplet energy gaps that are in the order of tens of millielectronvolts-comparable to thermal energy—could be rate-limiting for the delayed fluorescence process. On the other hand, RISC is a spin-forbidden transition and hence is also expected to be a slow process. To clarify this issue, inherently spin-sensitive and time-resolved methods applied to working OLEDs are necessary. Here, we apply pulsed electrically detected magnetic resonance (pEDMR) to OLEDs based on the donor:acceptor combination m-MTDATA:BPhen. We observe magnetic resonance signals corresponding to emissive exciplex states at the donor:acceptor interface. However, the pEDMR signal does not show any sign of coherent spin manipulation, instead its intensity scales linearly with the energy of applied microwave pulses which excludes the involvement of a coherent spin transition. This implies that TADF is actually not limited by spin-forbidden RISC, but rather by the thermal activation step.

[1] **The results of this chapter are published in**:
N. Bunzmann, D.Baird, H.Malissa, S. Weissenseel, C. Boehme, V. Dyakonov, and A. Sperlich. Thermal activation bottleneck in TADF OLEDs based on m-MTDATA:BPhen (2020). *Preprint on arXiv*

6.1 Introduction

Organic light emitting diodes (OLEDs) based on thermally activated delayed fluorescence (TADF) rely on the upconversion of non-radiative triplet states to radiative singlet states via reverse intersystem crossing (RISC) [10, 11]. One approach to realize TADF is to use proper combinations of donor and acceptor molecules, between which emissive exciplex states form. Due to the extent of this intermolecular excited state, the wave function overlap is small which results in a desirably small singlet-triplet energy gap ΔE_{ST}, that enables RISC at ambient temperatures. While emission from singlet excitons occurs on the order of nanoseconds, TADF is a slow process with time constants in the range of microseconds [10, 11]. This slowness causes issues that hinder the widespread application of TADF OLEDs. Long excited state lifetimes enhance the probability of second order processes, such as triplet-triplet and triplet-polaron annihilation, that limit the device efficiency at current densities relevant for display applications (efficiency roll-off) and are a precursor to degradation [116]. Yet, it is still unclear what the actual rate-limiting process is: the thermal upconversion or the spin-forbidden triplet to singlet RISC. The latter would be a spin-coherent process that depends directly on the initial spin state. In order to investigate this upconversion mechanism, a method with high spin sensitivity and selectivity is crucial. These requirements are met by methods based on electron paramagnetic resonance (EPR), which is a widely used tool in various fields of spin physics research [27]. In the context of TADF, however, only few investigations report on the application of EPR [25, 98, 97]. Recently, we demonstrated the application of photoluminescence, electroluminescence and electrically detected magnetic resonance (PLDMR, ELDMR, EDMR) on donor:acceptor based TADF OLEDs [102]. We were able to determine that the intermediate spin states that are involved in the light generation of the investigated TADF materials are different for optical and electrical excitation. However, to further address the question whether spin-coherent processes are involved in TADF, the method needs to be time resolved. An unambiguous interpretation of continuous wave (cw) magnetic resonance experiments is not always feasible since different spin- and time-dependent processes may result in indistinguishable spectra [117]. To overcome these limitations, the method of pulsed EDMR (pEDMR) can be applied as it combines the advantages of spin selectivity by coherent spin manipulation, time resolution and direct connection between the probed spin species and the optoelectronic properties of devices under test [118, 117, 87]. It has previously been applied to a variety of systems such as silicon thin films [119, 120, 121], organic solar cells [122] as well as polymer-based OLEDs [123, 83, 124]. In those examples the potential of pEDMR to reveal compre-

hensive information about spin dependent recombination and transport mechanisms was successfully demonstrated. Using pEDMR on first-generation polymer-based singlet emitter OLEDs (that are limited by spin-dependent recombination), coherent spin manipulation of charge carriers in the OLED device leads to observable current and EL changes [123, 125, 126]. Here, we apply pEDMR to TADF OLEDs for the first time in order to further elucidate the spin dependence of triplet harvesting via RISC.

6.2 Materials and Devices

In this work, we investigated exciplex-based TADF OLEDs using 4,4',4"-Tris[phenyl(m-tolyl)amino]triphenylamine (m-MTDATA) as a donor and 4,7 Diphenyl-1,10-phenanthroline (BPhen) as an acceptor. The molecular structures and the used sample architecture are shown in **Figure 6.1**.

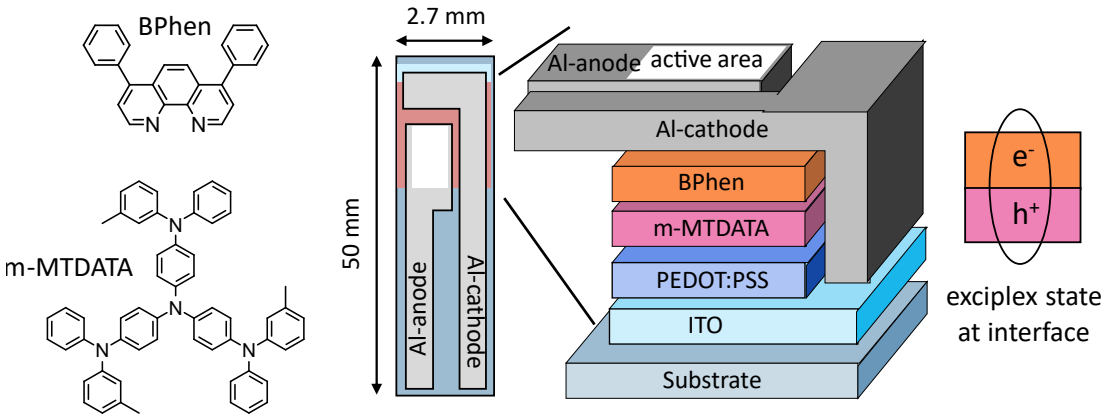

Figure 6.1: Left: Molecular structures of BPhen and m-MTDATA. **Right**: OLED architecture and layer stack.

The sample geometry is optimized for magnetic resonance measurements in an X-band EPR setup which requires the width of samples to be limited to 2.7 mm. The active area (marked in white in **Figure 6.1**) in this layout is defined by the overlap of ITO and the aluminum-cathode which is around 5 mm^2. In this area, the layer stack is given by ITO (120 nm) / PEDOT:PSS (40 nm) / m MTDATA (30 nm) / BPhen (40 nm) / Ca (5 nm) / Al (120 nm). PEDOT:PSS is spin-coated from aqueous solution and m-MTDATA from chlorobenzene. BPhen, Ca and Al were subsequently evaporated on top. Electrons injected from the cathode and holes injected from the anode meet at the interface of m-MTDATA and BPhen to form exciplex states.

The formation of exciplex states is apparent from a comparison of photoluminescence (PL) spectra from pristine m-MTDATA and BPhen films and an EL spectrum from an OLED that is processed as described above. As shown in **Figure 6.2a**, a clear redshift

between the PL spectra and the EL spectrum occurs, demonstrating the formation of exciplex states. The emission layer in such types of OLEDs is therefore given by the two-dimensional interface between m-MTDATA and BPhen.

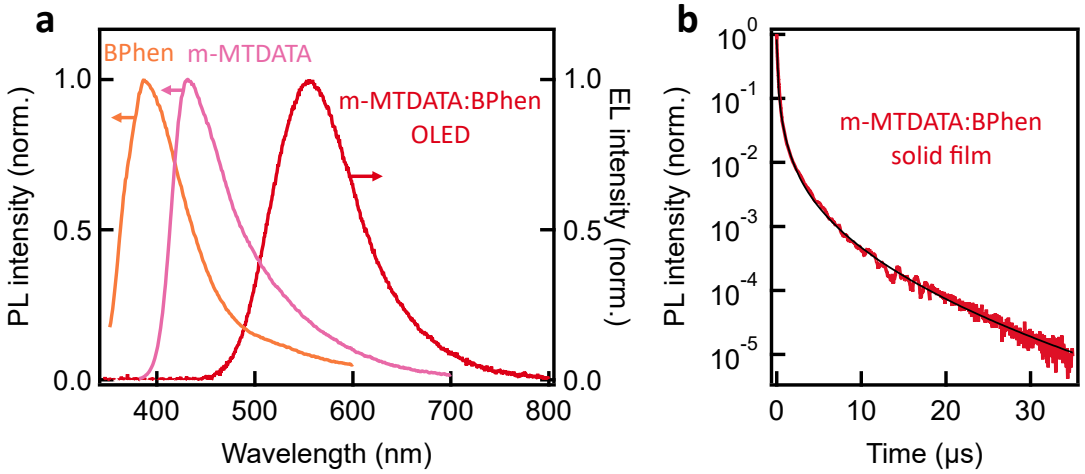

Figure 6.2: a, EL spectrum of an OLED based on m-MTDATA:BPhen and PL spectra of the pristine materials. **b**, Transient PL decay of a blended m-MTDATA:BPhen solid film.

Delayed Fluorescence in this system becomes apparent from time-resolved photoluminescence (trPL) measurements on m-MTDATA:BPhen mixed solid films, where a delayed component in the µs range can be identified (see **Figure 6.2b**). This delayed component was previously assigned to thermally activated RISC [127, 102]. The formation of an exciplex state enables a small singlet-triplet gap ΔE_{ST} of a few tens of millielectronvolts and therefore efficient triplet harvesting.

Figure 6.3 shows a comparison of a pEDMR and a cwELDMR spectrum.

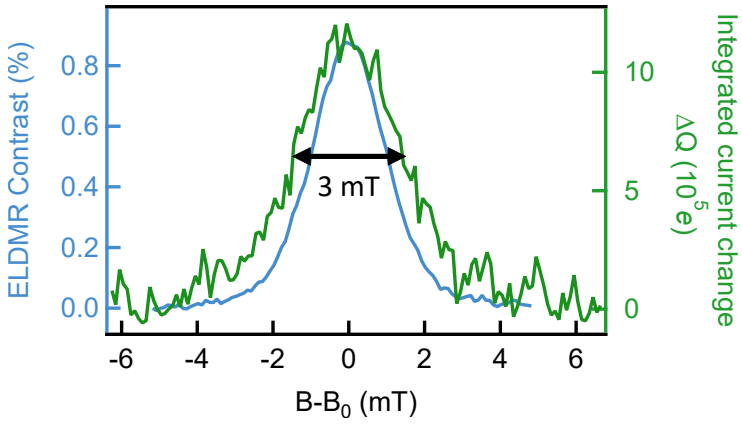

Figure 6.3: Comparison of cwELDMR and pEDMR OLED spectra measured at RT. The magnetic field axis is shifted, such that resonance peaks at $B=B_0$ are centered around $B-B_0$. Both methods yield a Gaussian shaped signal which is assigned to the exciplex triplet ^{3}Exc.

As discussed in detail in **Chapter 5** of this thesis (and in [102]), signals originating from exciplex triplets ^{3}Exc can be observed with spin-sensitive optical detection of PL (PLDMR), as well as by EL or current detection (ELDMR, EDMR) of a fully processed OLED under magnetic resonance conditions. The close similarity of a pEDMR and a cwELDMR spectrum demonstrates that also time-resolved, pulsed magnetic resonance methods can be used to probe this same exciplex spin species. The emergence of this signal will be explained in the following.

6.3 pEDMR Experiments - Theory

EDMR measurements in this chapter deviate from what is explained in the Experimental Section of this thesis. **Figure 6.4** shows the basic components of the used pEDMR setup which is based on a *Bruker E580* EPR spectrometer.

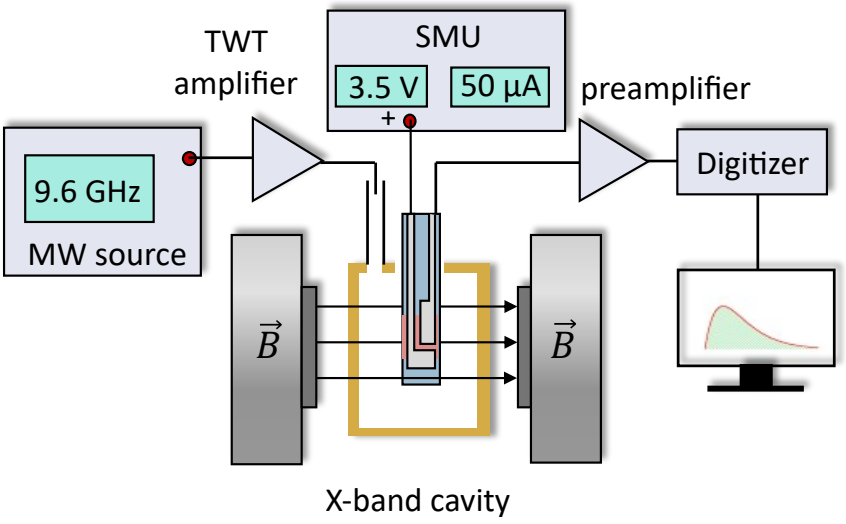

Figure 6.4: Schematic illustration of the used pEDMR setup.

An OLED is inserted into an X band cavity (*Bruker ER 4118 X-MD5*) inside an electromagnet that creates an external magnetic field B. MW pulses are generated by the E580 MW bridge with an adjustable attenuator that allows to vary the pulse power. The pulses are amplified by a traveling wave tube (TWT) amplifier with maximum output power of 1 kW before being directed to the cavity. The MW frequency of the pulses is resonant with the dimensions of the cavity and in the range of 9.6 GHz. The OLED is electrically driven by a source-measure-unit (SMU) at around 4.5 V and a current density of around 1 mA/cm^2. MW induced changes of the current ΔI through the OLED are pre-amplified by a current-voltage transimpedance amplifier (*Stanford Research SR570*) and detected by the built-in transient recorder of the E580. During a pEDMR

experiment, MW pulses of defined length and power are applied to the OLED, while it is driven by a current I. Resonant microwaves drive transitions between triplet sublevels. The coherent altering of triplet populations affects recombination and transport mechanisms causing a time-dependent current change ΔI [128, 129, 130]. For all measurements, the time axis starts with the rise of the MW pulse.

Figure 6.5 shows an illustration of the detection and evaluation scheme in pEDMR experiments.

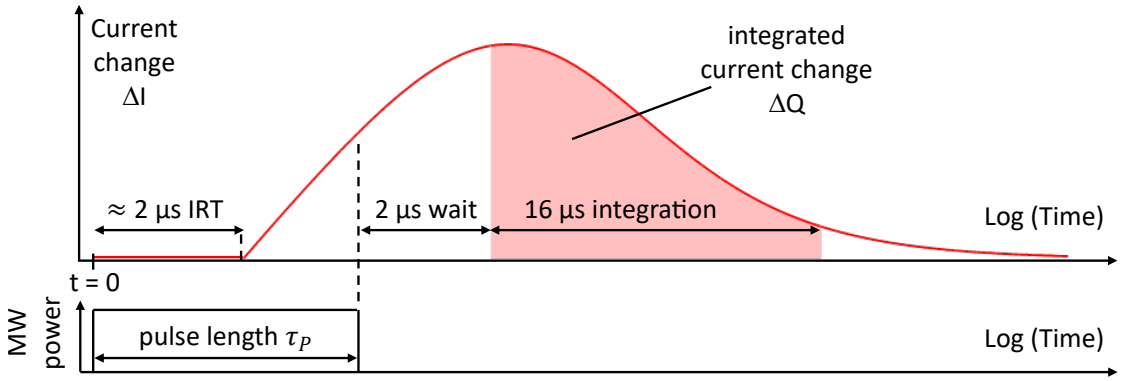

Figure 6.5: Illustration of the detection and evaluation scheme in pEDMR experiments: A MW pulse of length τ_P is applied to an OLED under test while the resulting current change ΔI is recorded. The rise of the MW pulse triggers the start of data acquisition (t=0). The instrument response time (IRT) delays the signal rise by around 2 μs. In general, the start of a detectable signal and the duration of the MW pulse can overlap. In order to make the integrated current change ΔQ comparable for different pulse lengths, the integration was chosen as a 16 μs window starting 2 μs after the end of the MW pulse.

A MW pulse of length τ_P is applied to an OLED under test while the resulting current change ΔI is recorded. The rise of the MW pulse triggers the start of data acquisition (t = 0). The instrument response time (IRT) delays the signal rise by around 2 μs. In general, the start of a detectable signal and the duration of the MW pulse can overlap. In order to quantify the amplitude of pEDMR for each transient, it is convenient to integrate ΔI over time, yielding a charge ΔQ [118]. To then make ΔQ comparable for different pulse lengths, an integration window of 16 μs was chosen, starting 2 μs after the end of the MW pulse. Those time limits reasonably take the IRT and signal lifetime of each transient into account.

6.4 pEDMR Experiments - Results

First, we measured pEDMR using a pulse length of $\tau_P = 4$ μs and a power attenuation of 9 dB. **Figure 6.6a** shows a current change transient at resonant magnetic field at 344 mT.

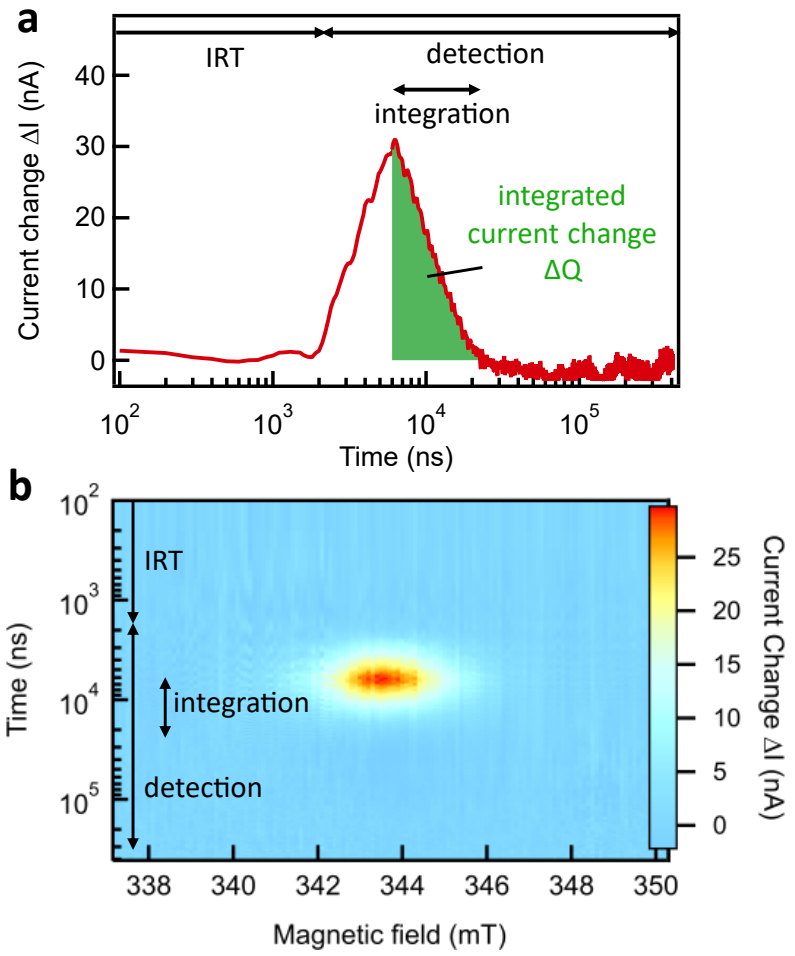

Figure 6.6: a, Current change transient for an m-MTDATA:BPhen OLED. Transient recording starts with the rise of the MW pulse. The instrument response time (IRT) delays signal detection for around 2 μs. An integration window of 16 μs starts 2 μs after the MW pulse ends, yielding the integrated current change ΔQ. **b**, 2D plot of current change transients at different magnetic fields.

The observation of a current change is delayed for 2 μs after rising edge of the MW pulse which is due to the instrument response time (IRT). Subsequently, the signal rises and reaches a maximum at around t = 10 μs. The decay back to zero is finished at around 30 µs. **Figure 6.6b** shows an entire 2D map of ΔI transients within the used magnetic field range.

Determining ΔQ according to **Figure 6.5** for all transients at each magnetic field yields the pEDMR spectrum shown in **Figure 6.3**. The shape of this curve is identi-

cal to the exciplex signal detected by cwELDMR except for a slightly broader linewidth caused by MW power broadening.

Before coherent pEDMR experiments can be performed, proper calibration of MW pulse length and power is essential. To adjust the pulses with respect to the spin flip time between the involved Zeeman sublevels, we used pulsed EPR on the known spin reference sample BDPA [131, 132]. A tiny amount of BDPA was mounted on top of the OLED to ensure identical experimental conditions for both pEPR and pEDMR. The observed Rabi oscillations of the BDPA spin-1/2 system are shown in **Figure 6.7** for 9 dB MW attenuation.

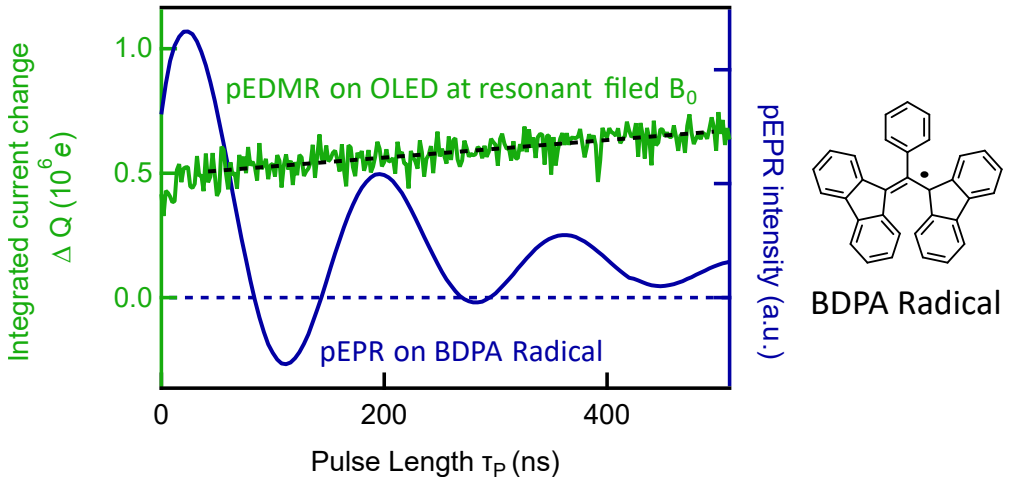

Figure 6.7: Blue trace: pEPR of a BDPA spin reference sample (molecular structure next to the graph) demonstrating Rabi oscillations. **Green trace**: ΔQ as a function of the MW pulse length τ_P at resonant magnetic field B_0 for an OLED under identical conditions as for pEPR. The black dashed line is a guide for the eye. A linear signal rise instead of Rabi oscillations can be observed.

The fitting of this trace to an exponentially decaying sine wave allows the estimation of the duration for a π-pulse to 85 ns and the microwave magnetic field B_1 = 0.21 mT. The oscillations decay with a time constant of 144 ns that is limited by the spectrometer and the spin-spin coherence time T_2^*, in line with literature values [133].

Now that we have calibrated the spectrometer and established that pEDMR is a suitable method to detect exciplex triplets in working OLEDs, we can look for the coherence properties of the involved spin system. The most straight-forward experiment is to search for Rabi oscillations of the exciplex signal. In this experiment, the integrated current change ΔQ in resonance is recorded as a function of the applied MW pulse length τ_P. Such experiments have previously been successfully performed on singlet emitter OLEDs based on derivatives of the polymer poly(p-phenylene vinylene) (PPV) using this particular pEDMR setup [123, 83, 124]. Remarkably, the pEDMR ΔQ trace

in **Figure 6.7** does not contain any sign of Rabi oscillations. Instead, after an initial instrument-related offset, ΔQ follows a linearly rising trend; i.e. being proportional to the length of the MW pulse.

To further explore this effect and corroborate that this is not an experimental artefact, we performed a series of experiments with varying pulse length and MW power as shown in **Figure 6.8a**, **b**.

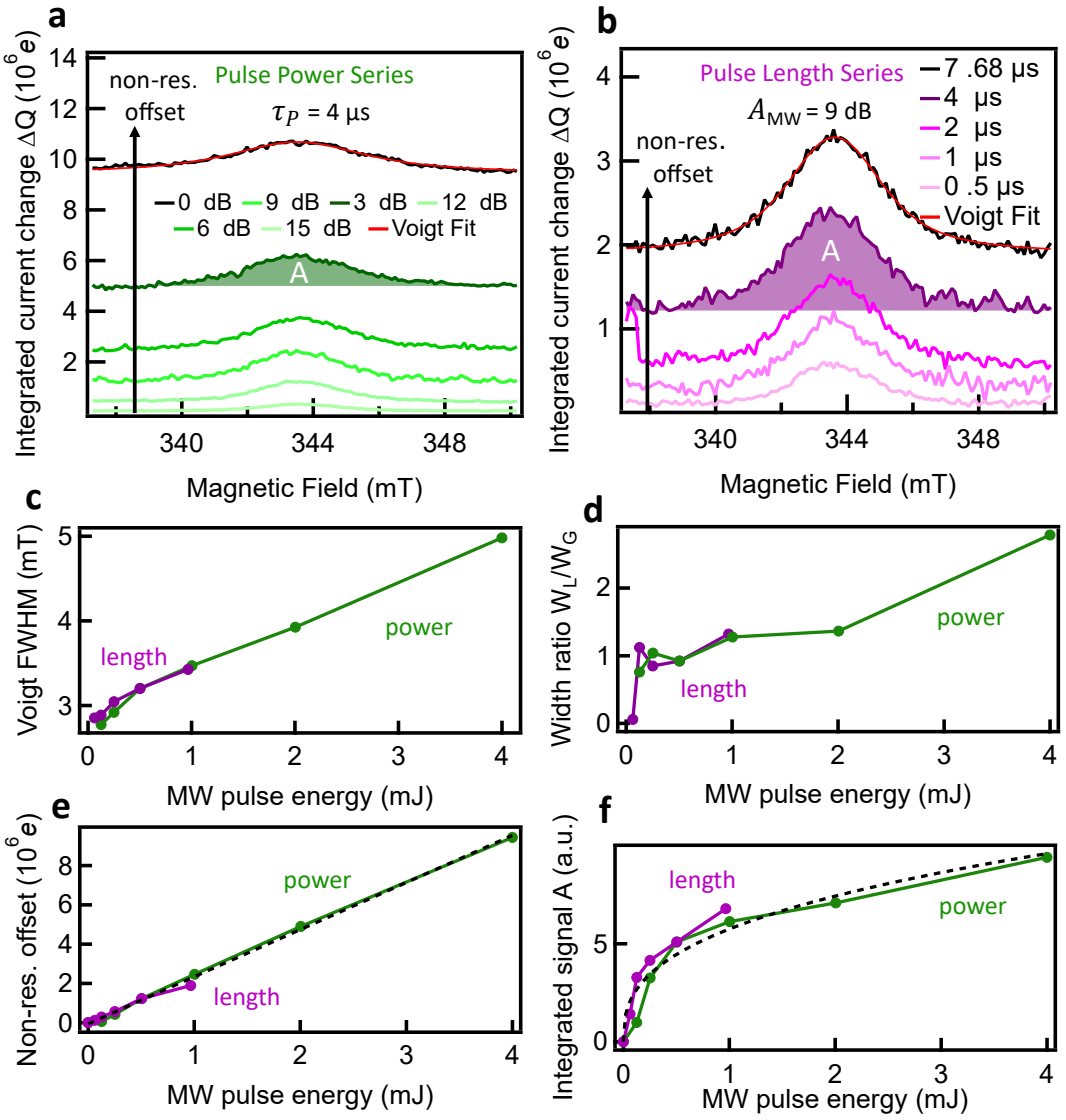

Figure 6.8: Pulse power (green) and pulse length (purple) dependent pEDMR experiments. ΔQ as a function of the magnetic field B for (**a**) different MW pulse attenuation (pulse length fixed at $\tau_P = 4\ \mu s$) and (**b**) for different pulse lengths (attenuation $A_{MW} = 9$ dB). All spectra are fitted with a Voigt profile (red). The fit parameters are plotted versus the MW pulse energy (pulse power × length). **c**, Voigt linewidth FWHM increase representing power broadening. **d**, Ratio of the width of the Lorentzian contribution W_L and the Gaussian contribution W_G. **e**, Non-resonant offset. **f**, Integrated signal A. Dashed black traces represent guides to the eye.

We observe, that both the non-resonant offset and the Voigt-shaped exciplex signal increase monotonically with increasing pulse energy (power × length). The linear increase of the non-resonant offset (**Figure 6.8e**) can be explained by sample heating due to MW electrical stray fields. Charge transport in organic semiconductor devices is a temperature-activated hopping transport. The observation of a linear current increase for an OLED operated at constant voltage is thus to be expected for Joule heating of the device.

The increase of the resonance signal with pulse energy is more complex as MW power broadening is involved [131]. At low power, the signal has a Gaussian lineshape as evident by the cwELDMR spectrum plotted in **Figure 6.3**, that has been recorded with approximately an order of magnitude lower MW magnetic field strength B_1 than the lowest-power pEDMR spectrum. At high MW power, however, the shape becomes Lorentzian. Voigt fits show this transition from Gaussian to Lorentzian lineshape (**Figure 6.8d**), as well as a doubling of the FWHM linewidth (**Figure 6.8c**) for the tested MW pulse energy range.

The integrated signal A is plotted in **Figure 6.8f** demonstrating monotonic, slightly saturating signal increase. This observation indicates saturation of the EPR transitions between the exciplex triplet sublevels.

The fact that signal parameters in **Figure 6.8** directly depend on pulse energy, regardless of whether pulse power or length were changed, demonstrates that we are not dealing with an experimental artifact. The pEDMR current changes do indeed not involve a spin-coherent process and thus do not display Rabi oscillations as shown in **Figure 6.7**.

6.5 Discussion

To put the observation of (non-)resonant heating and lack of coherent spin manipulation into context, we use our observations to extend the generally accepted model of TADF OLEDs [11, 10, 102] as illustrated in **Figure 6.9a**.

Singlet and triplet excitons localized on the separate donor and acceptor molecules are not involved as these are energetically much higher than the exciplex states [134, 102], which are the only states accessible for an electrically driven OLED. Losses by non-radiative decay from ^{1}Exc and ^{3}Exc states are omitted for simplicity. First, free charges recombine at the donor:acceptor interface into exciplex states with a 75:25 triplet to singlet ratio. Singlet exciplexes ^{1}Exc decay as prompt fluorescence (PF) with sub-µs rate constant k_F. Triplet exciplexes ^{3}Exc from a low vibrational excited state v_0 need to get thermally excited to a higher vibrational state v_i with rate k_{TA} [33].

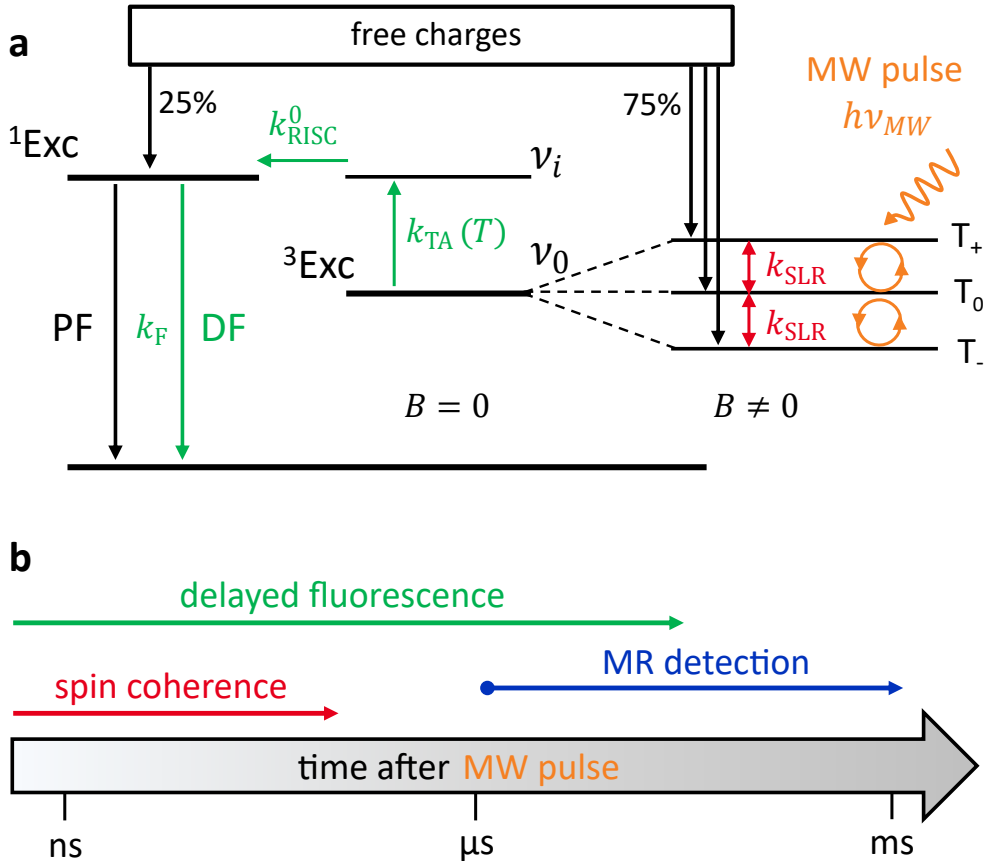

Figure 6.9: Spin coherence and TADF time constants in comparison. **a**, Energy diagram illustrating the steps involved for TADF. Free charge carriers recombine at the donor:acceptor interface to triplet and singlet exciplex states (^{3}Exc, ^{1}Exc). Singlets recombine radiatively emitting prompt fluorescence (PF) with rate k_F. ^{3}Exc triplets are thermally activated (k_{TA}) to a higher vibrational state ($\nu_0 \rightarrow \nu_i$) that is isoenergetic with ^{1}Exc to enable efficient RISC (k^0_{RISC}), followed by delayed fluorescence (DF). In an external magnetic field (B≠0), ^{3}Exc Zeeman sublevels (T$_+$, T$_0$, T$_-$) are energetically split. Between them, resonant microwave pulses $h\nu_{MW}$ can drive coherent population oscillations that are dampened by spin lattice relaxation (k_{SLR}). **b**, Depiction of involved time scales. DF is observed over several μs, while magnetic resonance is detected from 2 μs onwards. Coherent spin manipulation and SLR take place on the timescale of hundreds of ns. The combined rates of k_{TA} and k^0_{TA} lead to a μs TADF time constant that enables equalization of ^{3}Exc spin polarization by k_{SLR}.

If the higher vibrational state is approximately isoenergetic with ^{1}Exc, RISC takes place with rate k^0_{RISC} resulting in delayed fluorescence (DF) that can last over several microseconds.

If an external magnetic field B is applied, ^{3}Exc states are energetically split into Zeeman sublevels T$_+$, T$_0$, and T$_-$. Resonant microwave pulses can drive transitions between the sublevels, leading to coherent population oscillations as demonstrated by Rabi oscillations of BDPA radicals in **Figure 6.7**. Spin lattice relaxation k_{SLR} drives the

triplet population back to thermal equilibrium and causes decoherence on a timescale of hundreds of ns. The following slow thermal activation and RISC finally prevent coherent spin manipulation between triplet sublevels from affecting the observed rate of DF or the pEDMR current. Any coherent spin manipulation is 'averaged out' by slow TADF processes, similar to a low-pass frequency filter. Even zero IRT would thus not change this outcome. As a consequence, resonant microwaves only cause non-coherent Joule heating of the OLED which lowers the material's electrical resistance and is observed as a current increase for pEDMR. A summary of the involved time scales is shown in **Figure 6.9b**.

The temperature increase of the OLED under test can actually be estimated. **Figure 6.10a** shows temperature-dependent current density j versus voltage V characteristics for an OLED based on m-MTDATA:BPhen.

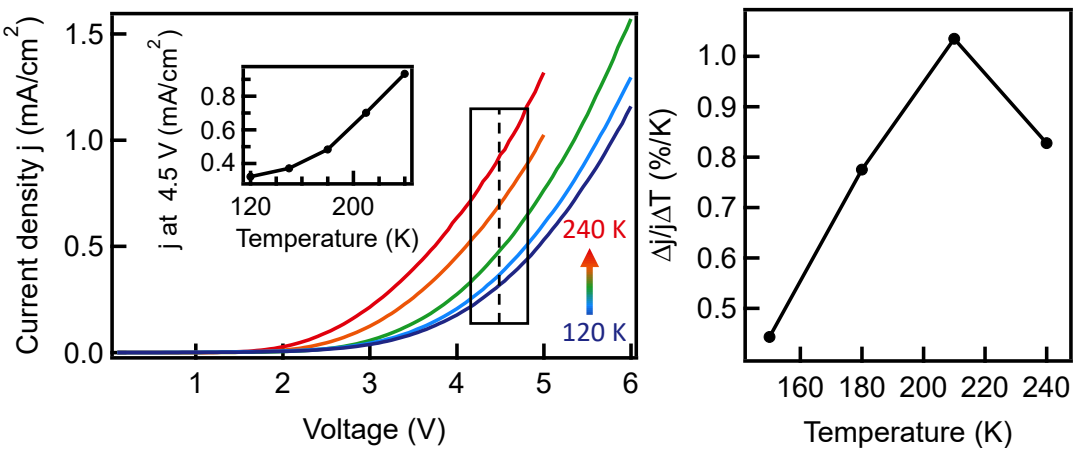

Figure 6.10: a, Temperature-dependent current density j versus voltage V characteristics for an OLED based on m-MTDATA:BPhen. Inset: Current density j at 4.5 V for each temperature. **b**, $\frac{\Delta j}{j\Delta T}$ calculated with the data points from (a). A temperature change ΔT of 1K results in a relative current change of 0.5-1%

The current density increases with increasing temperature, as expected from temperature-activated hopping in organic materials and from TADF. The inset of **Figure 6.10a** shows the current density at 4.5 V for each temperature. From those data points, the quantity $\frac{\Delta j}{j\Delta T}$ can be calculated according to $\frac{\Delta j}{j\Delta T}(T_i) = \frac{j_{i+1} - j_i}{j_i \cdot (T_{i+1} - T_i)}$, which is shown in **Figure 6.10b**. A temperature change ΔT of 1K results in a relative current change of 0.5-1%. The maximum pEDMR-detected current change Δ I in **Figure 6.6** is around 30 nA. With a total current of I=50 μA, the relative current change in resonance is 0.06%. Those numbers allow the estimation of the OLED's temperature increase of around 0.06 K in resonance.

We want to point out that the described spin resonance experiments are on an actual 2D interface between donor and acceptor materials. This is a rare opportunity to study spins confined to a 2D system, which usually inhibits the use of any standard EPR methods due to the low overall spin number. The superior sensitivity of EDMR is the key to this kind of experimental approach.

6.6 Conclusion

We set out to address the question which the actual rate-limiting process in TADF donor:acceptor OLEDs is: thermal activation or spin-forbidden conversion of non-emissive triplet to emissive singlet exciplex states. To investigate this problem, we applied the intrinsically spin-sensitive and spin-coherent experimental method of pulsed electrically detected magnetic resonance (pEDMR) to working OLEDs under realistic working conditions. The application of resonant microwave (MW) pulses induces a Voigt-shaped pEDMR signal, which is assigned to exciplex triplet states. pEDMR detected Rabi oscillations are however not observed which leads us to the conclusion that the time constant of thermal activation of triplets in the RISC process is too long for coherent spin manipulation to be translated to a change of the delayed fluorescence rate. Instead, spin lattice relaxation causes decoherence of spins before the thermal activation takes place. Furthermore, a comparison of the dependence of microwave pulse length and pulse power on the pEDMR signal points out that its intensity is solely related to the energy that is deposited per MW pulse. We therefore conclude that the observed signals are induced by resonant heating: microwave photons absorbed by triplet exciplexes or by the OLED device itself lead to a slight temperature increase of around 0.06 K that results in a detectable change in current and electroluminescence intensity. Overall, our results reveal that RISC in donor:acceptor based TADF OLEDs is not influenced by coherent spin-effects because the time constant of delayed fluorescence is at least an order of magnitude longer than the involved spin coherence times. Upcoming, more efficient TADF emitters with shorter excited state lifetimes might however enter a regime, where spin effects become rate limiting for OLED operation.

6.7 Contributions to this Chapter

Andreas Sperlich[1] (A.S.), Hans Malissa[2] (H.M.) and Vladimir Dyakonov[1] (V.D.) designed the experiments. Nikolai Bunzmann[1] (N.B.) and Sebastian Weißenseel[1] prepared the devices. N.B., S.W. and A.S. carried out electro-optical device characterization. A.S., Douglas L. Baird (D.L.B.)[2] and H.M. performed the magnetic resonance measurements. A.S., Christoph Boehme[2] (C.B.) and V.D. supervised the research project. N.B. and A.S. evaluated the data.

[1]Experimental Physics VI, Julius Maximilian University of Würzburg, 97074 Würzburg, Germany

[2]Department of Physics and Astronomy, University of Utah, Salt Lake City, Utah 84112, USA

7 Spin- and Voltage-Dependent Emission from Intra- and Intermolecular TADF OLEDs[1]

Abstract

Organic light emitting diodes (OLEDs) based on thermally activated delayed fluorescence (TADF) utilize molecular systems with a small energy splitting between singlet and triplet states. This can either be realized in intramolecular charge transfer states of molecules with near-orthogonal donor and acceptor moieties or in intermolecular exciplex states formed between a suitable combination of individual donor and acceptor materials. Here, we investigate pCNBCzoCF$_3$, which shows intramolecular TADF but simultaneously can form exciplex states in combination with m-MTDATA. The drawback of all-optical methods and electro-optical device characterization is their lack of sensitivity for the spin degree of freedom. In this work, we use electroluminescence detected magnetic resonance (ELDMR) on operational devices to study the thermally activated spin-dependent triplet to singlet up-conversion. Thereby, we can investigate intermediate excited states involved in OLED operation and derive the corresponding activation energy for both, intra- and intermolecular based TADF. Furthermore, we can give a lower estimate for the extent of the triplet wave function to be ≥1.2 nm. Photoluminescence detected magnetic resonance (PLDMR) reveals the population of molecular triplets in optically excited thin films. Overall, our findings allow us to draw a comprehensive picture of the spin-dependent emission from intra- and intermolecular TADF OLEDs.

[1] **The results of this chapter are published in**:
N. Bunzmann, B.Krugmann, S. Weissenseel, L. Kudriashova, K. Ivaniuk, P. Stakhira, V. Cherpak, M. Chapran, G. Grybauskaite-Kaminskiene, J. V. Grazulevicius, V. Dyakonov and A. Sperlich. Spin- and Voltage-dependent emission from Intra- and Intermolecular TADF OLEDs. *Advanced Electronic Materials*, aelm.202000702R1 (2020)

7.1 Introduction

Organic light emitting diodes (OLEDs) represent a promising alternative to conventional LEDs for flat panel display applications and room lighting. One of the major challenges in the development of OLED technologies has been the improvement of efficiencies since only 25% of injected charge carriers form emissive singlet states while 75% form non-radiative triplet states [43, 44, 30]. However, thermally activated delayed fluorescence (TADF) can be induced if molecules exhibit a small energy splitting ΔE_{ST} between singlet and triplet state [90, 11, 10]. An enhanced reverse intersystem crossing (RISC) enables harvesting of triplets thus dramatically increases the efficiency of TADF based devices.

ΔE_{ST} is predominantly determined by the orbital overlap between the highest occupied molecular orbital (HOMO) and the lowest unoccupied molecular orbital (LUMO) of organic molecules [90]. Therefore, the strategy to achieve small ΔE_{ST} is to design molecules that possess a spatially separated HOMO and LUMO. This requirement has either been achieved in molecules with twisted donor and acceptor moieties forming intramolecular charge transfer (CT) states [11, 135, 12] or in suitable combinations of separate donor and acceptor molecules forming intermolecular exciplex states [10, 91, 92]. Both of these approaches have been implemented successfully and high external quantum efficiencies (EQE) in the range of 20% have been demonstrated [12, 136].

One of the remaining challenges is to tune the emission color of the used molecules for the desired application, while maintaining high efficiency. An advantage of OLEDs for lighting applications is their surface-emission characteristic since conventional LEDs emit as potentially glaring point sources. Consequently, it is desirable to build efficient OLEDs that produce warm white light. The corresponding broad emission spectrum is often realized by blending the spectra of two single complementary emitters. One approach is the combination of a blue and an orange light source, which has been realized by a blue fluorescent and an orange phosphorescent emitter [137, 138]. However, progress has also been made in producing white light based on TADF emitters [139, 140]. One of these approaches is based on the molecule 4,4'- (9H,9'H- [3,3'-bicarbazole]-9,9'-diyl) bis (3-(trifluoromethyl) benzonitrile) (pCNBCzoCF$_3$) [140]. It forms intramolecular CT states which exhibit sky-blue emission but additionally can form intermolecular exciplex states in combination with 4,4',4"-Tris [phenyl(m-tolyl)-amino] triphenylamine (m-MTDATA), which results in orange emission. A device combining both of these characteristics showed warm white emission color with a high efficiency of 17.0% EQE [140].

Meanwhile, it is still an important point of discussion how the spin degree of freedom influences the first order forbidden RISC rate in operational TADF OLEDs. The combination of both intra- and intermolecular TADF makes pCNBCzoCF$_3$ an interesting model system to apply inherently spin sensitive methods to. Such methods have just recently been applied for the first time to donor:acceptor based intermolecular TADF OLEDs [98, 102], but not yet to intramolecular emitters or their combination. In this study, we investigate the TADF characteristics of the building blocks of warm white OLEDs based on the intramolecular CT emission from pristine pCNBCzoCF$_3$ and devices based on emission from exciplex states formed between pCNBCzoCF$_3$ and m-MTDATA. Moreover, we elucidate properties of the involved triplet states that are involved in the RISC mechanism for both device types by using electroluminescence detected magnetic resonance (ELDMR) for electrical generation and photoluminescence detected magnetic resonance (PLDMR) for optical excitation.

7.2 Materials and Devices

Figure 7.1 shows the molecules used in this work. pCNBCzoCF$_3$ and m-MTDATA are used for the emissive layers while TCTA and BCP are used as transport layers.

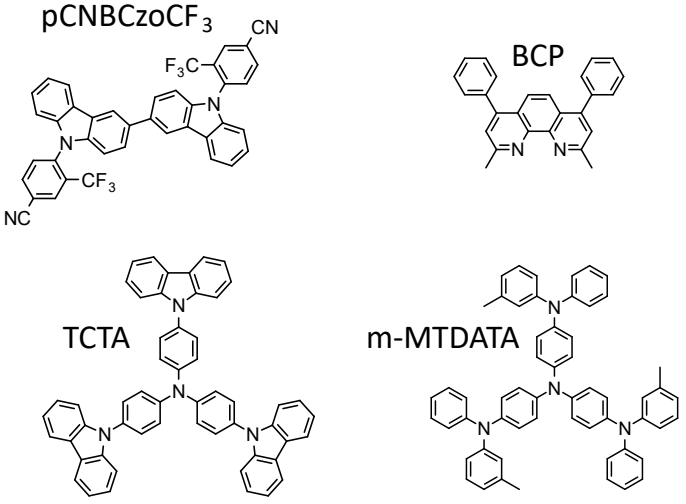

Figure 7.1: Molecular structures of materials used in this work.

Figure 7.2a displays the device structure of OLEDs used in this work. ITO was used as an anode for all devices and Ca/Al as a cathode. PEDOT:PSS and BCP were used as hole and electron transport layers, respectively. Two types of devices were built with different choice of materials for the emissive layer. The first device type is based on TCTA and pCNBCzoCF$_3$ in the emissive layer (left part of **Figure 7.2a**). In this case,

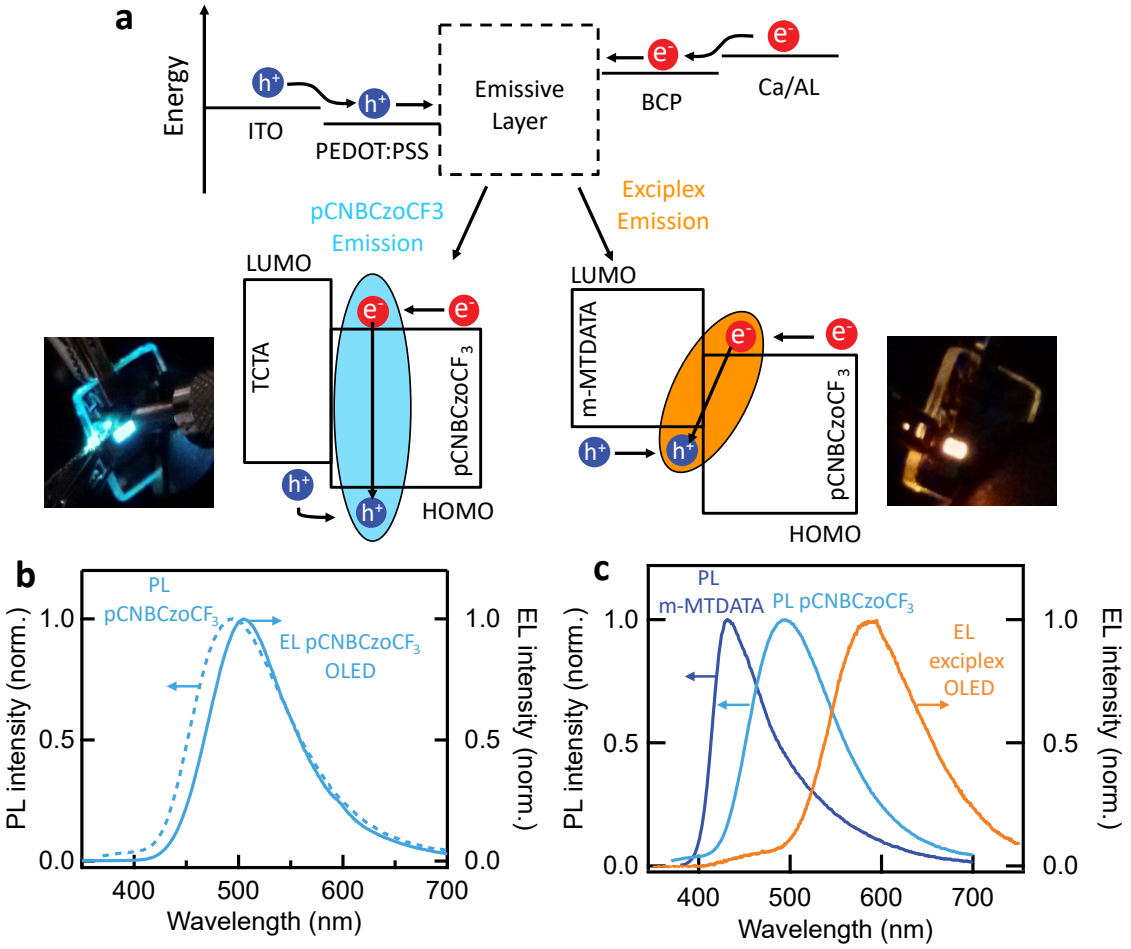

Figure 7.2: a, Device structure and energy diagram of investigated OLEDs. Two different emissive layer combinations were used. For TCTA:pCNBCzoCF$_3$ there is no exciplex formation and emission originates from excitons on pCNBCzoCF$_3$ (left). For m-MTDATA:pCNBCzoCF$_3$ emission originates from exciplex states at the interface (right). Photographs show the respective device under test. **b**, PL spectrum of a pristine pCNBCzoCF$_3$ film and an EL spectrum of a pCNBCzoCF$_3$-based OLED. **c**, PL spectra of pristine m-MTDATA and pristine pCNBCzoCF$_3$ films together with an EL spectrum of an m-MTDATA:pCNBCzoCF$_3$-based OLED.

excitons form on pCNBCzoCF$_3$ giving rise to sky-blue emission, as shown in the corresponding EL spectrum (**Figure 7.2b**). The PL spectrum of a pCNBCzoCF$_3$ film and the EL from an pCNBCzoCF$_3$-based OLED differ only slightly. This shows that there is no exciplex formation between TCTA and pCNBCzoCF$_3$ as well as no emission from pristine TCTA. Therefore, TCTA solely functions as a transport and blocking layer, but does not contribute to the emission.

The second device type relies on m-MTDATA and pCNBCzoCF$_3$ in the emissive layer (right part of **Figure 7.2a**). Here, a clear redshift between the EL spectrum of the device and the PL spectrum of pristine pCNBCzoCF$_3$ and pristine m-MTDATA is

observed (**Figure 7.2c**). This proves the formation of an exciplex state which gives rise to orange emission. There is a shoulder at 420-500 nm that can be assigned to additional emission from pristine pCNBCzoCF$_3$. Here, holes overcome the energetic barrier at the m-MTDATA:pCNBCzoCF$_3$ interface and form excitons with electrons in the pCNBCzoCF$_3$ layer, giving rise to the observed shoulder in the EL spectrum. This effect, however, does not necessarily need to be considered a deficiency since the use of an intramolecular TADF emitter as one of the constituents for an exciplex emitter can be beneficial for device efficiency [136]. In such a case, triplets can undergo RISC on a TADF molecule, whereas they can be lost due to non-radiative decay if they form on a conventional emitter molecule. As a result, a potential loss channel is averted. With a combination of the sky-blue emission of pristine pCNBCzoCF$_3$ and the orange emission of the exciplex, a warm white OLED can be realized, as successfully demonstrated in [140].

The intensity of pCNBCzoCF$_3$ emission at the shoulder of the EL spectrum of exciplex-based OLEDs increases with increased driving voltage as shown in **Figure 7.3a**.

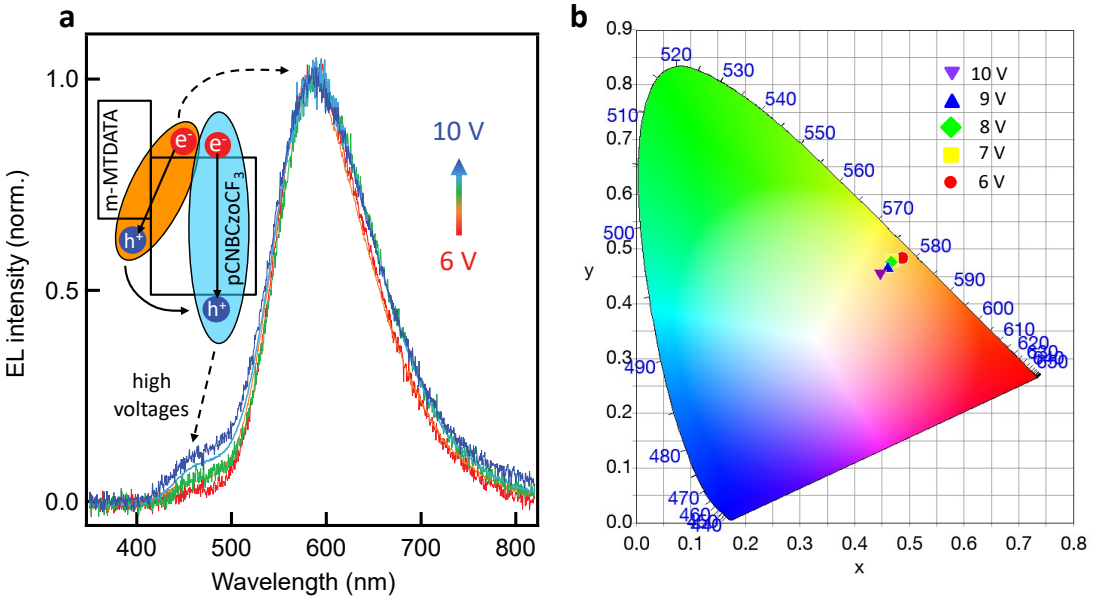

Figure 7.3: a, Voltage-dependent EL spectra of m-MTDATA:pCNBCzoCF$_3$-based OLEDs. The main peak originates from exciplex emission. An additional shoulder at around 450 nm increases with increasing voltage. This can explained by holes overcoming the energetic barrier at the m-MTDATA:pCNBCzoCF$_3$ interface, which leads to the formation of excitons on pCNBCzoCF$_3$. **b**, CIE1931 color diagram including the positions of voltage-dependent EL spectra from **a**.

Figure 7.3b shows the position of EL spectra from an exciplex-based OLED in a CIE1931 color diagram (as introduced in **Chapter 2**, **Section 2.11**). Between 6 V to 10 V the correlated color temperature (CCT) of the respective EL spectra shifts from 2870 K to

3230 K. A device that is optimized to exhibit emission from both pristine $pCNBCzoCF_3$ and the exciplex state could be used to tune the emission in between warm and cold white by setting different driving voltages. This concept is desirable as modern smartphone displays already employ a change in color temperature (so-called “night shift”) and this is also in demand for future room lighting applications. So far this can only be implemented by incorporating several OLEDs of different color and not within just one device.

7.3 Electroluminescence Detected Magnetic Resonance

Kaminskiene et al. showed the potential of $pCNBCzoCF_3$ for building warm white OLEDs [140]. The focus of their work was to explore the spectral properties and performance characteristics of the corresponding devices. However, a detailed investigation of the TADF characteristics of $pCNBCzoCF_3$ as well as spin sensitive measurements, such as ELDMR, are still missing. These measurements elucidate properties of triplet states that are involved in the light generation mechanisms of the devices, while the temperature dependence reveals the TADF activation energy [98, 102]. **Figure 7.4** shows ELDMR spectra for a $pCNBCzoCF_3$-based OLED and an exciplex-based OLED at a temperature of 245 K.

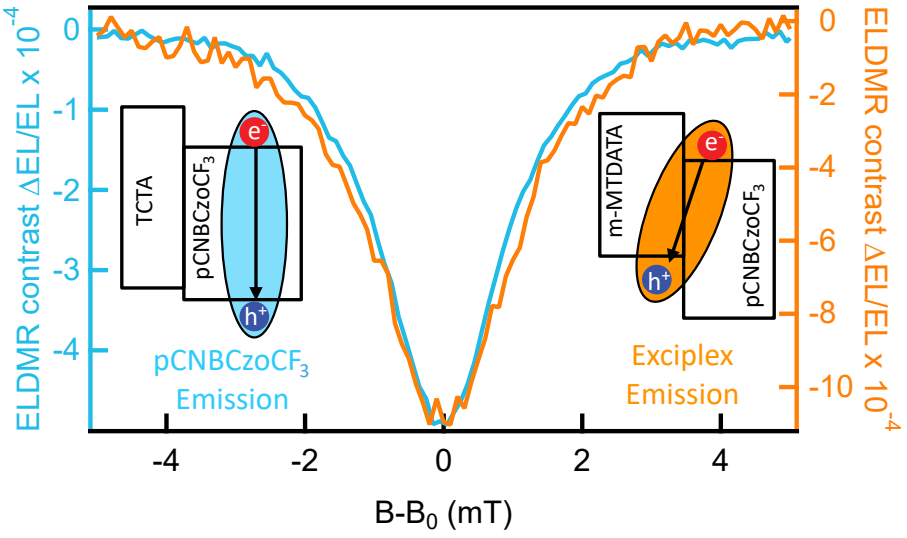

Figure 7.4: ELDMR spectra for a $pCNBCzoCF_3$-based OLED (left axis) and an m-MTDATA:$pCNBCzoCF_3$-based OLED (right axis) at 245 K. The y-axis for both measurements are scaled such that the maxima of both curves coincide. The magnetic field axis is shifted to $B - B_0$, where B_0 is the resonant magnetic field for the respective measurement.

The y-axis for both measurements are scaled such that the maxima of both curves coincide. The magnetic field axis is shifted to $B - B_0$ where B_0 is the resonant magnetic field for the respective measurement (ELDMR measurements were performed according to **Chapter 4**, **Section 4.2** with the use of a stripline as the microwave source). The ELDMR curve for both device types consists of a single, Gaussian shaped line without additional features. The emergence of such a signal was explained in detail in **Chapter 3**, **Section 3.3**. To remind, spin–spin interaction causes a zero-field splitting D of triplet states which lifts the degeneracy of the $T_{\pm}$ and the T_0 triplet sublevels at zero magnetic field. For small D values, EPR absorption lines for the $T_+ \leftrightarrow T_0$ and the $T_0 \leftrightarrow T_-$ transitions overlap. An ELDMR experiment eventually measures the superposition of those two individual overlapping lines. As a result, a single broadened Gaussian shaped signal is observed.

The full width at half maximum (FWHM) can be considered as an upper limit for $2D$. This estimation allows the calculation of a lower boundary for the extent of the triplet wave function, i.e. the distance $r_{e\text{–}h}$ between electron and hole forming the triplet state. The following approximation can be made [73]:

$$r_{e\text{–}h}[\text{nm}] = \sqrt[3]{\frac{2.785}{D[\text{mT}]}}\text{nm} \tag{7.1}$$

Here, one obtains $r_{e\text{–}h}$ in units of nm by using D in units of mT. From the FWHM = 3 mT of the ELDMR spectra shown in **Figure 7.4** one finds $2D \leq 3$ mT resulting in $r_{e\text{–}h} \geq 1.2$ nm. Such numbers fit to delocalized triplet states where the electron–hole distance is large. In contrast, strongly localized molecular triplet excitons, that are being discussed to be involved in TADF emission [24, 26], exhibit distinct broader spectra because of a close electron–hole distance and thus strong dipolar interaction D [76, 102]. Such molecular triplets are, however, not observed in the studied material systems. Consequently, the narrow ELDMR linewidth is consistent with expectations for CT triplet states. For the device based on pure pCNBCzoCF$_3$ emission this corresponds to the ^{3}CT triplet delocalized between the accepting and the donating moieties of pCNBCzoCF$_3$. For the exciplex-based device it corresponds to the ^{3}Exc triplet formed between an electron located on pCNBCzoCF$_3$ and a hole located on m-MTDATA. The striking similarity of the two signals is evidence for almost identical wave function delocalization in both cases: a delocalized triplet is probed that extents over different moieties of a single molecule or even two separate molecules.

In order to investigate the TADF character of both device types, we measured temperature dependent ELDMR spectra (see **Figure 7.5a**, **b**). In both cases the signal shape is temperature-independent, while the ELDMR intensity decreases with decreasing

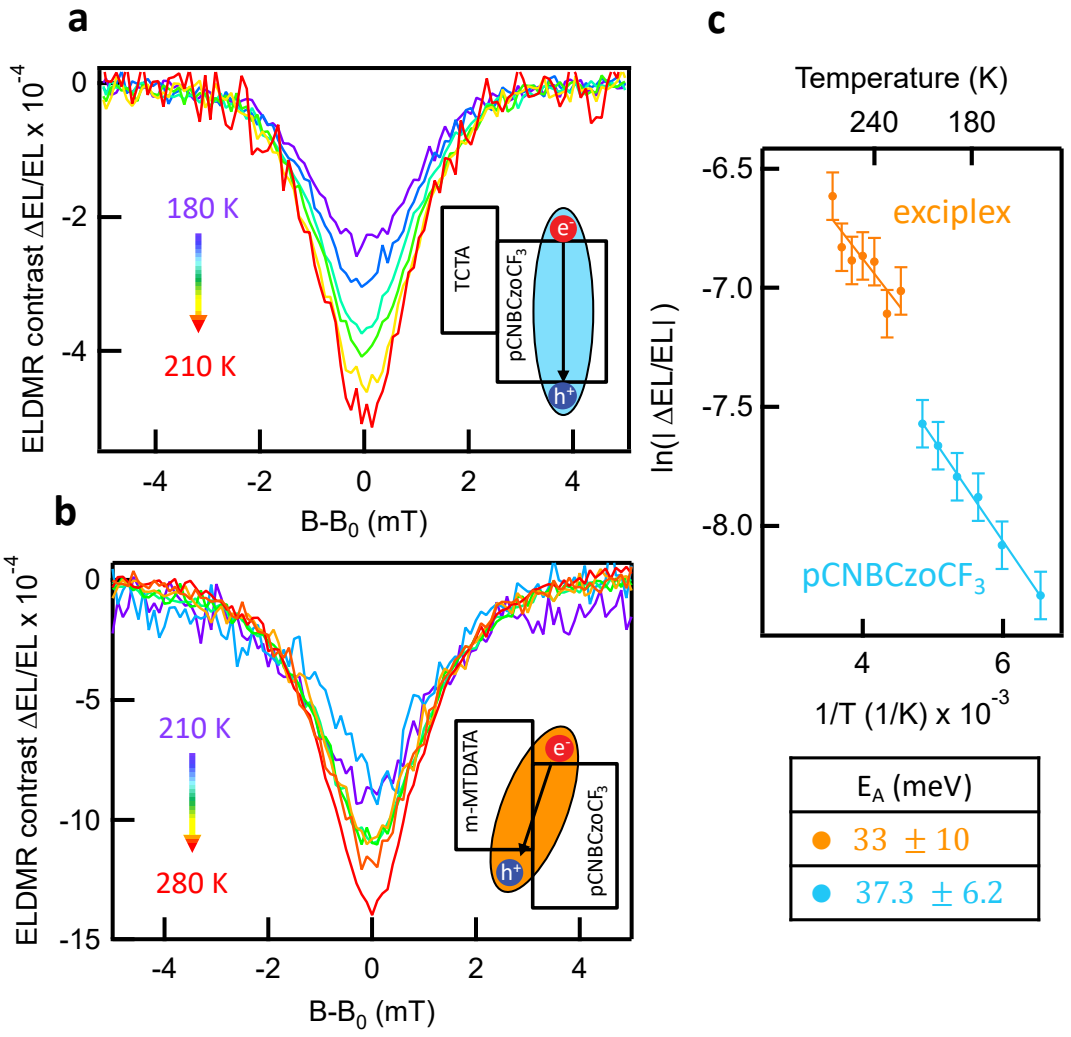

Figure 7.5: a and **b**, Temperature-dependent ELDMR spectra for a pCNBCzoCF$_3$-based OLED and an m-MTDATA:pCNBCzoCF$_3$-based OLED. **c**, Arrhenius plot for the ELDMR contrast of both device types.

temperature. This tendency is contrary to what is commonly observed in magnetic resonance experiments where lower temperatures yield a higher signal intensity due to a higher spin polarization. Consequently, we assign the temperature behavior of the ELDMR spectra to the thermal activation of delayed fluorescence. A quantitative analysis of the signal's temperature dependence can be carried out via an Arrhenius plot, which allows us to derive an activation energy E_A of the probed effect (as introduced in **Chapter 2**, **Section 2.10**). **Figure 7.5c** shows Arrhenius plots for both device types. For OLEDs based on pure pCNBCzoCF$_3$ we find an activation energy of 37.3±6.2 meV and for the exciplex-based OLED 33±10 meV. Both device types yield an activation energy in the range of thermal energy $k_B T$, which fits to TADF emitters. Hence, we consider these values to be an estimate for the singlet–triplet splitting ΔE_{ST}.

The determination of ΔE_{ST} for pCNBCzoCF$_3$ has shown considerable discrepancies in different previous reports. In [140] a ΔE_{ST} of 11 meV was reported, while [141] reported 190 meV. Both values were determined via the difference between emission peaks in PL and phosphorescence spectra of solid pCNBCzoCF$_3$ films at 77 K. This mismatch demonstrates that the determination of ΔE_{ST} via PL measurements is not unambiguous and has to be treated carefully. Our results support the value of [140], which is in the range of thermal energy at room temperature, in line with reasonable values for TADF emitters.

As a comparative method, we measured temperature-dependent EQE of the exciplex-based device to corroborate the activation energies derived via ELDMR. The exact temperature-dependence of a TADF OLED's EQE is non-trivial [31], however, in a first order approximation one can assume: EQE~$\exp\left(\frac{-E_A}{k_B T}\right)$. An Arrhenius analysis of temperature-dependent EQE measurements allows the determination of the activation energy E_A. A schematic illustration of the used setup is shown in the inset of **Figure 7.6a**.

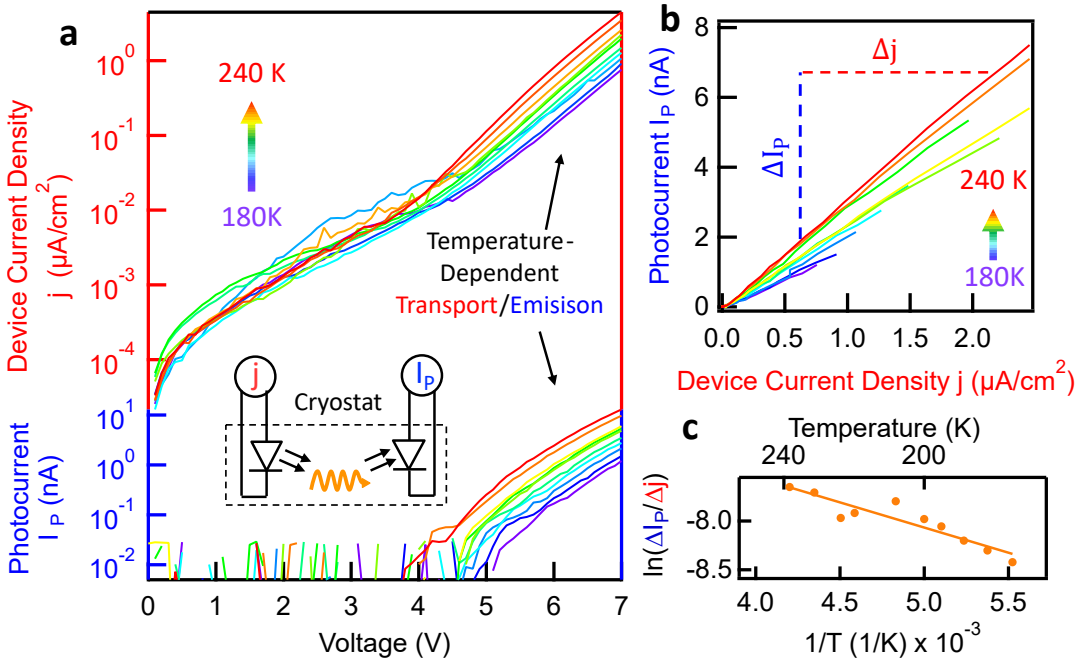

Figure 7.6: a, Temperature-dependent device current density (upper part) and EL intensity (lower part) versus voltage characteristics for an m-MTDATA:pCNBCzoCF$_3$-based OLED. The inset shows a schematic illustration of the used setup. An OLED is driven with a current density j and the emitted light induces a photocurrent I_P in a detector, which is placed in front of the OLED. This construction is placed in a cryostat allowing temperature-dependent measurements. **b**, Temperature-dependent photocurrent I_P versus device current density j. **c**, The slopes of the lines are analyzed with respect to their temperature dependence via an Arrhenius plot.

An OLED is driven by a current j and the emitted light is collected with a photodiode placed in front of the OLED measuring the photocurrent I_P. Temperature-dependent current density (j) and electroluminescence (I_P) to voltage (V) characteristics for an exciplex-based device are shown in **Figure 7.6a**. In order to disentangle the effects of TADF and temperature-dependent hopping transport in organic semiconductors, the photocurrent I_P is plotted vs. the current density j in **Figure 7.6b**. The resulting curves yield a linear dependency. The slope $\Delta I_P/\Delta j$ of these lines is proportional to the EQE of the device. A quantitative analysis of the temperature dependence of these slopes is therefore equivalent to an analysis of the EQE itself. An Arrhenius plot allows the determination of the corresponding activation energy E_A, as shown in **Figure 7.6c**. Here, an activation energy of 44.5±6.5 meV is determined for the exciplex-based device. This value is slightly higher than the value of 33±10 meV, derived via ELDMR, but still consistent within the errors. Overall, a value in the range of thermal energy is obtained confirming the TADF character of the exciplex state between pCNBCzoCF$_3$ and m-MTDATA.

7.4 Photoluminescence Detected Magnetic Resonance

We performed PLDMR measurements in order to explore the differences between the generation of excitons via optical excitation or electrical injection. In PLDMR, the external magnetic field is swept and the change of PL from an optically excited film is probed while resonant microwaves are applied (as introduced in **Chapter 3**, **Section 3.6**). First, we measured temperature-dependent PLDMR on an m-MTDATA:pCNBCzoCF$_3$ blend, which is presented in **Figure 7.7a**.

At low temperatures, there is a superposition of two signal components consisting of a broad positive signal and narrow negative signal. As temperature increases, the contribution of the broad signal vanishes and only the narrow one remains. The narrow component can be attributed to the CT triplet ^{3}CT on pCNBCzoCF$_3$ and the exciplex triplet ^{3}Exc, while the broad component can be attributed to the local triplet ^{3}LE on m-MTDATA.

In order to explain the assignment of the observed signals, the consecutive steps leading to the population of different spin states are illustrated in **Figure 7.7b**. According to photoexcitation spectra of m-MTDATA and pCNBCzoCF$_3$ (**Figure 7.7c**) both local singlets ^{1}LE on m-MTDATA and CT singlets ^{1}CT on pCNBCzoCF$_3$ are initially excited via the 365 nm UV LED we used in PLDMR (**Figure 7.7b**, **i**).

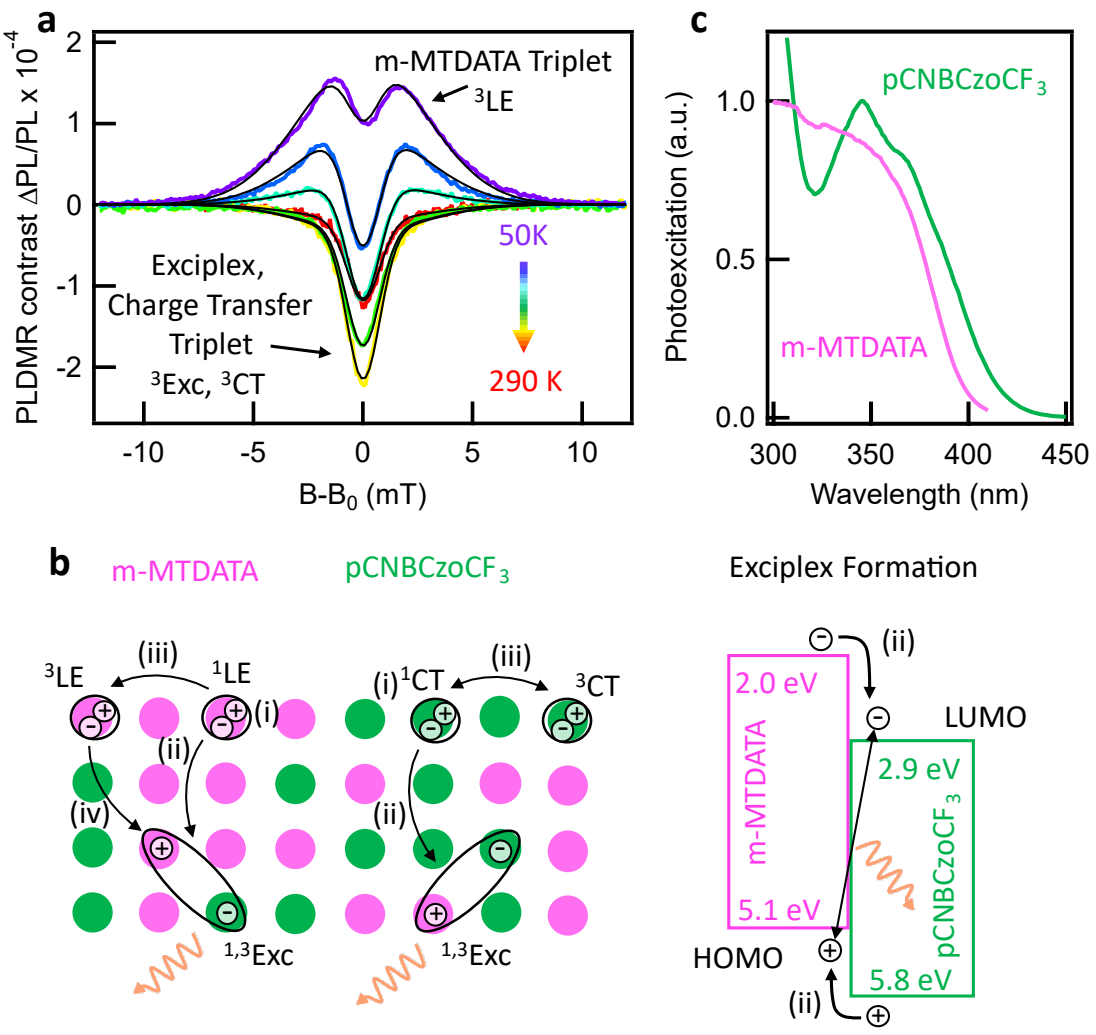

Figure 7.7: a, Temperature-dependent PLDMR spectra for an m-MTDATA:pCNBCzoCF$_3$ blend. A narrow signal at higher temperatures is assigned to the CT and exciplex triplet. The broad signal at lower temperatures is assigned to a local triplet on m-MTDATA. **b**, Illustration of the excitation pathways for singlet and triplet states in a mixed m-MTDATA:pCNBCzoCF$_3$ blend. Each circle represents an m-MTDATA or pCNBCzoCF$_3$ molecule. **(i)** Optical excitation of singlets on both m-MTDATA and pCNBCzoCF$_3$. **(ii)** Formation of exciplex states via CT. **(iii)** Formation of triplets on m-MTDATA and pCNBCzoCF$_3$ via ISC. **(iv)** m-MTDATA triplets can undergo CT to exciplex triplets. The right part of the figure displays the energies of HOMO and LUMO levels for m-MTDATA and pCNBCzoCF$_3$ with an additional illustration of the exciplex formation. Values for HOMO and LUMO energies are taken from [140]. **c**, Photoexcitation spectra for a pristine m-MTDATA and a pristine pCNBCzoCF$_3$ film.

The PL spectrum of an m-MTDATA:pCNBCzoCF$_3$ blend, however, shows a distinct redshift compared to the PL spectra of the pristine materials (**Figure 7.2c**). Consequently, a CT process leads to the formation of an exciplex state (**Figure 7.7b**, **ii**). Here, an electron is transferred from the LUMO of m-MTDATA to the LUMO of pCNBCzoCF$_3$

or a hole is transferred from the HOMO of pCNBCzoCF$_3$ to the HOMO of m-MTDATA (see right side of **Figure 7.7b**).

Exciplex singlets ^{1}Exc decay radiatively as prompt fluorescence or undergo ISC to form exciplex triplets ^{3}Exc. Subsequent RISC back to the singlet state induces delayed fluorescence. Combined prompt and delayed fluorescence give rise to the orange emission spectrum.

Alternatively to the CT process, ISC can facilitate the population of local triplets ^{3}LE on m-MTDATA or CT triplets ^{3}CT on pCNBCzoCF$_3$ (**Figure 7.7b**, **iii**).

For the exciplex triplet, electron and hole are delocalized over two molecules and for the CT triplet they are delocalized over two moieties on pCNBCzoCF$_3$. The distance between them is therefore relatively large resulting in a small dipolar interaction D. As already discussed in **Figure 7.4**, spin species with a small D exhibit narrow signals in magnetic resonance experiments, which is why the narrow component in PLDMR of an m-MTDATA:pCNBCzoCF$_3$ blend fits to the exciplex and the CT triplet. The broad signal can be assigned to the local triplet on m-MTDATA, where electron and hole are located on one molecule leading to a stronger dipolar interaction D and, consequently, to a broader spectrum.

The vanishing of the broad PLDMR signal component at higher temperatures can be explained by the temperature dependence of the CT process from m-MTDATA to pCNBCzoCF$_3$. CT processes are mediated by molecular vibrations which are less activated at lower temperatures [115]. Consequently, the efficiency of the CT process decreases at low temperatures and the probability for ISC from m-MTDATA singlets to triplets increases, which is why the broad signal is more pronounced at lower temperatures. Local m-MTDATA triplets can decay non-radiatively or, alternatively, still undergo CT to the exciplex triplet (**Figure 7.7b**, **iv**) and thus contribute indirectly to delayed fluorescence from exciplexes. Consequently, spin manipulation of m-MTDATA triplets causes a change in exciplex emission intensity as observed by PLDMR, which enables indirect detection of non-emissive local triplet states.

In the next step, we measured PLDMR on a TCTA:pCNBCzoCF$_3$ blend, which is presented in **Figure 7.8a**.

Similar to m-MTDATA:pCNBCzoCF$_3$, there is a superposition of a broad and a narrow signal where the broad component is predominantly pronounced at low temperatures and the narrow one at high temperatures. In this case, the broad signal can be attributed to the local triplet ^{3}LE on TCTA and the narrow one to the CT triplet ^{3}CT on pCNBCzoCF$_3$.

In order to elaborate those assignments, the excitation pathways of spin states in an optically excited TCTA:pCNBCzoCF$_3$ blend are illustrated in **Figure 7.8b**.

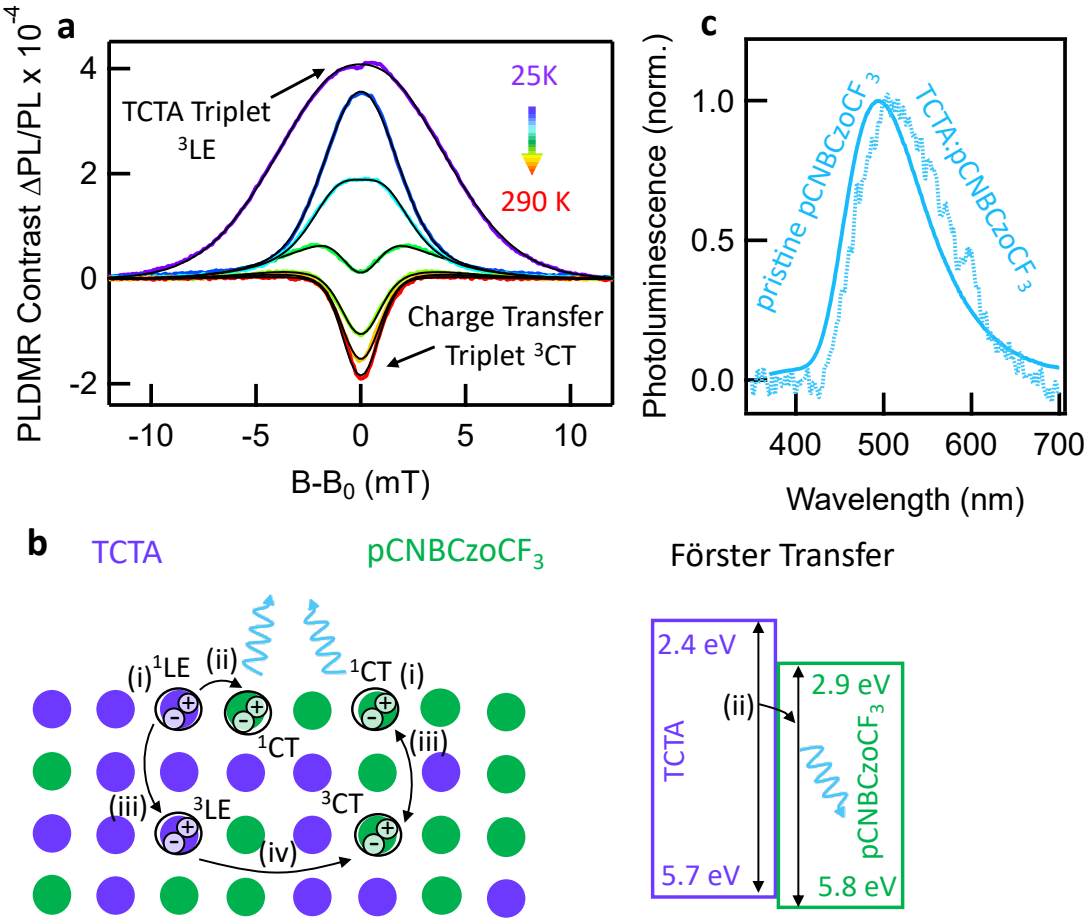

Figure 7.8: a, Temperature-dependent PLDMR spectra for a TCTA:pCNBCzoCF$_3$ blend. A narrow signal at higher temperatures is assigned to the CT triplet on pCNBCzoCF$_3$. The broad signal at lower temperatures is assigned to a local triplet on TCTA. **b**, Illustration of the excitation pathways for singlet and triplet states in a mixed TCTA:pCNBCzoCF$_3$ blend. Each circle represents a TCTA or pCNBCzoCF$_3$ molecule. **(i)** Optical excitation of singlets on both TCTA and pCNBCzoCF$_3$. **(ii)** Förster transfer from TCTA to pCNBCzoCF$_3$. **(iii)** Formation of triplets on TCTA and pCNBCzoCF$_3$ via ISC. Temperature activated reverse ISC is possible for pCNBCzoCF$_3$ ^{3}CT states enabling TADF. **(iv)** TCTA triplets can undergo Dexter transfer to pCNBCzoCF$_3$. The right part of the figure displays the energies of HOMO and LUMO levels for TCTA and pCNBCzoCF$_3$ with an additional illustration of the Förster transfer process. Values for HOMO and LUMO energies are taken from [140]. **c**, PL spectra of a pristine pCNBCzoCF$_3$ film (solid line) and a mixed TCTA:pCNBCzoCF$_3$ blended film (dashed line).

Via optical excitation, both local singlets ^{1}LE on TCTA and CT singlets ^{1}CT on pCNBCzoCF$_3$ are generated (**Figure 7.8b**, **i**) as both materials can be excited at 365 nm according to photoexcitation spectra (For pCNBCzoCF$_3$ see **Figure 7.7c** and for TCTA see [142]).

The PL spectrum of a TCTA:pCNBCzoCF$_3$ blend exhibits only emission from pCNBCzoCF$_3$, while no emission from TCTA or red-shifted exciplex emission is observed (**Figure 7.8c**). Excitations on TCTA must therefore be depopulated efficiently. The absence of emissive exciplex states indicates charge transfer is not expected. An alternative is singlet Förster transfer from TCTA to pCNBCzoCF$_3$ (**Figure 7.8b**, **ii**).

Singlets on both materials can form local triplets ^{3}LE on TCTA or CT triplets ^{3}CT on pCNBCzoCF$_3$ via ISC (**Figure 7.8b**, **iii**). The electron–hole distance of the local triplet on TCTA is small, whereas it is relatively large for the CT triplet on pCNBCzoCF$_3$. This means a strong dipolar interaction D for the local TCTA triplet and a relatively small D for the CT triplet. Therefore, the local TCTA triplet is observed as a broad signal and the CT triplet as a narrow signal.

As the TCTA triplet is detected by monitoring pCNBCzoCF$_3$ PL with PLDMR, Dexter triplet transfer between TCTA and pCNBCzoCF$_3$ seems plausible (**Figure 7.8b**, **iv**). Consequently, ISC on TCTA does not need to be considered as a loss mechanism, but just further delays emission.

7.5 Summary

The relative positions of HOMO and LUMO levels in blends of pCNBCzoCF$_3$ with m-MTDATA or TCTA are similar yet in one case an emissive exciplex state forms while in the other one only pCNBCzoCF$_3$ emits light. By performing both PLDMR and ELDMR, we were able to reveal the characteristic magnetic resonance signatures of triplet states in these systems and determined the respective activation energies for light emission. This information allows us to draw a comprehensive picture of the light generation mechanisms in pCNBCzoCF$_3$-based and in exciplex-based OLEDs. The most important processes for the pCNBCzoCF$_3$-based device are summarized in **Figure 7.9**.

Injected charges populate CT singlet and CT triplet states with a ratio of 1:3. Singlets decay radiatively as prompt fluorescence, while triplets undergo RISC giving rise to delayed fluorescence. Both processes yield the sky-blue emission spectrum of pCNBCzoCF$_3$. The triplet that is involved in RISC is found to be the CT triplet via ELDMR. Local triplets that are characterized by broad magnetic resonance spectra, as found in PLDMR, do not appear in ELDMR and therefore do not play a role in the case

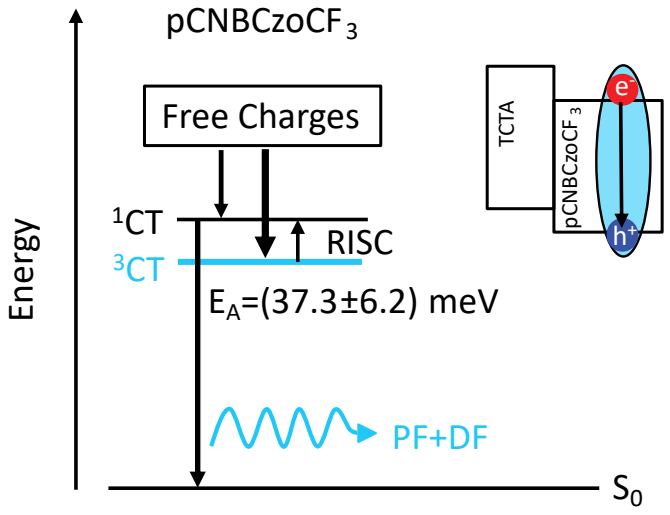

Figure 7.9: Energy diagram for population pathways in an electrically driven $pCNBCzoCF_3$-based device. Free charges populate CT singlets and triplets on $pCNBCzoCF_3$ with a ratio of 1:3. Emission originates from the CT singlet via prompt fluorescence (PF) and via delayed fluorescence (DF) after RISC from the CT triplet to the CT singlet. The activation energy E_A is derived from temperature-dependent ELDMR measurements.

of electrical injection. The activation energy of the RISC process is in the range of thermal energy, proving that $pCNBCzoCF_3$ exhibits TADF.

All involved processes for the exciplex-based device are shown in **Figure 7.10**. The majority of charges populates the singlet and triplet of the exciplex state. Singlets decay radiatively via prompt fluorescence, while triplets undergo RISC giving rise to delayed fluorescence. These processes are responsible for the orange emission. The triplet that is involved in RISC was identified as the exciplex triplet via ELDMR. The local triplet of m-MTDATA was only found in PLMDR but not in ELDMR. The activation energy of the RISC process is close to thermal energy which shows that the exciplex exhibits TADF as well as $pCNBCzoCF_3$ itself. The EL spectrum of the exciplex-based device exhibits a shoulder, which indicates additional population of CT singlets and triplets of $pCNBCzoCF_3$. Singlets can decay radiatively giving rise to the observed shoulder in the EL spectrum but can also undergo a CT to the exciplex singlet. Triplets on $pCNBCzoCF_3$ can undergo a CT to the exciplex triplet or undergo RISC to the CT singlet of $pCNBCzoCF_3$.

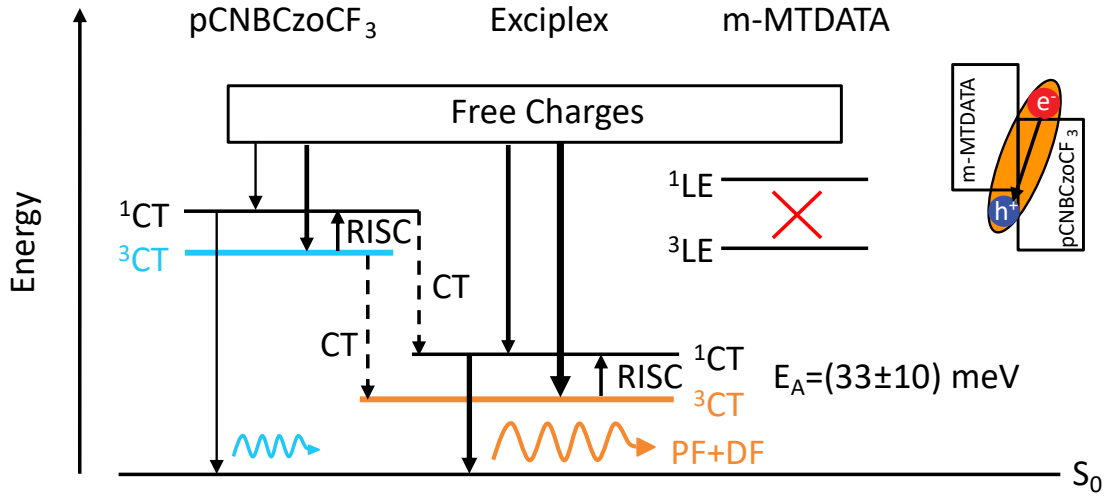

Figure 7.10: Energy diagram for population pathways in an electrically driven m-MTDATA:pCNBCzoCF$_3$-based device. Free charges populate singlets and triplets in the exciplex state but also on pCNBCzoCF$_3$. Emission originates from the exciplex singlet via prompt fluorescence and via delayed fluorescence after RISC from the exciplex triplet. Singlets on pCNBCzoCF$_3$ either decay radiatively or undergo CT to the exciplex singlet. Triplets on pCNBCzoCF$_3$ undergo RISC to form singlets or undergo CT to exciplex triplets. Activation energies of RISC processes were determined from temperature-dependent ELDMR spectra. Neither is emission from m-MTDATA observed nor are signatures of local m-MTDATA triplets found in ELDMR spectra.

7.6 Conclusion

The inherently spin-sensitive techniques of electroluminescence and photoluminescence detected magnetic resonance (ELDMR, PLDMR) were employed to study efficient OLEDs based on intra- and intermolecular TADF effects. From the results we can draw the following conclusions. The electrically generated intermediate triplet states that are responsible for light generation are broadly delocalized (≥1.2 nm) over either one molecule that features intramolecular TADF or over two adjacent molecules that exhibit exciplex type emission. Aside from that, no strongly localized triplet excitons were observed for electrically driven devices with ELDMR. However, upon optical excitation, such localized molecular triplet excitons on the donor materials are generated at low temperatures as evident by PLDMR. By using two independent, temperature-dependent measurements for both types of devices, we derived singlet-triplet gaps of $\Delta E_{ST} = 33 - 45$ meV, which are in the range of thermal energy, being in line with efficient TADF at ambient temperatures. Furthermore, we observed that for orange emitting exciplex based devices a residual sky-blue emission from the used intra-molecular TADF emitter is generated, whose intensity can be voltage controlled. This opens up

the intriguing technical application of tuning both the OLED emission color by voltage adjustments and its brightness by pulse width modulation.

7.7 Additional Experimental Details

The most important experimental details are explained extensively in **Chapter 4**. More information that is specific for this chapter is given in the following.

The materials m-MTDATA, TCTA and BCP were purchased from Sigma-Aldrich. $pCNBCzoCF_3$ was provided by J. V. Grazulevicius and synthesized as described in [140]. All materials were used as received.

All OLED devices were fabricated on indium tin oxide (ITO) covered glass substrates (1 cm^2). First, poly(3,4-ethylendioxythiophene):polystyrolsulfonate (PEDOT:PSS, 4083Ai) from Hereaus was spin coated with 3000 rpm for 1 minute, resulting in a 40 nm thick film. All further device fabrication steps were done inside a nitrogen glovebox to avoid degradation, starting with annealing of the PEDOT:PSS layer for 10 minutes at 130 °C. Donor and acceptor layers were thermally evaporated in an evaporation chamber.

For devices based on pristine $pCNBCzoCF_3$ the device stack was: 40 nm TCTA, 40 nm $pCNBCzoCF_3$, 10 nm BCP. For exciplex bilayer devices: 40 nm m-MTDATA, 40 nm $pCNBCzoCF_3$, 10 nm BCP. For exciplex mixed layer devices: 30 nm m-MTDATA, 30 nm $pCNBCzoCF_3$, with an additional 50 nm mixed layer (1:1) in between the pristine material layers. Finally, for all devices, the top electrode was (5 nm Ca / 120 nm Al), completing 8 OLEDs (3 mm2 each) per substrate.

For PL samples, the materials were evaporated onto glass substrates without the use of ITO, PEDOT:PSS or a metal cathode.

7.8 Contributions to this Chapter

Nikolai Bunzmann[1] (N.B.), Benjamin Krugmann[1] (B.K.), Sebastian Weißenseel[1] (S.W.), Andreas Sperlich[1] (A.S.) and Vladimir Dyakonov[1] (V.D.) designed the experiments. N.B., B.K. and S.W. prepared the devices. Juozas Vidas Grazulevicius[2] (J.V.G.) and Pavlo Stakhira[3] (P.S.) provided the molecule pCNBCzoCF$_3$. N.B., B.K., and S.W. carried out electro-optical device characterization. N.B., B.K., S.W and A.S. performed the magnetic resonance measurements. Liudmila Kudriashova[1] (L.K.) measured photoexcitation and photoluminescence. A.S. and V.D. supervised the research project. N.B., B.K. and A.S. evaluated the data.

[1]Experimental Physics VI, Julius Maximilian University of Würzburg, 97074 Würzburg, Germany

[2]Department of Polymer Chemistry and Technology at Kaunas University of Technology, Radvilenu pl. 19, LT-50254 Kaunas, Lithuania

[3]Lviv Polytechnic National University, S. Bandera 12, 79013 Lviv, Ukraine

8 Summary

This work revealed spin states that are involved in the light generation of organic light-emitting diodes (OLEDs) that are based on thermally activated delayed fluorescence (TADF). First, several donor:acceptor-based TADF systems forming exciplex states were investigated. Afterwards, a TADF emitter that shows intramolecular charge transfer states but also forms exciplex states with a proper donor molecule was studied. The primary experimental technique was electron paramagnetic resonance (EPR), in particular the advanced methods electroluminescence detected magnetic resonance (ELDMR), photoluminescence detected magnetic resonance (PLDMR) and electrically detected magnetic resonance (EDMR). Additional information was gathered from time-resolved and continuous wave photoluminescence measurements.

Chapters 2-4 provided theoretical background that is needed to understand the experiments in this work:

Chapter 2 outlined fundamental processes in the light generation of OLEDs. First, transitions between excitonic states in organic semiconductors were described. Afterwards, typical OLED structures and the single steps from charge carrier injection to electroluminescence emission were explained. Finally, this chapter presented the phenomenon of TADF, including the corresponding molecular properties and luminescence characteristics.

Chapter 3 introduced EPR spectroscopy of triplet states. At the beginning, interactions determining the energetic structure of triplets are described. Subsequently, the structure of triplet EPR spectra and the effects that determine their lineshape are explained. This chapter finished with an explanation of the advanced EPR methods ELDMR, PLDMR and EDMR. Here, the particular suitability of these methods for TADF systems was highlighted.

Chapter 4 explained how ELDMR, PLDMR and EDMR can be technically realized. For PLDMR, an EPR spectrometer including a microwave cavity is used. ELDMR and EDMR rely on a microwave transmission line.

Chapters 5-7 contained the experimental results and conclusions that were gathered in this work:

Chapter 5 presented the application of photophysical characterization methods and EPR techniques on three different donor:acceptor-based TADF systems, namely m-MTDATA:3TPYMB, m-MTDATA:BPhen and THCA:BPhen. The formation of an exciplex state in all of those systems could be proven by a redshift between PL spectra of the pristine donor/acceptor materials and EL spectra of OLEDs employing a donor:acceptor blend as the emissive layer. m-MTDATA:3TPYMB OLEDs showed a maximum EQE of 6.3% at room temperature which exceeds the theoretical limit of 5% for 1st generation OLEDs. Streak camera images of an m-MTDATA:3TPYMB blend and pristine m-MTDATA indicated a considerable reduction of the lifetime of m-MTDATA singlets in the blend. We explained this observation by an ultra-fast charge transfer and the subsequent formation of an exciplex state after optical excitation of a donor:acceptor blend. Temperature-dependent ELDMR measurements on all studied systems exhibited Gaussian-shaped spectra, where the signal intensity increases with increasing temperature. The signal shape was explained by the delocalization of exciplex triplet states which exhibit a small zero-field interaction. The temperature-dependence was attributed to TADF, while activation energies between 16 and 58 meV were obtained via Arrhenius plots. PLDMR measurements on all investigated systems yielded a superposition of a narrow negative and a broad positive signal. The narrow one was similar to the ELDMR signal and was assigned to the exciplex triplet. The broad one was attributed to a local triplet on the donor since local triplets are expected to exhibit a higher zero-field interaction and therefore a broader lineshape. This assignment was further supported by the observation of a PLDMR half-field signal. The most important conclusion from this chapter was that different intermediate spin states are involved in light generation for electrical generation or optical excitation of excitons in donor:acceptor TADF systems.

Chapter 6 presented pulsed EDMR (pEDMR) experiments on donor:acceptor TADF OLEDs based on m-MTDATA:BPhen. We showed, that microwave pulses with a pulse length in the microsecond range induce a time-dependent current change ΔI in an OLED during operation. Time integration of this current change yields a charge ΔQ. The determination of ΔQ at different magnetic fields yielded a spectrum which is almost identical to cwELDMR spectra, showing that pEDMR probes exciplex triplet states. We measured Rabi oscillations from a BDPA radical via pulsed EPR, demonstrating the capability of the used setup. However, the application of a Rabi oscillation pulse scheme to an m-MTDATA:BPhen OLED resulted in a linear increase of the pEDMR signal, while no Rabi oscillations could be observed. Power- and pulse length-dependent pEDMR measurements showed, that the signal intensity scales with the pulse energy (pulse power x pulse length), regardless of whether the power or the length was varied.

We concluded, that the time scale of delayed fluorescence (DF) is too long for coherent spin manipulation to be transferred to the rate of DF. Instead, spin–lattice relaxation causes decoherence before reverse intersystem crossing takes place. Consequently, Rabi oscillations could not be observed. We explained the microwave-induced current change by sample heating due to microwave absorption.

Chapter 7 presented the application of photophysical characterization methods and EPR techniques on the molecule pCNBCzoCF$_3$. We built two types of devices. OLEDs with pCNBCzoCF$_3$ in the emissive layer exhibited sky-blue electroluminescence. This emission was assigned to intramolecular CT states on pCNBCzoCF$_3$. OLEDs with an m-MTDATA:pCNBCzoCF$_3$ interface in the emissive layer showed orange electroluminescence. We concluded, that an exciplex state is formed between m-MTDATA and pCNBCzoCF$_3$ causing a redshift to the orange region. At high voltages orange exciplex emission and sky-blue CT state emission superimposed resulting in a white emission spectrum. Temperature-dependent ELDMR measurements on both types of devices showed Gaussian-shaped signals. For the pCNBCzoCF$_3$-based device, the signal was assigned to the intramolecular CT triplet, and for the m-MTDATA:pCNBCzoCF$_3$-based device to the intermolecular exciplex triplet. Arrhenius plots of the signal intensities yielded activation energies in the range of 33-45 meV, supporting the TADF character of both device types. PLDMR measurements on an m-MTDATA:pCNBCzoCF$_3$ blend revealed the population of the exciplex triplet as well as local triplets on m-MTDATA under optical excitation. PLDMR on a TCTA:pCNBCzoCF$_3$ blend showed signatures of the CT triplet and the local TCTA triplet under optical excitation. Overall, both types of devices exhibited TADF character, while only CT and exciplex triplet states are relevant for devices in operation.

All in all, this work demonstrated the (still underrated) value of EPR spectroscopy within the research field of TADF based OLEDs. In particular, the importance of experiments on devices under operation was highlighted. The results and conclusions from this thesis contribute to a better understanding of TADF based OLEDs and can be of great benefit for their further development.

Zusammenfassung

In dieser Arbeit wurden Spinzustände identifiziert, die an der Lichterzeugung von organischen Leuchtdioden beteiligt sind, welche auf thermisch aktivierter verzögerter Fluoreszenz (engl. TADF) basieren. Zuerst wurden mehrere Donor:Akzeptor basierte TADF Systeme untersucht. Danach wurde ein TADF Emitter studiert, welcher intramolekulare Ladungstransfer Zustände (engl. CT states) zeigt, aber auch Exziplex Zustände mit einem geeigneten Donor Molekül bildet. In erster Linie wurde die experimentelle Methode der Elektronenspinresonanz (ESR) genutzt, insbesondere die erweiterten Techniken Elektrolumineszenz detektierte Magnetresonanz (ELDMR), Photolumineszenz detektierte Magnetresonanz (PLDMR) und elektrisch detektierte Magnetresonanz (EDMR). Zusätzliche Informationen wurden aus zeitaufgelösten und dauerstrich Photolumineszenz Messungen gewonnen.

In den **Kapiteln 2-4** wurden die theoretischen Hintergründe erklärt, die benötigt werden um die Experimente in dieser Arbeit zu verstehen.

In **Kapitel 2** wurden grundlegende Prozesse bei der Lichterzeugung von OLEDs skizziert. Am Anfang wurden Übergänge zwischen exzitonischen Zuständen in organischen Halbleitern beschrieben. Danach wurden typische OLED Strukturen sowie die einzelnen Schritte von Ladungsträgerinjektion hinzu Elektrolumineszenz beschrieben. Zum Schluss wird das Phänomen von TADF erklärt. Dabei wird auf die entsprechenden molekularen Eigenschaften und die Lumineszenzeigenschaften eingegangen.

In **Kapitel 3** wurde eine Einführung in die ESR Spektroskopie von Triplet Zuständen gegeben. Zunächst wurden die Wechselwirkungen beschrieben, welche die energetische Struktur von Triplets bestimmen. Danach wurden die Struktur von ESR Spektren und die Effekte, welche deren Linienform bestimmen, erklärt. Am Schluss wurden die erweiterten ESR Methoden ELDMR, PLDMR und EDMR erläutert. Dabei wird darauf eingegangen, warum diese Methoden für die Untersuchung von TADF Systemen besonders geeignet sind.

In **Kapitel 4** wurde erklärt wie ELDMR, PLDMR und EDMR technisch umgesetzt werden. Für PLDMR wird ein ESR Spektrometer mit einem Mikrowellenresonator verwendet. Die experimentellen Aufbauten für ELDMR und EDMR basieren auf einem Mikrowellentransmissionsstreifen.

Die **Kapitel 5-7** beinhalten die experimentellen Ergebnisse und die Schlussfolgerungen, die in dieser Thesis erarbeitet wurden.

In **Kapitel 5** wurde die Anwendung von photophysikalischen Charakterisierungsmethoden und ESR Techniken auf drei unterschiedliche Donor:Akzeptor TADF Systeme gezeigt. Die Systeme sind m-MTDATA:3TPYMB, m-MTDATA:BPhen und THCA:BPhen. In allen Systemen konnte das Ausbilden eines Exziplex Zustandes gezeigt

werden durch eine Rotverschiebung zwischen den Donor/Akzeptor PL Spektren und dem EL Spektrum einer OLED, welche eine Donor:Akzeptor Mischschicht in der Emissionsschicht verwendet. m-MTDATA:3TPYMB OLEDs zeigten bei Raumtemperatur eine maximale EQE von 6.3%, was das theoretische Limit von 1. Generation OLEDs von 5% übersteigt. Streak Kamera Aufnahmen eines Films aus m-MTDATA:3TPYMB und eines Films aus reinem m-MTDATA deuten auf eine deutliche Reduzierung der Lebensdauer von m-MTDATA im Gemisch hin. Diese Beobachtung wurde durch einen extrem schnellen Ladungstransfer und die darauffolgende Ausbildung eines Exziplex Zustandes nach optischer Anregung erklärt. Temperaturabhängige ELDMR Messungen an allen untersuchten Systemen haben Gaussförmige Spektren ergeben, wobei die Signalintensität mit steigender Temperatur steigt. Die Signalform wurde durch die Delokalisierung von Exziplex Tripletzuständen erklärt, welche eine kleine Nullfeldaufspaltung aufweisen. Die Temperaturabhängigkeit wurde TADF zugeordnet, wobei Aktivierungsenergien im Bereich von 16 bis 58 meV über eine Arrhenius Auftragung bestimmt wurden. PLDMR Messungen an allen untersuchten Systemen haben eine Überlagerung eines schmalen negativen und eines breiten positiven Signals ergeben. Das schmale Signal war ähnlich zum ELDMR Signal und wurde einem Exziplex Triplet zugeordnet. Das breite Signal wurde einem lokalisierten Triplet auf dem Donor zugeordnet, weil lokalisierte eine größere Nullfeldaufspaltung aufweisen und daher ein breiteres Signal erwartet wird. Diese Zuordnung wurde zusätzlich durch das Auftreten eines PLDMR Halbfeldsignals bekräftigt. Die wichtigste Schlussfolgerung dieses Kapitels war, dass in Donor:Akzeptor Systemen bei elektrischer Erzeugung und optischer Anregung von Exzitonen unterschiedliche Zwischenspinzustände an der Lichterzeugung beteiligt sind.

In **Kapitel 6** wurden gepulste EDMR (engl. pEDMR) Experimente an Donor:Akzeptor OLEDs gezeigt, welche auf m-MTDATA:BPhen basieren. Wir konnten zeigen, dass Mikrowellenpulse mit einer Pulslänge im Mikrosekundenbereich eine zeitabhängige Stromänderung ΔI in einer OLED unter Betrieb induzieren. Das zeitliche Integral dieser Stromänderung ergibt eine Ladung ΔQ. Die Bestimmung von ΔQ bei unterschiedlichen Magnetfeldern ergab ein Spektrum, welches fast identisch zu einem ELDMR Spektrum ist. Daraus folgt, dass mit pEDMR Exziplex Tripletzustände untersucht werden. Über gepulstes ESR haben wir Rabioszillationen an einem BDPA Radikal gemessen, was die prinzipiellen Möglichkeiten des genutzten experimentellen Aufbaus zeigt. Beim Anwenden einer Pulssequenz für Rabioszillationen auf eine m-MTDATA:BPhen OLED sind trotzdem keine Rabioszillationen aufgetreten, sondern ein linearer Anstieg der Signalintensität mit der Pulslänge. Leistungs- und pulslängenabhängige pEDMR Messungen haben gezeigt, dass die Signalintensität mit der Energie des Pulses (Pulsleis-

tung mal Pulslänge) ansteigt, unabhängig davon, ob die Pulsleistung oder die Pulslänge variiert wird. Daraus schlossen wir, dass die Zeitskala, auf der verzögerte Fluoreszenz (VF) auftritt, zu lange ist, als dass kohärente Spinmanipulation auf die Rate der VF übertragen wird. Stattdessen verursacht Spin–Gitter Relaxation Dekohärenz bevor Spinkonversion vom Triplet zum Singulett statt findet. Deshalb konnten keine Rabioszillationen beobachtet werden. Die durch Mikrowellen induzierte Stromänderung haben wird durch Heizen erklärt, welches sich aus Mikrowellenabsorption ergibt.

In **Kapitel 7** wurde die Anwendung von photophysikalischen Charakterisierungsmethoden und ESR Techniken auf das Molekül pCNBCzoCF$_3$ gezeigt. Wir haben zwei unterschiedliche Typen von Bauteilen hergestellt. OLEDs mit pCNBCzoCF$_3$ in der Emissionsschicht haben himmelblaues Licht emittiert. Diese Emission wurde einem intramolekularen CT Zustand auf pCNBCzoCF$_3$ zugeordnet. OLEDs mit einer m-MTDATA:pCNBCzoCF$_3$ Grenzschicht in der Emissionsschicht haben orange Elektrolumineszenz gezeigt. Daraus folgerten wir, dass sich zwischen m-MTDATA und pCNBCzoCF$_3$ ein Exziplex Zustand ausbildet, wodurch sich die Rotverschiebung zu orange ergibt. Bei hohen Spannungen wurde die orange Emission von zusätzlicher himmelblauer Emission überlagert, was insgesamt zu einem weißen Spektrum geführt hat. Temperaturabhängige ELDMR Messungen an beiden Typen von OLEDs haben Gaussförmige Spektren gezeigt. Bei der OLED, die auf pCNBCzoCF$_3$ basiert, wurde das Signal einem intramolekularen Triplet zugeordnet und bei der OLED, die auf m-MTDATA:pCNBCzoCF$_3$ basiert, dem intermolekularen Exziplex Triplet. Eine Analyse der Temperaturabhängigkeit mit Hilfe einer Arrhenius Auftragung ergab Aktivierungsenergien im Bereich 33 bis 45 meV, was die TADF Eigenschaften von beiden Typen von OLEDs unterstützt. PLDMR Messungen an einem m-MTDATA:pCNBCzoCF$_3$ Gemisch zeigten, dass bei optischer Anregung das Exziplex Triplet und das lokalisierte Triplet auf m-MTDATA bevölkert werden. PLDMR Messungen an einem TCTA:pCNBCzoCF$_3$ Gemisch zeigten, dass bei optischer Anregung das intramolekulare CT Triplet auf pCNBCzoCF$_3$ und das lokalisierte Triplet auf TCTA bevölkert werden. Insgesamt wiesen beide Typen von OLEDs TADF Eigenschaften auf, wobei für den elektrischen Betrieb der OLEDs lediglich das CT bzw. das Exziplex Triplet relevant sind.

Alles in allem wurde durch diese Arbeit verdeutlicht, wie wertvoll die (immer noch unterschätzte) ESR Spektroskopie im Forschungsbereich der TADF OLEDs ist. Insbesondere wurde die Bedeutung von Experimenten an Bauteilen im Betrieb herausgearbeitet. Die Ergebnisse und Schlussfolgerungen aus dieser Thesis tragen zu einem besseren Verständnis von TADF OLEDs bei und können für deren Weiterentwicklung von großem Nutzen sein.

Bibliography

[1] G. F. Simmons. *Precalculus Mathematics in a Nutshell: Geometry, Algebra, Trigonometry*. Resource Publications (2003). ISBN 1592441300.

[2] M. Y. Wong and E. Zysman-Colman. Purely organic thermally activated delayed fluorescence materials for organic light-emitting diodes. *Advanced Materials*, **29**, 22, 1605444 (2017). doi: 10.1002/adma.201605444.

[3] T. Shimizu and H. Fukagawa. Trends in research and development of OLED.

[4] C. W. Tang and S. A. VanSlyke. Organic electroluminescent diodes. *Applied Physics Letters*, **51**, 12, 913 (1987). doi: 10.1063/1.98799.

[5] M. A. Baldo, D. O'brien, Y. You, A. Shoustikov, S. Sibley, M. Thompson and S. R. Forrest. Highly efficient phosphorescent emission from organic electroluminescent devices. *Nature*, **395**, 6698, 151 (1998). doi: 10.1038/25954.

[6] C. Adachi, M. A. Baldo, M. E. Thompson and S. R. Forrest. Nearly 100% internal phosphorescence efficiency in an organic light-emitting device. *Journal of Applied Physics*, **90**, 10, 5048 (2001). doi: 10.1063/1.1409582.

[7] H. Xu, R. Chen, Q. Sun, W. Lai, Q. Su, W. Huang and X. Liu. Recent progress in metal–organic complexes for optoelectronic applications. *Chemical Society Reviews*, **43**, 10, 3259 (2014). doi: 10.1039/C3CS60449G.

[8] Y. Zhang, J. Lee and S. R. Forrest. Tenfold increase in the lifetime of blue phosphorescent organic light-emitting diodes. *Nature Communications*, **5**, 5008 (2014). doi: 10.1038/ncomms6008.

[9] C. Parker and C. Hatchard. Triplet-singlet emission in fluid solutions. Phosphorescence of eosin. *Transactions of the Faraday Society*, **57**, 1894 (1961). doi: 10.1039/TF9615701894.

[10] K. Goushi, K. Yoshida, K. Sato and C. Adachi. Organic light-emitting diodes employing efficient reverse intersystem crossing for triplet-to-singlet state conversion. *Nature Photonics*, **6**, 4, 253 (2012). doi: 10.1038/nphoton.2012.31.

[11] H. Uoyama, K. Goushi, K. Shizu, H. Nomura and C. Adachi. Highly efficient organic light-emitting diodes from delayed fluorescence. *Nature*, **492**, 7428, 234 (2012). doi: 10.1038/nature11687.

[12] Q. Zhang, B. Li, S. Huang, H. Nomura, H. Tanaka and C. Adachi. Efficient blue organic light-emitting diodes employing thermally activated delayed fluorescence. *Nature Photonics*, **8**, 4, 326 (2014). doi: 10.1038/nphoton.2014.12.

[13] S. Wu, M. Aonuma, Q. Zhang, S. Huang, T. Nakagawa, K. Kuwabara and C. Adachi. High-efficiency deep-blue organic light-emitting diodes based on a thermally activated delayed fluorescence emitter. *Journal of Materials Chemistry C*, **2**, 3, 421 (2014). doi: 10.1039/C3TC31936A.

[14] Y. J. Cho, S. K. Jeon, B. D. Chin, E. Yu and J. Y. Lee. The design of dual emitting cores for green thermally activated delayed fluorescent materials. *Angewandte Chemie International Edition*, **54**, 17, 5201 (2015). doi: 10.1002/anie.201412107.

[15] M. Taneda, K. Shizu, H. Tanaka and C. Adachi. High efficiency thermally activated delayed fluorescence based on 1, 3, 5-tris (4-(diphenylamino) phenyl)-2, 4, 6-tricyanobenzene. *Chemical Communications*, **51**, 24, 5028 (2015). doi: 10.1039/C5CC00511F.

[16] J. Li, T. Nakagawa, J. MacDonald, Q. Zhang, H. Nomura, H. Miyazaki and C. Adachi. Highly efficient organic light-emitting diode based on a hidden thermally activated delayed fluorescence channel in a heptazine derivative. *Advanced Materials*, **25**, 24, 3319 (2013). doi: 10.1002/adma.201300575.

[17] S. Wang, X. Yan, Z. Cheng, H. Zhang, Y. Liu and Y. Wang. Highly efficient near-infrared delayed fluorescence organic light emitting diodes using a phenanthrene-based charge-transfer compound. *Angewandte Chemie International Edition*, **54**, 44, 13068 (2015). doi: 10.1002/anie.201506687.

[18] M. K. Etherington, J. Gibson, H. F. Higginbotham, T. J. Penfold and A. P. Monkman. Revealing the spin–vibronic coupling mechanism of thermally activated delayed fluorescence. *Nature Communications*, **7**, 13680 (2016). doi: 10.1038/ncomms13680.

[19] C. L. Linfoot, M. J. Leitl, P. Richardson, A. F. Rausch, O. Chepelin, F. J. White, H. Yersin and N. Robertson. Thermally activated delayed fluorescence (TADF) and enhancing photoluminescence quantum yields of [Cu^{I}

(diimine)(diphosphine)]$^+$ complexes–Photophysical, structural, and computational studies. *Inorganic Chemistry*, **53**, 20, 10854 (2014). doi: 10.1021/ic500889s.

[20] J. Gibson, A. P. Monkman and T. J. Penfold. The importance of vibronic coupling for efficient reverse intersystem crossing in thermally activated delayed fluorescence molecules. *ChemPhysChem*, **17**, 19, 2956 (2016). doi: 10.1002/cphc.201600662.

[21] P. K. Samanta, D. Kim, V. Coropceanu and J.-L. Bredas. Up-conversion intersystem crossing rates in organic emitters for thermally activated delayed fluorescence: impact of the nature of singlet vs triplet excited states. *Journal of the American Chemical Society*, **139**, 11, 4042 (2017). doi: 10.1021/jacs.6b12124.

[22] T. Chen, L. Zheng, J. Yuan, Z. An, R. Chen, Y. Tao, H. Li, X. Xie and W. Huang. Understanding the control of singlet-triplet splitting for organic exciton manipulating: a combined theoretical and experimental approach. *Scientific Reports*, **5**, 10923 (2015). doi: 10.1038/srep10923.

[23] C. M. Marian. Mechanism of the triplet-to-singlet upconversion in the assistant dopant ACRXTN. *The Journal of Physical Chemistry C*, **120**, 7, 3715 (2016). doi: 10.1021/acs.jpcc.6b00060.

[24] F. B. Dias, J. Santos, D. R. Graves, P. Data, R. S. Nobuyasu, M. A. Fox, A. S. Batsanov, T. Palmeira, M. N. Berberan-Santos, M. R. Bryce et al. The role of local triplet excited states and D-A relative orientation in thermally activated delayed fluorescence: photophysics and devices. *Advanced Science*, **3**, 12 (2016). doi: 10.1002/advs.201600080.

[25] T. Ogiwara, Y. Wakikawa and T. Ikoma. Mechanism of intersystem crossing of thermally activated delayed fluorescence molecules. *The Journal of Physical Chemistry A*, **119**, 14, 3415 (2015). doi: 10.1021/acs.jpca.5b02253.

[26] P. L. dos Santos, F. B. Dias and A. P. Monkman. Investigation of the mechanisms giving rise to TADF in exciplex states. *The Journal of Physical Chemistry C*, **120**, 32, 18259 (2016). doi: 10.1021/acs.jpcc.6b05198.

[27] J. A. Weil, J. R. Bolton and J. E. Wertz. *Electron spin resonance: elementary theory and practical applications*. New York (1994). ISBN 0-471-57234-9.

[28] A. Köhler and H. Bässler. *Electronic processes in organic semiconductors: An introduction*. John Wiley & Sons (2015). ISBN 9783527332922.

[29] W. Demtröder. *Experimentalphysik 3: Atome, Moleküle und Festkörper*. Springer-Verlag (2010). ISBN 9783642039102.

[30] W. Brütting, J. Frischeisen, T. D. Schmidt, B. J. Scholz and C. Mayr. Device efficiency of organic light-emitting diodes: progress by improved light outcoupling. *physica status solidi (a)*, **210**, 1, 44 (2013). doi: 10.1002/pssa.201228320.

[31] Y. Tao, K. Yuan, T. Chen, P. Xu, H. Li, R. Chen, C. Zheng, L. Zhang and W. Huang. Thermally activated delayed fluorescence materials towards the breakthrough of organoelectronics. *Advanced Materials*, **26**, 47, 7931 (2014). doi: 10.1002/adma.201402532.

[32] W. Nolting. *Grundkurs Theoretische Physik 6: Statistische Physik*, volume 5. Springer (2005). ISBN 978-3-540-20505-0.

[33] T. J. Penfold, E. Gindensperger, C. Daniel and C. M. Marian. Spin-vibronic mechanism for intersystem crossing. *Chemical Reviews*, **118**, 15, 6975 (2018). doi: 10.1021/acs.chemrev.7b00617.

[34] M. Alam and D. Cameron. Optical and electrical properties of transparent conductive ITO thin films deposited by sol–gel process. *Thin Solid Films*, **377**, 455 (2000). doi: 10.1016/S0040-6090(00)01369-9.

[35] R. H. Fowler and L. Nordheim. Electron emission in intense electric fields. *Proceedings of the Royal Society of London. Series A, Containing Papers of a Mathematical and Physical Character*, **119**, 781, 173 (1928). doi: 10.1098/rspa.1928.0091.

[36] J. Simmons. Richardson-schottky effect in solids. *Physical Review Letters*, **15**, 25, 967 (1965). doi: 10.1103/PhysRevLett.15.967.

[37] Z. Chiguvare, J. Parisi and V. Dyakonov. Current limiting mechanisms in indium-tin-oxide/poly3-hexylthiophene/aluminum thin film devices. *Journal of Applied Physics*, **94**, 4, 2440 (2003). doi: 10.1063/1.1588358.

[38] H. Bässler. Charge transport in disordered organic photoconductors a monte carlo simulation study. *physica status solidi (b)*, **175**, 1, 15 (1993). doi: 10.1002/pssb.2221750102.

[39] A. Miller and E. Abrahams. Impurity conduction at low concentrations. *Physical Review*, **120**, 3, 745 (1960). doi: 10.1103/PhysRev.120.745.

[40] S. V. Novikov, D. H. Dunlap, V. M. Kenkre, P. E. Parris and A. V. Vannikov. Essential role of correlations in governing charge transport in disordered organic materials. *Physical Review Letters*, **81**, 20, 4472 (1998). doi: 10.1103/PhysRevLett.81.4472.

[41] W. Pasveer, J. Cottaar, C. Tanase, R. Coehoorn, P. Bobbert, P. Blom, D. De Leeuw and M. Michels. Unified description of charge-carrier mobilities in disordered semiconducting polymers. *Physical Review Letters*, **94**, 20, 206601 (2005). doi: 10.1103/PhysRevLett.94.206601.

[42] V. I. Adamovich, S. R. Cordero, P. I. Djurovich, A. Tamayo, M. E. Thompson, B. W. D'Andrade and S. R. Forrest. New charge-carrier blocking materials for high efficiency OLEDs. *Organic Electronics*, **4**, 2-3, 77 (2003). doi: 10.1016/j.orgel.2003.08.003.

[43] A. Brown, D. Bradley, J. Burroughes, R. Friend, N. Greenham, P. Burn, A. Holmes and A. Kraft. Poly(p-phenylenevinylene) light-emitting diodes: enhanced electroluminescent efficiency through charge carrier confinement. *Applied Physics Letters*, **61**, 23, 2793 (1992). doi: 10.1063/1.108094.

[44] L. J. Rothberg and A. J. Lovinger. Status of and prospects for organic electroluminescence. *Journal of Materials Research*, **11**, 12, 3174 (1996). doi: 10.1557/JMR.1996.0403.

[45] N. C. Greenham, R. H. Friend and D. D. Bradley. Angular dependence of the emission from a conjugated polymer light-emitting diode: implications for efficiency calculations. *Advanced Materials*, **6**, 6, 491 (1994). doi: 10.1002/adma.19940060612.

[46] K. Meerholz and D. C. Müller. Outsmarting waveguide losses in thin-film light-emitting diodes. *Advanced Functional Materials*, **11**, 4, 251 (2001). doi: 10.1002/1616-3028(200108)11:4<251::AID-ADFM251>3.0.CO;2-Y.

[47] H. Greiner. Light extraction from organic light emitting diode substrates: simulation and experiment. *Japanese Journal of Applied Physics*, **46**, 7R, 4125 (2007). doi: 10.1143/JJAP.46.4125.

[48] D. Yokoyama, A. Sakaguchi, M. Suzuki and C. Adachi. Horizontal orientation of linear-shaped organic molecules having bulky substituents in neat and doped vacuum-deposited amorphous films. *Organic Electronics*, **10**, 1, 127 (2009). doi: 10.1016/j.orgel.2008.10.010.

[49] T.-A. Lin, T. Chatterjee, W.-L. Tsai, W.-K. Lee, M.-J. Wu, M. Jiao, K.-C. Pan, C.-L. Yi, C.-L. Chung, K.-T. Wong et al. Sky-blue organic light emitting diode with 37% external quantum efficiency using thermally activated delayed fluorescence from spiroacridine-triazine hybrid. *Advanced Materials*, **28**, 32, 6976 (2016). doi: 10.1002/adma.201601675.

[50] T. D. Schmidt, T. Lampe, P. I. Djurovich, M. E. Thompson, W. Brütting et al. Emitter orientation as a key parameter in organic light-emitting diodes. *Physical Review Applied*, **8**, 3, 037001 (2017). doi: 10.1103/PhysRevApplied.8.037001.

[51] M. Pope, H. Kallmann and P. Magnante. Electroluminescence in organic crystals. *The Journal of Chemical Physics*, **38**, 8, 2042 (1963). doi: 10.1063/1.1733929.

[52] H. Yersin. *Highly efficient OLEDs with phosphorescent materials*. John Wiley & Sons (2008). ISBN 9783527405947.

[53] N. A. Drigo, L. G. Kudriashova, S. Weissenseel, A. Sperlich, A. J. Huckaba, M. K. Nazeeruddin and V. Dyakonov. Photophysics of deep blue acridane- and benzonitrile-based emitter employing thermally activated delayed fluorescence. *The Journal of Physical Chemistry C*, **122**, 39, 22796 (2018). doi: 10.1021/acs.jpcc.8b08716.

[54] Z. Yang, Z. Mao, Z. Xie, Y. Zhang, S. Liu, J. Zhao, J. Xu, Z. Chi and M. P. Aldred. Recent advances in organic thermally activated delayed fluorescence materials. *Chemical Society Reviews*, **46**, 3, 915 (2017). doi: 10.1039/c6cs00368k.

[55] X.-K. Chen, S.-F. Zhang, J.-X. Fan and A.-M. Ren. Nature of highly efficient thermally activated delayed fluorescence in organic light-emitting diode emitters: nonadiabatic effect between excited states. *The Journal of Physical Chemistry C*, **119**, 18, 9728 (2015). doi: 10.1021/acs.jpcc.5b00276.

[56] S. Weissenseel, N. A. Drigo, L. G. Kudriashova, M. Schmid, T. Morgenstern, K.-H. Lin, A. Prlj, C. Corminboeuf, A. Sperlich, W. Brütting et al. Getting the right twist: influence of donor–acceptor dihedral angle on exciton kinetics and singlet–triplet gap in deep blue thermally activated delayed fluorescence emitter. *The Journal of Physical Chemistry C*, **123**, 45, 27778 (2019). doi: 10.1021/acs.jpcc.9b08269.

[57] M. Sarma and K.-T. Wong. Exciplex: an intermolecular charge-transfer approach for TADF. *ACS Applied Materials & Interfaces*, **10**, 23, 19279 (2018). doi: 10.1021/acsami.7b18318.

[58] S. Hirata, Y. Sakai, K. Masui, H. Tanaka, S. Y. Lee, H. Nomura, N. Nakamura, M. Yasumatsu, H. Nakanotani, Q. Zhang et al. Highly efficient blue electroluminescence based on thermally activated delayed fluorescence. *Nature Materials*, **14**, 3, 330 (2015). doi: 10.1038/nmat4154.

[59] X.-K. Chen, Y. Tsuchiya, Y. Ishikawa, C. Zhong, C. Adachi and J.-L. Brédas. A new design strategy for efficient thermally activated delayed fluorescence organic emitters: from twisted to planar structures. *Advanced Materials*, **29**, 46, 1702767 (2017). doi: 10.1002/adma.201702767.

[60] Y. Wang, K. Sahin-Tiras, N. J. Harmon, M. Wohlgenannt and M. E. Flatté. Immense magnetic response of exciplex light emission due to correlated spin-charge dynamics. *Physical Review X*, **6**, 1, 011011 (2016). doi: 10.1103/PhysRevX.6.011011.

[61] F. B. Dias, T. J. Penfold and A. P. Monkman. Photophysics of thermally activated delayed fluorescence molecules. *Methods and Applications in Fluorescence*, **5**, 1, 012001 (2017). doi: 10.1088/2050-6120/aa537e.

[62] C. Parker and C. Hatchard. Delayed fluorescence from solutions of anthracene and phenanthrene. *Proceedings of the Royal Society of London. Series A. Mathematical and Physical Sciences*, **269**, 1339, 574 (1962). doi: 10.1098/rspa.1962.0197.

[63] D. Kondakov. Characterization of triplet-triplet annihilation in organic light-emitting diodes based on anthracene derivatives. *Journal of Applied Physics*, **102**, 11, 114504 (2007). doi: 10.1063/1.2818362.

[64] D. Kondakov, T. Pawlik, T. Hatwar and J. Spindler. Triplet annihilation exceeding spin statistical limit in highly efficient fluorescent organic light-emitting diodes. *Journal of Applied Physics*, **106**, 12, 124510 (2009). doi: 10.1063/1.3273407.

[65] Colour & Vision Research Laboratory–Institute of Ophthalmology. CVRL functions. http://www.cvrl.org/.

[66] J.-S. Kim, P. K. Ho, N. C. Greenham and R. H. Friend. Electroluminescence emission pattern of organic light-emitting diodes: implications for device efficiency calculations. *Journal of Applied Physics*, **88**, 2, 1073 (2000). doi: 10.1063/1.373779.

[67] W. D. Wright. A re-determination of the trichromatic coefficients of the spectral colours. *Transactions of the Optical Society*, **30**, 4, 141 (1929). doi: 10.1088/1475-4878/30/4/301.

[68] J. Guild. The colorimetric properties of the spectrum. *Philosophical Transactions of the Royal Society of London. Series A, Containing Papers of a Mathematical or Physical Character*, **230**, 681-693, 149 (1931). doi: 10.1098/rsta.1932.0005.

[69] OsramSylvania. Colorcalculator. https://www.osram.us/cb/tools-and-resources/applications/led-colorcalculator/index.jsp.

[70] R. Davis. A correlated color temperature for illuminants. *Bureau of Standards Journal of Research*, **7**, 659 (1931). doi: 10.6028/jres.007.039.

[71] C. S. McCamy. Correlated color temperature as an explicit function of chromaticity coordinates. *Color Research & Application*, **17**, 2, 142 (1992). doi: 10.1002/col.5080170211.

[72] S. Stoll. Easyspin online documentation. http://easyspin.org/easyspin/documentation/hamiltonian.html.

[73] G. Jeschke. Determination of the nanostructure of polymer materials by electron paramagnetic resonance spectroscopy. *Macromolecular Rapid Communications*, **23**, 4, 227 (2002). doi: 10.1002/1521-3927(20020301)23:4<227::AID-MARC227>3.0.CO;2-D.

[74] S. Richert, C. E. Tait and C. R. Timmel. Delocalisation of photoexcited triplet states probed by transient EPR and hyperfine spectroscopy. *Journal of Magnetic Resonance*, **280**, 103 (2017). doi: 10.1016/j.jmr.2017.01.005.

[75] C. Thomson. Electron Spin Resonance Studies of the Triplet State. *Quarterly Reviews, Chemical Society*, **22**, 1, 45 (1968). doi: 10.1039/QR9682200045.

[76] S. Väth, K. Tvingstedt, A. Baumann, M. C. Heiber, A. Sperlich, J. A. Love, T.-Q. Nguyen and V. Dyakonov. Triplet excitons in highly efficient solar cells based on the soluble small molecule p-DTS $(FBTTh_2)_2$. *Advanced Energy Materials*, **7**, 7, 1602016 (2017). doi: 10.1002/aenm.201602016.

[77] H. Kraus, M. C. Heiber, S. Väth, J. Kern, C. Deibel, A. Sperlich and V. Dyakonov. Analysis of triplet exciton loss pathways in PTB7:$PC_{71}BM$ bulk heterojunction solar cells. *Scientific Reports*, **6**, 29158 (2016). doi: 10.1038/srep29158.

[78] M. Di Valentin, C. Kay, G. Giacometti and K. Möbius. A time-resolved electron nuclear double resonance study of the photoexcited triplet state of P680 in isolated reaction centers of photosystem 2. *Chemical Physics Letters*, **248**, 5-6, 434 (1996). doi: 10.1016/0009-2614(95)01347-4.

[79] M. M. Roessler and E. Salvadori. Principles and applications of EPR spectroscopy in the chemical sciences. *Chemical Society Reviews*, **47**, 8, 2534 (2018). doi: 10.1039/c6cs00565a.

[80] A. Sperlich. Electron paramagnetic resonance spectroscopy of conjugated polymers and fullerenes for organic photovoltaics. Ph.D. thesis, University of Würzburg (2013).

[81] P. Kottis and R. Lefebvre. Calculation of the electron spin resonance line shape of randomly oriented molecules in a triplet state. i. the $\Delta m = 2$ transition with a constant linewidth. *The Journal of Chemical Physics*, **39**, 2, 393 (1963). doi: 10.1063/1.1734260.

[82] S. S. Eaton, K. M. More, B. M. Sawant and G. R. Eaton. Use of the ESR half-field transition to determine the interspin distance and the orientation of the interspin vector in systems with two unpaired electrons. *Journal of the American Chemical Society*, **105**, 22, 6560 (1983). doi: 10.1021/ja00360a005.

[83] D. McCamey, K. Van Schooten, W. Baker, S.-Y. Lee, S.-Y. Paik, J. Lupton and C. Boehme. Hyperfine-field-mediated spin beating in electrostatically bound charge carrier pairs. *Physical Review Letters*, **104**, 1, 017601 (2010). doi: 10.1103/PhysRevLett.104.017601.

[84] L. Swanson, P. Lane, J. Shinar and F. Wudl. Polarons and triplet polaronic excitons in poly (paraphenylenevinylene)(PPV) and substituted PPV: an optically detected magnetic resonance study. *Physical Review B*, **44**, 19, 10617 (1991). doi: 10.1103/PhysRevB.44.10617.

[85] E. Goovaerts. Optically detected magnetic resonance (ODMR). *eMagRes*, 343–358 (2007). doi: 10.1002/9780470034590.emrstm1524.

[86] D. Carbonera. Optically detected magnetic resonance (ODMR) of photoexcited triplet states. *Photosynthesis Research*, **102**, 2-3, 403 (2009). doi: 10.1007/s11120-009-9407-5.

[87] C. Boehme and H. Malissa. Electrically detected magnetic resonance spectroscopy. *eMagRes*, 83–100 (2007). doi: 10.1002/9780470034590.emrstm1525.

[88] E. H. Fooks and R. A. Zakarevicius. *Microwave engineering using microstrip circuits*. Prentice-Hall, Inc. (1990). ISBN 9780136916505.

[89] L. Kudriashova. Photoluminescence reveals charge carrier recombination in organic and hybrid semiconductors. Ph.D. thesis, University of Würzburg (2019).

[90] A. Endo, M. Ogasawara, A. Takahashi, D. Yokoyama, Y. Kato and C. Adachi. Thermally activated delayed fluorescence from Sn^{4+}–porphyrin complexes and their application to organic light emitting diodes—a novel mechanism for electroluminescence. *Advanced Materials*, **21**, 47, 4802 (2009). doi: 10.1002/adma.200900983.

[91] W.-Y. Hung, G.-C. Fang, Y.-C. Chang, T.-Y. Kuo, P.-T. Chou, S.-W. Lin and K.-T. Wong. Highly efficient bilayer interface exciplex for yellow organic light-emitting diode. *ACS Applied Materials & Interfaces*, **5**, 15, 6826 (2013). doi: 10.1021/am402032z.

[92] J. Li, H. Nomura, H. Miyazaki and C. Adachi. Highly efficient exciplex organic light-emitting diodes incorporating a heptazine derivative as an electron acceptor. *Chemical Communications*, **50**, 46, 6174 (2014). doi: 10.1039/C4CC01590H.

[93] Q. Huang, S. Zhao, Z. Xu, X. Fan, C. Shen and Q. Yang. Exciplex emission and decay of co-deposited 4,4',4"-tris[3-methylphenyl(phenyl)amino]triphenylamine:tris-[3-(3-pyridyl)mesityl]borane organic light-emitting devices with different electron transporting layer thicknesses. *Applied Physics Letters*, **104**, 16, 161112 (2014). doi: 10.1063/1.4870492.

[94] E. Hontz, W. Chang, D. N. Congreve, V. Bulović, M. A. Baldo and T. Van Voorhis. The role of electron–hole separation in thermally activated delayed fluorescence in donor–acceptor blends. *The Journal of Physical Chemistry C*, **119**, 45, 25591 (2015). doi: 10.1021/acs.jpcc.5b07340.

[95] P. Deotare, W. Chang, E. Hontz, D. Congreve, L. Shi, P. Reusswig, B. Modtland, M. Bahlke, C. Lee, A. Willard, V. Bulović, T. Van Voorhis and M. Baldo. Nanoscale transport of charge-transfer states in organic donor–acceptor blends. *Nature Materials*, **14**, 11, 1130 (2015). doi: 10.1038/nmat4424.

[96] W. Chang, D. N. Congreve, E. Hontz, M. E. Bahlke, D. P. McMahon, S. Reineke, T. C. Wu, V. Bulović, T. Van Voorhis and M. A. Baldo. Spin-dependent charge transfer state design rules in organic photovoltaics. *Nature Communications*, **6**, 6415 (2015). doi: 10.1038/ncomms7415.

[97] E. W. Evans, Y. Olivier, Y. Puttisong, W. K. Myers, T. J. Hele, S. M. Menke, T. H. Thomas, D. Credgington, D. Beljonne, R. H. Friend et al. Vibrationally assisted intersystem crossing in benchmark thermally activated delayed fluorescence molecules. *The Journal of Physical Chemistry Letters*, **9**, 14, 4053 (2018). doi: 10.1021/acs.jpclett.8b01556.

[98] S. Väth, K. Tvingstedt, M. Auth, A. Sperlich, A. Dabuliene, J. V. Grazulevicius, P. Stakhira, V. Cherpak and V. Dyakonov. Direct observation of spin states involved in organic electroluminescence based on thermally activated delayed fluorescence. *Advanced Optical Materials*, **5**, 3 (2017). doi: 10.1002/adom.201600926.

[99] R. S. Nobuyasu, Z. Ren, G. C. Griffiths, A. S. Batsanov, P. Data, S. Yan, A. P. Monkman, M. R. Bryce and F. B. Dias. Rational design of TADF polymers using a donor–acceptor monomer with enhanced TADF efficiency induced by the energy alignment of charge transfer and local triplet excited states. *Advanced Optical Materials*, **4**, 4, 597 (2016). doi: 10.1002/adom.201500689.

[100] A. Michaleviciute, E. Gurskyte, D. Y. Volyniuk, V. V. Cherpak, G. Sini, P. Y. Stakhira and J. V. Grazulevicius. Star-shaped carbazole derivatives for bilayer white organic light-emitting diodes combining emission from both excitons and exciplexes. *The Journal of Physical Chemistry C*, **116**, 39, 20769 (2012). doi: 10.1021/jp306824u.

[101] V. Cherpak, P. Stakhira, B. Minaev, G. Baryshnikov, E. Stromylo, I. Helzhynskyy, M. Chapran, D. Volyniuk, Z. Hotra, A. Dabuliene, A. Tomkeviciene, L. Voznyak and J. V. Grazulevicius. Mixing of phosphorescent and exciplex emission in efficient organic electroluminescent devices. *ACS Applied Aaterials & Interfaces*, **7**, 2, 1219 (2015). doi: 10.1021/am507050g.

[102] N. Bunzmann, S. Weissenseel, L. Kudriashova, J. Gruene, B. Krugmann, J. V. Grazulevicius, A. Sperlich and V. Dyakonov. Optically and electrically excited intermediate electronic states in donor: acceptor based OLEDs. *Materials Horizons*, **7**, 1126 (2020). doi: 10.1039/C9MH01475F.

[103] K.-H. Kim, S.-J. Yoo and J.-J. Kim. Boosting triplet harvest by reducing nonradiative transition of exciplex toward fluorescent organic light-emitting diodes with 100% internal quantum efficiency. *Chemistry of Materials*, **28**, 6, 1936 (2016). doi: 10.1021/acs.chemmater.6b00478.

[104] H. A. Al Attar and A. P. Monkman. Electric field induce blue shift and intensity enhancement in 2D exciplex organic light emitting diodes; controlling electron–hole separation. *Advanced Materials*, **28**, 36, 8014 (2016). doi: 10.1002/adma.201600965.

[105] Q. Huang, S. Zhao, P. Wang, Z. Qin, Z. Xu, D. Song, B. Qiao and X. Xu. Investigating the evolution of exciplex states in thermally activated delayed fluorescence organic light-emitting diodes by transient measurement. *Journal of Luminescence*, **201**, 38 (2018). doi: 10.1016/j.jlumin.2018.03.094.

[106] N. S. Sariciftci, L. Smilowitz, A. J. Heeger and F. Wudl. Photoinduced electron transfer from a conducting polymer to buckminsterfullerene. *Science*, 1474–1476 (1992). doi: 10.1126/science.258.5087.1474.

[107] I.-W. Hwang, D. Moses and A. J. Heeger. Photoinduced carrier generation in P3HT/PCBM bulk heterojunction materials. *The Journal of Physical Chemistry C*, **112**, 11, 4350 (2008). doi: 10.1021/jp075565x.

[108] S.-Y. Lee, S. Paik, D. R. McCamey and C. Boehme. Modulation frequency dependence of continuous-wave optically/electrically detected magnetic resonance. *Physical Review B*, **86**, 11, 115204 (2012). doi: 10.1103/PhysRevB.86.115204.

[109] X.-K. Liu, Z. Chen, C.-J. Zheng, C.-L. Liu, C.-S. Lee, F. Li, X.-M. Ou and X.-H. Zhang. Prediction and design of efficient exciplex emitters for high-efficiency, thermally activated delayed-fluorescence organic light-emitting diodes. *Advanced Materials*, **27**, 14, 2378 (2015). doi: 10.1002/adma.201405062.

[110] D. Graves, V. Jankus, F. B. Dias and A. Monkman. Photophysical investigation of the thermally activated delayed emission from films of m-MTDATA:PBD exciplex. *Advanced Functional Materials*, **24**, 16, 2343 (2014). doi: 10.1002/adfm.201303389.

[111] T. Basel, D. Sun, S. Baniya, R. McLaughlin, H. Choi, O. Kwon and Z. V. Vardeny. Magnetic field enhancement of organic light-emitting diodes based on electron donor–acceptor exciplex. *Advanced Electronic Materials*, **2**, 2 (2016). doi: 10.1002/aelm.201500248.

[112] C. Zhang, D. Sun, C. Sheng, Y. Zhai, K. Mielczarek, A. Zakhidov and Z. Vardeny. Magnetic field effects in hybrid perovskite devices. *Nature Physics*, **11**, 5, 427 (2015). doi: 10.1038/nphys3277.

[113] S. Stoll and A. Schweiger. Easyspin, a comprehensive software package for spectral simulation and analysis in EPR. *Journal of Magnetic Resonance*, **178**, 1, 42 (2006). doi: 10.1016/j.jmr.2005.08.013.

[114] Z. Yu. Spin-orbit coupling and its effects in organic solids. *Physical Review B*, **85**, 11, 115201 (2012). doi: 10.1103/PhysRevB.85.115201.

[115] R. A. Marcus. On the theory of oxidation-reduction reactions involving electron transfer. I. *The Journal of Chemical Physics*, **24**, 5, 966 (1956). doi: 10.1063/1.1742723.

[116] C. Murawski, K. Leo and M. C. Gather. Efficiency roll-off in organic light-emitting diodes. *Advanced Materials*, **25**, 47, 6801 (2013). doi: 10.1002/adma.201301603.

[117] A. Schnegg, J. Behrends, M. Fehr and K. Lips. Pulsed electrically detected magnetic resonance for thin film silicon and organic solar cells. *Physical Chemistry Chemical Physics*, **14**, 42, 14418 (2012). doi: 10.1039/C2CP41258F.

[118] C. Boehme and K. Lips. Theory of time-domain measurement of spin-dependent recombination with pulsed electrically detected magnetic resonance. *Physical Review B*, **68**, 24, 245105 (2003). doi: 10.1103/PhysRevB.68.245105.

[119] C. Boehme and K. Lips. Electrical detection of spin coherence in silicon. *Physical review letters*, **91**, 24, 246603 (2003). doi: 10.1103/PhysRevLett.91.246603.

[120] C. Boehme and K. Lips. A pulsed EDMR study of hydrogenated microcrystalline silicon at low temperatures. *physica status solidi (c)*, **1**, 5, 1255 (2004). doi: 10.1002/pssc.200304326.

[121] T. Herring, S.-Y. Lee, D. McCamey, P. Taylor, K. Lips, J. Hu, F. Zhu, A. Madan and C. Boehme. Experimental discrimination of geminate and non-geminate recombination in a-Si: H. *Physical Review B*, **79**, 19, 195205 (2009). doi: 10.1103/PhysRevB.79.195205.

[122] J. Behrends, A. Schnegg, K. Lips, E. Thomsen, A. K. Pandey, I. D. Samuel and D. J. Keeble. Bipolaron formation in organic solar cells observed by pulsed electrically detected magnetic resonance. *Physical Review Letters*, **105**, 17, 176601 (2010). doi: 10.1103/PhysRevLett.105.176601.

[123] D. McCamey, H. Seipel, S.-Y. Paik, M. Walter, N. Borys, J. Lupton and C. Boehme. Spin rabi flopping in the photocurrent of a polymer light-emitting diode. *Nature Materials*, **7**, 9, 723 (2008). doi: 10.1038/nmat2252.

[124] W. Baker, D. McCamey, K. Van Schooten, J. Lupton and C. Boehme. Differentiation between polaron-pair and triplet-exciton polaron spin-dependent mechanisms in organic light-emitting diodes by coherent spin beating. *Physical Review B*, **84**, 16, 165205 (2011). doi: 10.1103/PhysRevB.84.165205.

[125] W. Baker, T. Keevers, J. Lupton, D. McCamey and C. Boehme. Slow hopping and spin dephasing of coulombically bound polaron pairs in an organic semiconductor at room temperature. *Physical Review Letters*, **108**, 26, 267601 (2012). doi: 10.1103/PhysRevLett.108.267601.

[126] M. Kavand, D. Baird, K. van Schooten, H. Malissa, J. M. Lupton and C. Boehme. Discrimination between spin-dependent charge transport and spin-dependent recombination in π-conjugated polymers by correlated current and electroluminescence-detected magnetic resonance. *Physical Review B*, **94**, 7, 075209 (2016). doi: 10.1103/PhysRevB.94.075209.

[127] T. Zhang, B. Chu, W. Li, Z. Su, Q. M. Peng, B. Zhao, Y. Luo, F. Jin, X. Yan, Y. Gao et al. Efficient triplet application in exciplex delayed-fluorescence OLEDs using a reverse intersystem crossing mechanism based on a ΔE_{S-T} of around zero. *ACS Applied Materials & Interfaces*, **6**, 15, 11907 (2014). doi: 10.1021/am501164s.

[128] D. J. Lepine. Spin-dependent recombination on silicon surface. *Physical Review B*, **6**, 2, 436 (1972). doi: 10.1103/PhysRevB.6.436.

[129] D. Kaplan, I. Solomon and N. Mott. Explanation of the large spin-dependent recombination effect in semiconductors. *Journal de Physique Lettres*, **39**, 4, 51 (1978). doi: 10.1051/jphyslet:0197800390405100.

[130] N. Kishimoto, K. Morigaki and K. Murakami. Conductivity change due to electron spin resonance in amorphous Si-Au system. *Journal of the Physical Society of Japan*, **50**, 6, 1970 (1981). doi: 10.1143/JPSJ.50.1970.

[131] G. R. Eaton, S. S. Eaton, D. P. Barr and R. T. Weber. *Quantitative Epr*. Springer Science & Business Media (2010). ISBN 9783211929483.

[132] M. Kavand, C. Zhang, D. Sun, H. Malissa, Z. Vardeny and C. Boehme. Quantitative inverse spin hall effect detection via precise control of the driving-field amplitude. *Physical Review B*, **95**, 16, 161406 (2017). doi: 10.1103/PhysRevB.95.161406.

[133] H. De Raedt, B. Barbara, S. Miyashita, K. Michielsen, S. Bertaina and S. Gambarelli. Quantum simulations and experiments on Rabi oscillations of spin

qubits: intrinsic vs extrinsic damping. *Physical Review B*, **85**, 1, 014408 (2012). doi: 10.1103/PhysRevB.85.014408.

[134] L. Zhu, K. Xu, Y. Wang, J. Chen and D. Ma. High efficiency yellow fluorescent organic light emitting diodes based on m-MTDATA/BPhen exciplex. *Frontiers of Optoelectronics*, **8**, 4, 439 (2015). doi: 10.1007/s12200-015-0492-0.

[135] F. B. Dias, K. N. Bourdakos, V. Jankus, K. C. Moss, K. T. Kamtekar, V. Bhalla, J. Santos, M. R. Bryce and A. P. Monkman. Triplet harvesting with 100% efficiency by way of thermally activated delayed fluorescence in charge transfer OLED emitters. *Advanced Materials*, **25**, 27, 3707 (2013). doi: 10.1002/adma.201300753.

[136] W. Liu, J.-X. Chen, C.-J. Zheng, K. Wang, D.-Y. Chen, F. Li, Y.-P. Dong, C.-S. Lee, X.-M. Ou and X.-H. Zhang. Novel strategy to develop exciplex emitters for high-performance OLEDs by employing thermally activated delayed fluorescence materials. *Advanced Functional Materials*, **26**, 12, 2002 (2016). doi: 10.1002/adfm.201505014.

[137] D. Qin and Y. Tao. White organic light-emitting diode comprising of blue fluorescence and red phosphorescence. *Applied Physics Letters*, **86**, 11, 113507 (2005). doi: 10.1063/1.1879108.

[138] G. Schwartz, K. Fehse, M. Pfeiffer, K. Walzer and K. Leo. Highly efficient white organic light emitting diodes comprising an interlayer to separate fluorescent and phosphorescent regions. *Applied Physics Letters*, **89**, 8, 083509 (2006). doi: 10.1063/1.2338588.

[139] B. Zhao, T. Zhang, B. Chu, W. Li, Z. Su, Y. Luo, R. Li, X. Yan, F. Jin, Y. Gao and H. Wu. Highly efficient tandem full exciplex orange and warm white OLEDs based on thermally activated delayed fluorescence mechanism. *Organic Electronics*, **17**, 15 (2015). doi: 10.1016/j.orgel.2014.11.014.

[140] G. Grybauskaite-Kaminskiene, K. Ivaniuk, G. Bagdziunas, P. Turyk, P. Stakhira, G. Baryshnikov, D. Volyniuk, V. Cherpak, B. Minaev, Z. Hotra, H. Agren and J. V. Grazulevicius. Contribution of TADF and exciplex emission for efficient "warm-white" OLEDs. *Journal of Materials Chemistry C*, **6**, 6, 1543 (2018). doi: 10.1039/C7TC05392D.

[141] X. Cao, J. Hu, Y. Tao, W. Yuan, J. Jin, X. Ma, X. Zhang and W. Huang. Alkyl effects on the optoelectronic properties of bicarbazole/cyanobenzene hybrid host materials: double delayed fluorescent host/dopant systems in solution-processed OLEDs. *Dyes and Pigments*, **136**, 543 (2017). doi: 10.1016/j.dyepig.2016.09.008.

[142] H.-T. Cao, Y. Zhao, C. Sun, D. Fang, L.-H. Xie, M.-N. Yan, Y. Wei, H.-M. Zhang and W. Huang. Novel electron acceptor based on spiro [fluorine-9, 9'-xanthene] for exciplex thermally activated delayed fluorescence. *Dyes and Pigments*, **149**, 422 (2018). doi: 10.1016/j.dyepig.2017.10.019.

Publications and Conference Contributions

Publications in peer-reviewed journals

1. N. Bunzmann, S. Weissenseel, L. Kudriashova, J. Gruene, B. Krugmann, J. V. Grazulevicius, A. Sperlich and V. Dyakonov. Optically and electrically excited intermediate electronic states in donor: acceptor based OLEDs. *Materials Horizons*, **7**, 1126 (2020)

2. N. Bunzmann, B.Krugmann, S. Weissenseel, L. Kudriashova, K. Ivaniuk, P. Stakhira, V. Cherpak, M. Chapran, G. Grybauskaite-Kaminskiene, J. V. Grazulevicius, V. Dyakonov and A. Sperlich. Spin- and Voltage-dependent emission from Intra- and Intermolecular TADF OLEDs. *Advanced Electronic Materials*, aelm.202000702R1 (2020)

3. J. Gruene, N.Bunzmann, M. Meinecke, A.Sperlich and V. Dyakonov. Kinetic Modeling of Transient Electroluminescence Reveals TTA as an Efficiency-Limiting Process in Exciplex-Based TADF OLEDs. *The Journal of Physical Chemistry C*, 124, 47, 25667–25674 (2020)

Publications with arXiv Preprint

1. N. Bunzmann, D.Baird, H.Malissa, S. Weissenseel, C. Boehme, V. Dyakonov, and A. Sperlich. Thermal activation bottleneck in TADF OLEDs based on m-MTDATA:BPhen (2020). *Preprint on arXiv*

Contributed Talks

1. **DPG Frühjahrstagung in Dresden**. N. Bunzmann, S. Weissenseel, B. Krugmann, J. Gruene, A. Sperlich, and V. Dyakonov. Investigation of organic light emitting diodes based on thermally activated delayed fluorescence via magnetic resonance methods (2017)

2. **The 50th Annual International Meeting of the ESR Spectroscopy Group of the Royal Society of Chemistry in Oxford** N. Bunzmann, S. Weissenseel, B. Krugmann, S. Väth, A. Sperlich, and V. Dyakonov. Investigation of spin states in organic light emitting diodes based on thermally activated delayed fluorescence via multi-frequency magnetic resonance techniques (2017)
3. **GRK2112 Seminar in Niederstetten** N. Bunzmann, S. Weissenseel, B. Krugmann, L. Kudriashova, J. Gruene, S. Väth, A. Sperlich, and V. Dyakonov. Difference between Optical Excitation and Electrical Generation in Donor-Acceptor based OLEDs (2017)
4. **DPG Frühjahrstagung in Berlin** N. Bunzmann, B. Krugmann, S. Weissenseel, G. Grybauskaite-Kaminskiene, D. Volyniuk, A. Sperlich, J.V. Grazulevicius and V. Dyakonov. Intra- and Intermolecular TADF emission investigated by magnetic resonance methods (2018)
5. **International Krutyn TADF Summer School in Krutyn** N. Bunzmann, S. Weissenseel, B. Krugmann, L. Kudriashova, J. Gruene, A. Sperlich, and V. Dyakonov. Optically and electrically excited intermediate electronic states in donor:acceptor based OLEDs (2019)

Conference Posters

1. **SPP1601 Annual Meeting in Hirschegg**. N. Bunzmann, S. Weissenseel, M. Auth, S. Väth, A. Sperlich, and V. Dyakonov. Investigation of spin states in organic light emitting diodes based on thermally activated delayed fluorescence via multi-frequency ELDMR and EDMR techniques (2016)
2. **GRK2112 Symposium in Würzburg** N. Bunzmann, B. Krugmann, S. Weissenseel, G. Grybauskaite-Kaminskiene, D. Volyniuk, A. Sperlich, J.V. Grazulevicius and V. Dyakonov. Investigation of Inter- and Intramolecular TADF emission by magnetic resonance methods (2018)
3. **GDCh FGMR Annual Meeting in Leipzig** N. Bunzmann, B. Krugmann, S. Weissenseel, G. Grybauskaite-Kaminskiene, D. Volyniuk, A. Sperlich, J.V. Grazulevicius and V. Dyakonov. Intra- and Intermolecular TADF emission investigated by magnetic resonance methods (2018)
4. **DPG Frühjahrstagung in Regensburg** N. Bunzmann, S. Weissenseel, J. Gruene, C. Boehme, V. Dyakonov and A. Sperlich. Taking OLEDs for a Spin (2019)

Danksagung

An dieser Stelle möchte ich mich bei all denjenigen bedanken, die in irgendeiner Form zum erfolgreichen Gelingen dieser Arbeit beigetragen haben. Zum einen haben mir eine ganze Reihe von Personen geholfen wissenschaftlich erfolgreich zu sein. Zum anderen waren die 4 Jahre, in denen ich an meiner Promotion gearbeitet habe, eine sehr lustige Zeit, die ich immer gerne in Erinnerung behalten werde.

- Ein ganz besonderer Dank geht an meinen Doktorvater Prof. Vladimir Dyakonov. Danke für das Vertrauen, das du mir geschenkt hast, als du mir eine Promotionsstelle angeboten hast. Ich hatte eine großartige Zeit an deinem Lehrstuhl und habe viel über das wissenschaftliche Arbeiten gelernt. Ein Paper zu veröffentlichen und Vorträge auf nationalen und internationalen Konferenzen halten zu dürfen waren besondere Erfahrungen für mich. Danke, dass du diese interessante und lustige Zeit möglich gemacht hast.

- Großer Dank geht auch an meinen Betreuer Dr. habil. Andreas Sperlich. Danke, dass du es mir ermöglicht hast meine Doktorarbeit in deiner SpinOS-Arbeitsgruppe anzufertigen. Ich habe viel über Physik, experimentelles Arbeiten im Labor, das Halten von Vorträgen und das Schreiben von Papern von dir gelernt. Besonders schön fand ich, dass du immer Wert auf eine gute Arbeitsatmosphäre in der Arbeitsgruppe gelegt hast und Diskussionen über sämtliche Probleme immer auf Augenhöhe statt fanden.

- Sebastian Weißenseel, danke für die tolle Zusammenarbeit mit dir, welche wesentlich zum Erfolg meiner Promtion beigetragen hat. Als du für deine Masterarbeit an den Lehrstuhl kamst hast du dich als Messknecht angekündigt aber diese Bezeichnung hat sich als grobe Fehleinschätzung herausgestellt. Zusammen haben wir die OLED Forschung am Lehrstuhl vorangetrieben und sind dabei viele Herausforderungen gemeinsam angegangen. Du aus Unterfranken und ich aus Oberfranken war (auch sprachlich) einfach die richtige Kombi.

- Liudmila Kudriashova, thanks for all the PL measurements you performed for me and for all the discussions about organic semiconductors. I learned a lot from you! Even when I had the audacity to call you during your vacation, you came to the university and helped me. I don't take all of that for granted. I am happy to say that I have a Russian friend now. Спасибо.

- Jeannine Gruene, danke für deine Beiträge zu meiner Doktorarbeit während deiner Bachelor- und Masterarbeit und während deiner Promotion. Mit deinem Ehrgeiz und deiner motivierten Arbeitseinstellung hattest du immer wieder Anteil an meinen wissenschaftlichen Errungenschaften. Wenn ich gehe bist du eine würdige Nachfolgerin :-)

- Michael Auth, was soll ich sagen? Die gemeinsame Zeit mit dir im Büro war einfach der Hammer! Wenns um Diskussionen zu Physik und EPR oder auch um Hilfeleistung im Labor ging, war auf dich immer Verlass. Danke auch für deine Kameradschaft auf allen EPR Konferenzen, die wir zusammen besucht haben. Dazu kommen sämtliche Spaßaktionen die wir gemeinsam durchgezogen haben: Bürofitness, Kickern, Laser Tag, Mountain Biken, Ski-Fahren, Fußball und natürlich AOE2. Semper paratus pro proelio!

- Danke Benjamin Krugmann, du hast als Masterstudent einen großen Teil der Arbeit zum pCNBCzoCF$_3$-Molekül geleistet und damit wesentlich zu meiner Doktorarbeit beigetragen. Deine Zeit am Lehrstuhl war eine der witzigsten, weil wir beim Chillen am Main, beim Kickern, Weinwandern usw. immer eine gute Gemeinschaft hatten. Du bist einfach ein krasser Typ, der sich nie ewig Stress macht.

- Was wäre ich ohne meinen Personal Coach Andreas Gottscholl? Danke für die lustige Zeit beim Calisthenics. Dank dir bin ich jetzt krass-fit und kann (fast) einen Muscle-Up und eine Human-Flag.

- Danke auch an die Perovskite-Boys um David, Phillip und Kris. Dank euch kenn ich micht jetzt auch in der Welt der Solarzellen aus. Und ihr habt mir immer bei Fragen zum Glovebox-Labor geholfen. Danke auch für die vielen lustigen Gespräche in der Mensa.

- Danke an Rebecca Bönnighausen für die magnetfeldabhängigen ELDMR Messungen, die zum erfolgreichen Veröffentlichen meines Papers beigetragen haben. Und danke für deine gnadenlose Motivation beim Training.

- Danke auch an Prof. Jens Pflaum und seine Doktoranden Ulli, Thomas, Sebastian und die beiden Maxe. Der Austausch mit eurer Arbeitsgruppe war immer sehr gewinnbringend und ich durfte viel Spaß beim Kickern mit euch haben.

- Danke Diep Phan für deine freundliche Hilfe bei allen verwaltungstechnischen Angelegenheiten. Danke vor allem für dein präzises Auge und deine Geduld bei Anträgen jeglicher Art.

- Danke André Thiem-Riebe für deine zuverlässige Hilfe bei sämtlichen Problemen im Labor.

- Ganz besonderer Dank geht an Christian Kasper. Wir haben über die letzten 10 Jahre gemeinsam unseren Bachelor, Master und die Doktorarbeit durchgezogen. Dabei haben wir uns durch Klausuren, Praktika, Abschlussarbeiten usw. gekämpft und uns immer gegenseitig unterstützt. Danke für deine Kameradschaft. Absolut unvergessen werden die vielen Fußball Spiele bleiben, die wir gemeinsam gekuckt haben. Besonders das CL Finale 2013: Boateng, Ribery, Robben, boom!

- Abschließend möchte ich den wichtigsten Menschen in meinem Leben, meiner Familie, danken: meinen Eltern Doris und Konrad Bunzmann, meinen Schwestern Hanna und Leah, meinem Bruder Julian, seiner Frau Christina, meinem Neffen Theo und meiner Nichte Malia. Ihr wart während meines gesamten Studiums und während meiner Promotion immer für mich da! Die schriftliche Zusammenstellung dieser Arbeit ist während der außergewöhnlichen Corona Zeit entstanden, in der wir als Familie noch enger zusammengerückt sind. Die enge Gemeinschaft mit euch allen hat mir enorm geholfen die Kraft für das Schreiben meiner Arbeit zu finden.

Finanzielle Förderung

Diese Arbeit an der Universität Würzburg wurde durch die Deutsche Forschungsgemeinschaft (DFG) über das Schwerpunktprogramm SPP 1601 “New Frontiers in Sensitivity for EPR Spectroscopy: from Biological Cells to Nano Materials ” unterstützt.